Università degli Studi di Cagliari

DOTTORATO DI RICERCA

Scienze e Tecnologie della Terra e dell'Ambiente

Ciclo XXIX

Dispersion of metals in San Giorgio river (Sardinia SW): interaction between minerals and biosphere

Settore/i scientifico disciplinari di afferenza

GEO/06

Presentata da *Dott.ssa Claudia Pusceddu*

Coordinatore Dottorato *Prof. Aldo Muntoni*

Tutor *Dott. Giovanni De Giudici*

Co-Tutor *Dott. Richard B. Wanty*

Dott.ssa Daniela Medas

Esame finale anno accademico 2016 – 2017

Tesi discussa nella sessione d'esame marzo – aprile 2017

Abstract

Trace metals, particularly Zn, are nutrients for living organisms, however, when present in the environment in high concentrations, trace metals can pose a serious threat to ecosystem and human health. Geochemical behaviour of Zn is characterized by high mobility and bioavailability, and although Zn is an essential trace element in plant metabolism, its excess can have toxic effects in plants, limiting their growth and/or diffusion.

In mine environments, dispersion and attenuation of trace metals can be mediated by processes occurring at the critical zone where water, sediments and biosphere meet. As the interface between surface and groundwater, the hyporheic zone of riverbed sediments is recognized as a critically important ecotone where biogeochemical reaction takes place. Knowledge of the hyporheic zone is of interest to develop sustainable techniques such as phytoremediation. These techniques can be targeted to the stabilization and/or to the extraction of metals, their success depends upon the type of plant used and the specific geological conditions. The use of autochthonous plants for stabilization and pollution control is probably the most realistic and effective method to rehabilitate land affected by these threats.

The purpose of the present study is to investigate how the interaction between mineral and biosphere can mitigate the dispersion of trace metals in mine environments. The focus of the study is on i) understanding the overall process ruling attenuation of trace metals, and ii) understanding the specific microscopic processes.

Different scales of study and different investigation methods were used. Catchment scale investigation was carried out by applying hydrological tracer to the basin of Rio San Giorgio (SW, Sardinia). The riverbed of Rio San Giorgio is characterized by the presence of a natural dense vegetation comprising mainly *Juncus acutus* and *Phragmites australis,* that rules the streambed

morphology, erosional processes and water flow velocity. The riverbed sediments are mine wastes with up to 1-2 % in Zn and Pb.

Biogeochemical barriers were recognized to be active in the hyporheic zone of Rio San Giorgio, presence of framboidal pyrite in sediments of Rio San Giorgio and concentration of elements at the surfaces of roots is a first mechanism limiting trace metal mobility. Plants build up a second biogeochemical barrier. In fact they i) uptake significant amounts of Fe and Zn; ii) drop the excess of Fe and Zn inside the plants is by biomineralization processes leading to the formation of Zn hydroxyapatite-like or similar phases occurring in the roots; iii) translocate as Zn-organic-complexes (amino acids as Zn cysteine and Zn acetate hydrate) into stems and leaves.

Rhizobox experiments and isotopic analyses were conceived to make a step forward in understanding the mechanisms that rule the interaction between mineral, water and plants under controlled conditions. A different response of the plants to Zn supply was found and this depended on mineralogy, Zn concentration in waters, and plant species.

Results from rhizobox experiments indicate that the response of the plants to Zn supply can slightly change depending of the amount and the way Zn is supplied, if it is present in highest concentration in water or substrate. Overall, *Phragmites a.* and *Juncus a.* are metal tolerant species that are suitable for phytoremediation. Particularly, they are excellent candidates for phytostabilization of metals. The results obtained in this work have clarified natural attenuation processes that occur in the hyporheic zone of rio San Giorgio. The resulting information provides useful knowledge to design phytoremediation techniques in areas affected by mine pollution.

Ringraziamenti

Giunti al termine di questo percorso è doveroso ringraziare tutti coloro che hanno reso possibile lo sviluppo di questa ricerca e l'elaborazione di questa tesi.

Innanzitutto il mio Tutor Dott. Giovanni De Giudici che, con le sue competenze e il suo supporto, è stato una guida durante il percorso. La Dott.sa Daniela Medas che, oltre ad essere un valido sostegno scientifico, è stata un importante punto di riferimento. Il Dott. Rich B. Wanty per l'aiuto ed i suggerimenti lungo tutto il periodo.

Desidero inoltre ringraziare Salvatore Vacca e la Dott.ssa Francesca Podda per il loro aiuto nelle varie fasi del lavoro in laboratorio.

Il Prof. Carlo Meneghini e il prof. Marco Merlini per l'assistenza nell'ambito delle tecniche di luce al sincrotrone.

Ringrazio il Dott. Vittorio Murgia per la sua preziosa collaborazione durante l'esperimento dei rhizobox.

Ringrazio inoltre le mie cugine e amiche Emanuela, Alessandra, Adele e Michela che in varie fasi dei tre anni hanno dato il loro apporto per la buona riuscita di questa tesi. Ringrazio Claudia per le lunghe chiacchierate e il sostegno morale.

Un grande grazie va a Roberta, compagna anche in questa avventura, sempre presente come collega e come amica.

Ringrazio i miei genitori e mio fratello che sempre mi appoggiano in ogni nuova esperienza. Per ultimo, ma non certo per importanza, mio marito Maurizio che ha supportato e sopportato ogni momento di questi tre anni, che sempre mi incoraggia ad accettare ogni nuova sfida.

Summary

Results and discussion

Chapter 1- Introduction

1.1 Zn biogeochemical cycle

Trace metals, particularly Zn, are nutrients for living organisms, however, when present in the environment in high concentrations, trace metals can pose a serious threat to ecosystem and human health (Shadid et al., 2017). Geochemical behaviour of Zn is characterized by high mobility and bioavailability, and although Zn is an essential trace element in plant metabolism, its excess can have toxic effects in plants, limiting their growth and/or diffusion (Mateos-Narajos et al., 2014). Figure 1 summarizes the biogeochemical cycle of Zn, and highlights the main input and output of the processes ruling Zn cycling between geosphere and biosphere, and the impact of human activities over them.

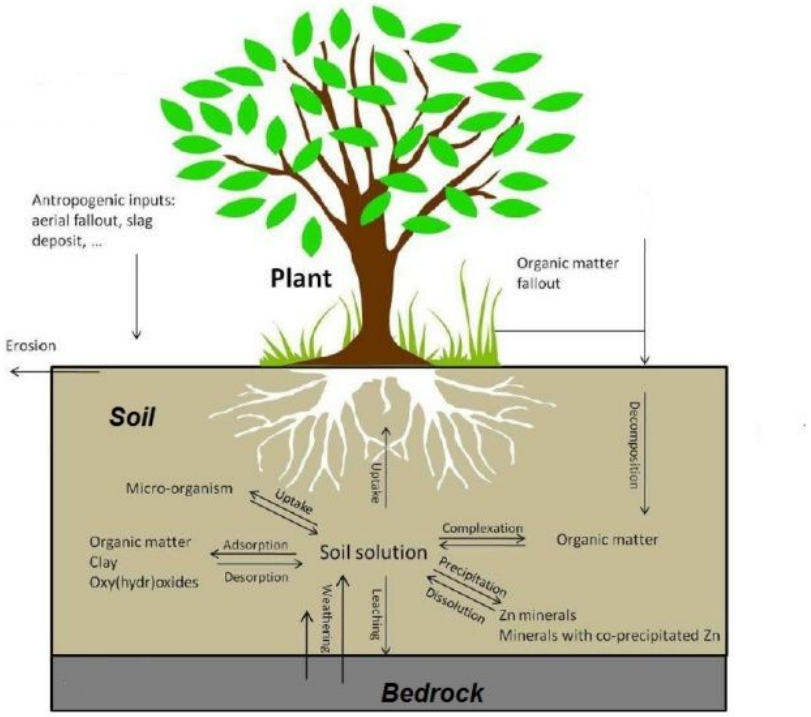

Figure 1. Scheme of the biogeochemical cycle of Zn (modified from Couder, 2013)

The inputs are mainly due to human activity and pollution and, in part, also to the degradation of organic matter. The main outputs are represented by erosion, leaching and plant absorption (Couder et al., 2013). Uptake of Zn from the soil is ruled by many factors such as pH of soil solution, chemical speciation, root exudates released to the rhizosphere, hydrologic and climatic conditions. Presence of Zn in soils can be due to natural geochemical background. In Italy, according to decree n°152 2006, the pollution threshold for Zn concentration in soil is 150 mg/kg in sites to be used for green both public and private residential, and 1,500 mg/kg in sites to be used for commercial and industrial purposes. However, the geochemical background of Zn in SW of Sardinia is anomalous due to widespread presence of ore deposits and mine wastes with concentration of Zn exceeding 20,000 mg/kg (Cidu and Fanfani, 2002; Medas et al., 2012; Bacchetta, 2015).

Zn ion can be included in mineral structures, precipitated, complexed with organic matter or bound to solid surfaces (adsorption) with increasing affinity to organic matter, clays and oxy(hydr)oxides (McLaughlin et al., 2000). Zn can form complexes – soluble or not, organic or not – in solution in addition to aquo ion (Zn^{2+}). At pH lower than 7.7, Zn is mainly present as Zn^{2+} while at higher pH, complexes such as $Zn(OH)^{+}$predominate (Fig. 2, modified from Lindsay, 1979). Zn chemical speciation is also strongly influenced by biological activity, as shown by a fairly large body of literature. Medas et al. (2014) investigated the effect that surface energy of nanometric biominerals has on thermodynamics, and found a tremendous impact of biological activity on stability field of some Zn bearing minerals in pe-pH diagrams (Fig. 3).

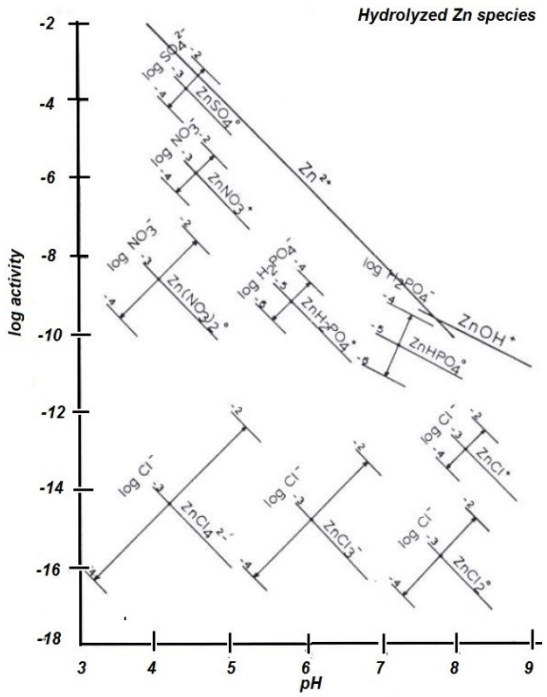

Figure 2. Hydrolyzed Zn species (Lindsay, 1979, modified)

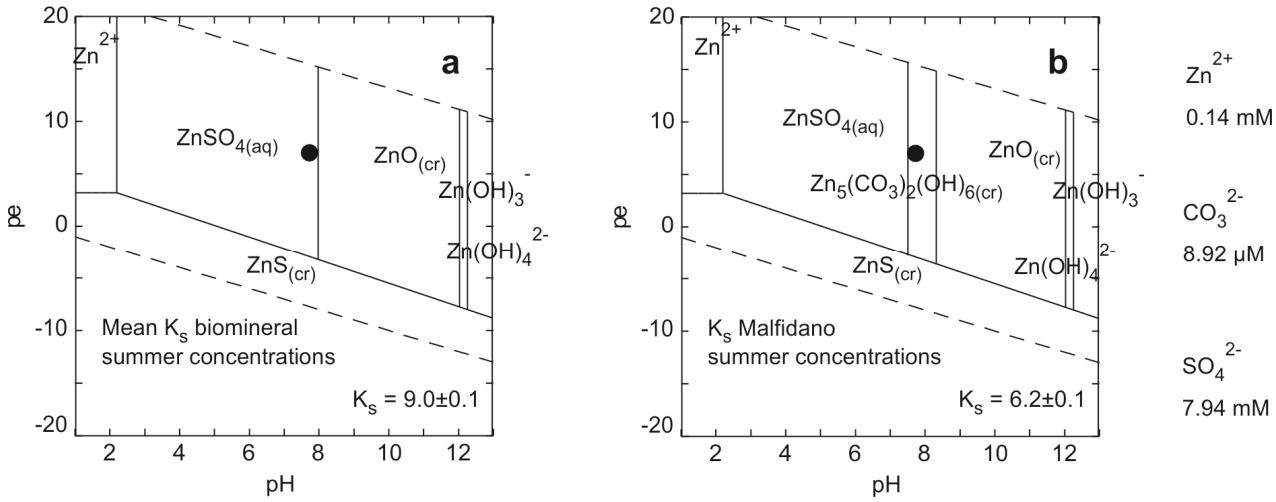

Figure 3 pe vs pH diagrams for the system Zn^{2+}–$Si(OH)_4^0$–$CO3^{2-}$–SO_4^{2-}–H_2O, from Medas et al,. 2014 modified.

1.2 Critical zone and role of plants in natural attenuation

In mine environments, dispersion and attenuation of trace metals can be mediated by processes occurring at the critical zone where water, sediments and biosphere meet. As the interface between surface and groundwater, the hyporheic zone of riverbed sediments is recognized as a critically important ecotone where biogeochemical reaction takes place (Byrne et al., 2010). Recently, some hydrological tracer studies found that water exchange between riverbed and hyporheic zone can be intense (Bencala et al., 2011; De Giudici, Pusceddu et al., 2017), affecting oxygen access to hyporheic zone, biogeochemical processes, the redox interface and, overall, trace metal dispersion.

In the last decades, phytoremediation has gained importance on account of its cost-effective, long-term applicability and because it is an ecofriendly, promising clean-up solution for a wide variety of contaminated sites (Weis and Weis, 2004). The research on vegetal species which can be useful in metal phytoremediation has become a major issue (Zhanget al., 2010) and these species should be chosen on the basis of their capacity to tolerate and accumulate particular contaminants (Marques et al., 2011).This method is based on the capability of some plants to extract, degrade or immobilize contaminants (Marques et al., 2011). The use of autochthonous plants for stabilization and pollution control is probably the most realistic and effective method to rehabilitate land affected by these threats (Ma et al., 2003). Hyperaccumulators are species capable of accumulating metals at levels 100-fold greater than those typically measured in shoots of common non-accumulator plants. Thus, an hyperaccumulator can attain up to 10,000 ppm Zn in aerial parts (Baker et al., 2000). Hyperaccumulator plants are able to take up exceedingly large amounts of one or more trace metals from the soil, and the trace metals are not retained in the roots but are translocated to the shoot and accumulated in aboveground organs (Rascio et al., 2011).

In this context, *Juncus acutus* is an hypertolerant species to Zn (Mateos Naranjos et al.,2014). Hypertolerant is a species or ecotype which can survive and reproduce on highly metal-enriched soils (Ernst et al.,2008). The capacity of *Juncus acutus* specie to accumulate great amount of Zn in its roots (>2,500 mg/kgZn) is associated to a capability to translocate and compartmentalize metal to stems (Mateos Naranjos et. al,2014). *Phragmites australis* has innate tolerance to Zn and other metals (Ye et al., 1997; Caldelas et al.,2011). The accumulation of Zn in roots, and the limitation of Zn export to the aerial compartments comprise an avoidance response that confers increased tolerance to Zn excess (Denny and Wilkins, 1987; Maestri et al., 2010).

1.3 Use of isotopes as proxies

The processes of Zn exchange in the water-soil-plant system is ruled by mechanisms that are still poorly known. To unravel them, isotope fractionation factors can be useful (Caldelas et. al., 2011; Borrock et al.,2007; Wanty et al., 2013) to understand better the mechanisms of Zn uptake, translocation, and tolerance in plants (Caldelas et al., 2016) and how these react to the environment and mechanisms of Zn absorption, transport, and sequestration in plants (Tang et al., 2016). Moreover, the stable Zn isotope fractionation in higher plants could be a useful tool for tracing the physiological processes involved in Zn homeostasis, actually, isotope fractionation by plants changes in response to Zn availability in environment (Caldelas et al., 2016).

Zn has five stable isotopes, ^{64}Zn, ^{66}Zn, ^{67}Zn, ^{68}Zn and ^{70}Zn. Their average relative abundances in Nature are 48.98, 27.81, 4.11, 18.57 and 0.53 %, respectively (Rosman andTaylor, 1998). The isotopic results are expressed in standard delta notation (in units of ‰) relative to the average of the bracketing standards (i.e., JMCave), as shown in Eq. (1).

$$\delta^{66}Zn = \left[\frac{(^{66}Zn/^{64}Zn)_{sample}}{(^{66}Zn/^{64}Zn)_{JMCave}} - 1\right] \times 1000 \qquad \text{Eq. 1}$$

Weiss et al. (2005)performed the first analyses of Zn isotopes in plants, and found that shoots were isotopically lighter with respect to roots, and roots isotopically heavier with respect to solution. The magnitude of fractionation changed with increasing Zn supply from –0.2‰ to –0.8‰. Viers et al. (2007) studied several plant species in a pristine watershed, and found a significant difference in fractionation factors between species and between plant organs of the same species, which they ascribed to root uptake from soil and translocation within the plants.

The leaves of the tallest species had the most negative isotopic signatures, and they hypothesized a correlation between the length of the plants and the extent of Zn fractionation. Caldelas et al. (2011) observed that the enrichment in light Zn isotopes of shoots and leaves is consistent with long distance root to shoot transport in *Phragmites australis*.

1.4 Overview

In the Sulcis-Iglesiente-Arburese area (SW Sardinia), mines have been for centuries the most important economic activity. Closure of the mines left a rich heritage of industrial archaeology but also a deep impact on the environment that is still in need of remediation. Mining activity involves significant transformations of physical geography, exposes large mineralized areas to exogenous alteration, increasing the risk of contamination, produces changes in the water chemistry and mineralogy of soil for an undetermined length of time. Thus, abandoned mine areas represent a serious environmental threat. In Sardinia, several different wastes are widespread in Sulcis-Iglesiente-Arburese and other relevant mine areas. In particular, abandoned flotation mud from

settling ponds, wastes from rock dumps and contaminated streams can be still recognized (Cidu and Fanfani, 2002; https://www.regione.sardegna.it/documenti/1_117_20141020101403.pdf).

As previously mentioned, historical mining areas are perturbed systems that are still in evolution. The fate of pollutant sources and their temporal evolution can be investigated with specific tools comprising mass balances and hydrological tracer techniques (Kimball et al. 2002 for a review), isotopic and microscopic investigations, also with synchrotron techniques (Caldelas et al., 2011; Wanty et al. 2012; Gardea-Torresdey et al., 2005; Medas et al. 2015; De Giudici et al. 2015). As for a common target of many investigations, natural attenuation processes reveal how the natural systems evolve in response to the perturbation due to pollutant dispersion form mine areas.

The purpose of the present study is to investigate some of the processes occurring in the hyporheic zone, where plants meet sediments and mine waste with water and microbes. This study scales down from the catchment scale to microscopic scale mechanisms. The basin of the Rio San Giorgio (SW, Sardinia) was selected for the catchment scale investigation. The riverbed of Rio San Giorgio is characterized by the presence of a natural dense vegetation comprising mainly *Juncus acutus* and *Phragmites australis*. The riverbed sediments are mine wastes with up to 1-2 % in Zn and Pb (http://www.sardegnaambiente.it/index.php?xsl=612&s=169247&v=2&c=4807&idsito=18).

Growth of selected plants (*Juncus acutus* and *Phragmites australis*) and microscopic processes was investigated under greenhouse conditions in rhizobox experiments (Hylander, 2006).

Microscopic processes were investigated using facilities available at the University of Cagliari and facilities from different European research centres through the CERIC-ERIC (an European Consortium whose members are the Governments of 6 European Countries: Italy, Austria, Czech Republic, Romania, Serbia and Slovenia). The vision of CERIC-ERIC consists in offering a framework of multidisciplinary and multinational research within the European Research Area, open, based on competition, to scientists from all over the world, to favour excellence, innovation

and integration at the European level. Zn isotope fractionation and Zn mass exchange between water, plants and substrate was investigated. The support of United States Geological survey was very useful for both catchment scale investigation and isotopes investigation.

1.5 Main objectives

This work is guided by these questions:

1) What is the extent of natural attenuation processes, can they be quantified?

2)How water, plants and substrates interact to mitigate mobility?

3)What lessons can be drawn from these systems for land management?

Through a multiscale and multimethod approach this work investigates:

1) physical and biogeochemical processes occurring in a mine-polluted stream, Rio San Giorgio, where the streambed is characterized by a vegetation-rich environment. Investigation of the system plant-soil-water.

2) role of plant, substrate and water in a controlled system (rhizobox experiment) and in natural catchment to understand mechanism of bio-geosphere interaction.

Chapter 2- Study Area

Field study was performed in SW Sardinia, specifically in the San Giorgio area (Fig. 4), close the town of Iglesias. In addition, some plants and substrate for rhizobox experiment were collected from Naracauli area, close the town of Arbus (sse Appendix I).

Figure 4. Map of SW San Giorgio area (satellite photo from Google Earth).

2.1 Geological setting and hydrological data

San Giorgio area is located in the External Zones of the Hercynian orogeny (Carmignani et al., 1997), where geology (Fig. 5) is mainly represented by Cambro- Ordovician autochtonous unit. This geological succession, from the bottom to the top, consists in: Nebida Group, represented by silicoclastic, shallow-water sediments, with carbonate intercalations toward the top; Gonnesa

Group, containing shallow-water platform carbonates; Iglesias group represented by nodular limestones and slates.

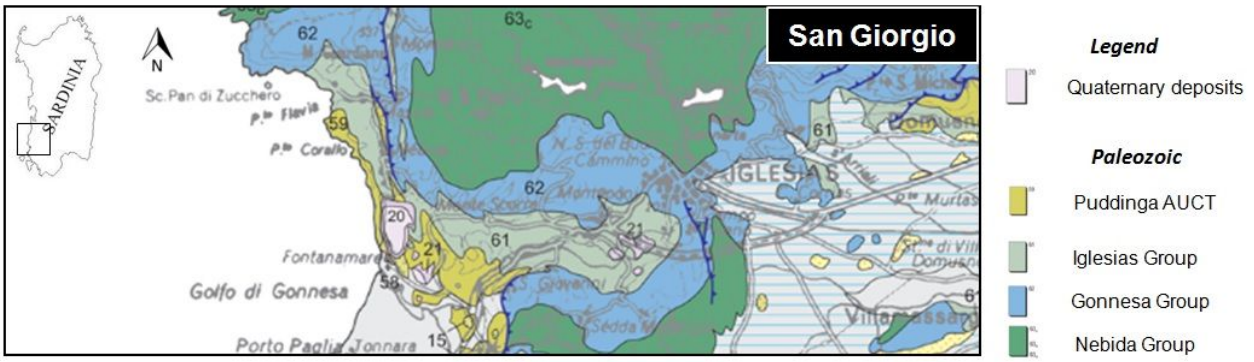

Figure 5. Geological map of San Giorgio Area, (Carmignani et al, 1997, modified)

During the intra Ordovician "Sardic" tectonic phase, sediments of Cambrian to Lower Ordovician were subjected an extensive deformation (Boni, 1999). This phase is followed by erosion and deposition of Upper Ordovician sediments in angular unconformity. These deposits consist of thick successions of continental conglomerates and sandstones (‘Puddinga’ AUCT.), followed by marine slates, lasting until Late Ordovician–Silurian time. The Variscan orogeny produced at least two compressional phases and one extensional phase of deformation (Carmignani et al., 1997). The Variscan deformation also produced low-grade metamorphism and several phases of magmatic intrusion, which affected the deformed Paleozoic successions (Boni et al., 1999). Several pulses of extensional tectonics caused repeated opening of fractures and circulation of hydrothermal fluids during the Permian and the Mesozoic (Boni et al., 1999).Along the south-western coast a Tertiary volcanic to rhyolitic and rhyodacitic types rock are represented by Oligo–Miocene andesitic. Quaternary sediments are represented by conglomerates of fluviatile origin and Holocene sand dunes characterize the coastal belt northwest of Gonnesa.

Information on geology and ore deposit of Naracauli area are reported in Appendix 1.

The climate of the SW of Sardinia is characterized by dry periods usually extending from May to September with wetter autumn and winter. Based on data collected from 1922 to 1992, rainfall has a mean value of 723 mm for Naracauli area and 804 mm for San Giorgio area, and the mean annual temperature is 17°C for both areas.

2.2 Ore deposits and mine activity

Ore deposits in San Giorgio area are stratiform or strata bound and they are referred at lower Cambrian. They consist partly of massive sulphides (Sedimentary Exhalative) content in salty dolomites, and partly of lower-grade sulphide concentrations (Mississippi Valley type) content in limestones (Boni et al., 1999). The metallic minerals are sphalerite–galena barite with variable pyrite contents, As-rich pyrite is dominant in the massive sulphides. Sphalerite contains Fe and Cd–Ge; low grades of Ag accompany the strata bound galena. Along the Nebida coast and on the San Giovanni–San Giorgio and Barega hills are common low temperature base metal- barite veins. They consist in simple ore mineral association of Ag-rich galena and barite, the age of these mineralizing events is probably between Permian and Mesozoic. During Phoenicians and Romans period and then in the Middle Ages deposits was exploited due to high Ag contents. The ores consisting mostly of smithsonite, hydrozincite (the so-called 'Calamine') and cerussite and, near the surface, are generally oxidized bodies. These ores, were extensively exploited up until the sixties.

Currently, San Giorgio area (Fig. 6) is affected by a high mine pollution, there are 17 million cubic meters of open pit excavations, 12 million cubic meters of dump and tailings (RAS, 2003; http://www.sardegnaambiente.it/index.php?xsl=612&s=169247&v=2&c=4807&idsito=18).

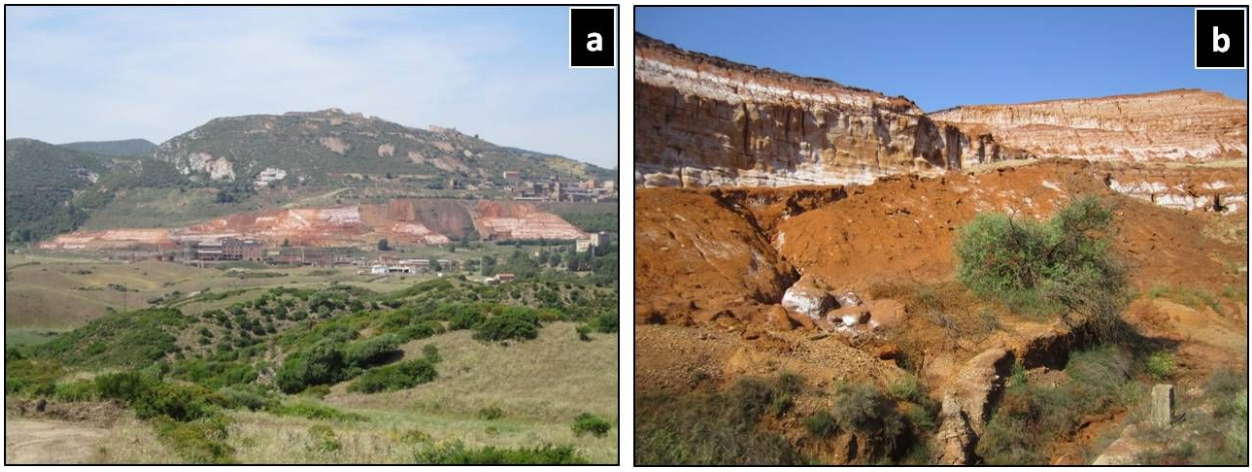

Figure 6. View of San Giorgio area (a), zoom in Fanghi rossi (b)

Chapter 3-Materials and Methods

3.1 Catchment scale investigation: Tracer techniques

The mass-loading approach has been used to quantify metal loads from abandoned and inactive mines and to support science-based decisions for remediation of stream catchments. The approach is based on continuous injection of a conservative tracer and synoptic-sampling methods that were developed in a series of studies for determining mass loading in mine-drainage streams (Kimball et al. 2002, Bencala et al. 2011). The mass-loading approach is used to quantify the influx of metals from various sources and to quantify the extent of biogeochemical reactions in the stream (De Giudici et al. 2014). The tracer-injection technique involves several steps: detailed characterization of the stream to select sampling sites for mass-balance accounting, injecting a salt solution with a known concentration of tracer at a constant rate and monitoring the approach to ”plateau” concentration at selected sampling sites downstream. When the stream and hyporheic volume become saturated with tracer, synoptic sampling is conducted over a short time period to obtain a spatially-dense profile of discharge and chemical composition.

Inflows of water, either from tributaries or discharging groundwater, dilute the tracer along the stream. Stream sampling sites were selected both upstream and downstream from observed inflows to constrain the mass contribution of each inflow to loading. Each pair of stream sampling sites along the study reach represents a stream segment, and the mass balance between the two sites accounts for the net loading or removal for that segment of the study reach.

Quantifying tracer dilution allows calculation of stream discharge based on the conservation of the injected tracer mass. Chloride and Br salts of Li or Na typically are suitable tracer, but in streams with higher pH Cl and Br work well (Kimball et al., 2002, Bencala et al. 2011). In Rio San Giorgio,

NaBr was chosen as the tracer salt. It was determined the rate of injection and the concentration of Br. The mass of Br that injected volume was measured and its specific gravity provided the concentration and the volume. It was also analysed water chemistry from the synoptic samples and calculated heavy-metal loads along the stream profile multiplying concentration of metals to discharge. More details of the tracer-dilution methods are described in Kimball et al. (2002).

The tracer-dilution method can identify the location of surface water and groundwater inflows for each of the stream segments. However, the method cannot identify losses of stream flow because as stream water with Br tracer leaves the stream, the in-stream concentration of Br does not change. Recent works have focused on quantifying gain and loss on small streams (Payn et al. 2009; Bencala et al 2011; Runkel et al. 2013). To allow a correction to the tracer-dilution discharge due to possible loss of stream flow have been used a slug injection method. This is a punctual and accurate measurements of discharge that use dry salt instead of salt solution and it is easily repeatable (Moore, 2005).

Three slug injections were used on the day of synoptic sampling (Kimball et al. 2002) to allow a correction to the tracer-dilution discharge due to possible loss of stream flow.

Tracer of San Giorgio river was performed on June 2012 under the supervision of Dr Kimball (USGS) in collaboration with Dr. Richard Wanty (USGS) from members of group of Mineralogy and Geochemistry Environmental Department of Chemistry and Geology, University of Cagliari.

3.1.2 Water samples collection and analysis of San Giorgio river catchment

A combination of 19 stream sites and 8 inflows were selected for synoptic sampling along the Rio San Giorgio study reach (Fig.7 and Table 1). Five sampling points along the stream were selected as "transport" sites (T sites), and were monitored before, during, and after the Br tracer attained a plateau. The T sites were chosen so as to monitoring transport of tracer in each part of the stream.

Synoptic sampling of the 19 stream points was carried out on 4 June 2012 after four days of continuous bromide injection (Syn. 9).

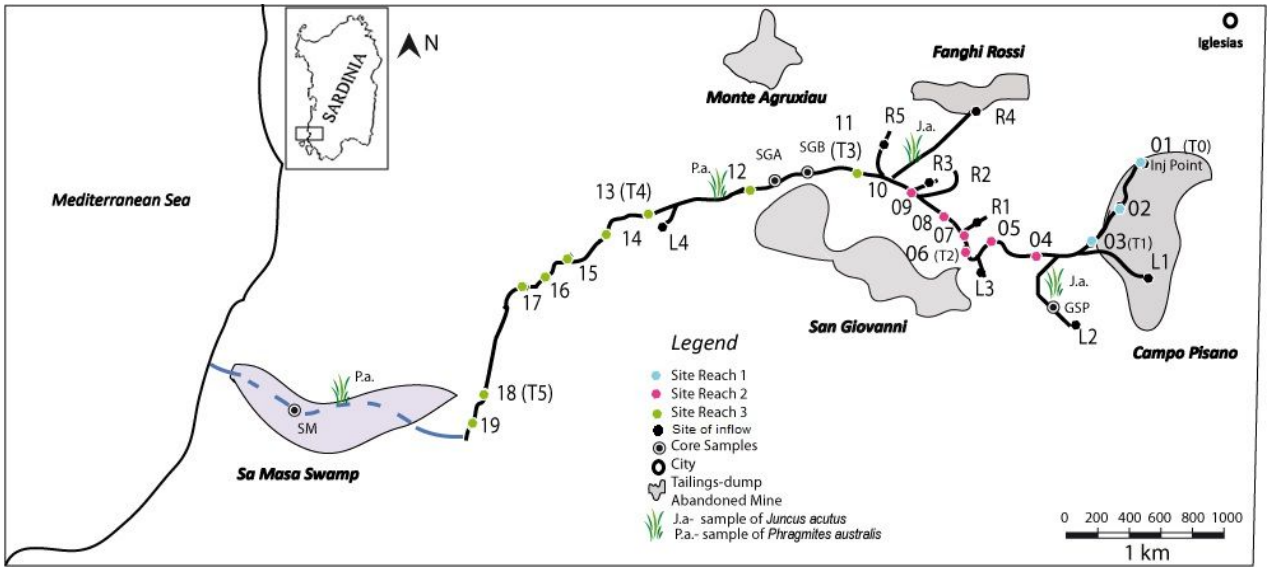

Figure 7. Map of San Giorgio area showing the location of water samples sites, core samples, plant samples (J.a - Juncus acutus, P.a. Phragmites australis), and the distribution of mine tailings (from De Giudici al., 2017 modified)

This synoptic sampling started at 9 AM, and lasted about 4 hours. Owing to the logistics of the tracer study, it could not collect all 19 samples at the same time, to be truly synoptic. A second, true synoptic sampling (Syn. 17) was conducted at the same day at 5 PM, sampling only 13 sampling sites, including the five T sites. Inflow sites were sampled on 3 June. At the headwaters of the Rio San Giorgio, a 183,200 mg/l Br solution was injected into the stream at a constant rate of 30 ml/min (using the median of 9 injectate samples). The tracer concentration achieved a steady state along the study reach after 72 h of continuous injection.

A study of diel variation in stream chemistry was carried out by repeated sampling over 48 hours at two fixed stations in Rio San Giorgio at 3–6 hour intervals. For the diel study, temperature, pH and conductivity were determined in situ at the time of sampling. Alkalinity was determined in the field by the Gran titration method (Gran et al., 1950) within two hours of sampling. Temperature was determined using a precision thermometer (Checktemp HI98509-01, Hanna Instruments), and pH

was measured with a Ross electrode and a pH meter (Orion, Thermo Fisher Scientific, USA), after calibration against NIST buffer solutions. Conductivity was determined by a conductivity meter (HI98303, Hanna Instruments). For both the diel and synoptic samples, four aliquots of each sample were processed: a 0.45-µm filtered, unacidified sample for anions determined by ion chromatography; two 0.45-µm filtered aliquots acidified to 1% v/v with high purity HNO_3 for metal analysis by inductively coupled plasma optical emission spectroscopy (ICP-OES) and inductively coupled plasma mass spectroscopy (ICP-MS); and an unfiltered aliquot acidified to 1% by volume with high purity HNO_3 acid for total-recoverable metals analysis. For the synoptic samples, an additional unfiltered, unacidified sample was collected for alkalinity, which was determined in the laboratory by Gran titration within 3 days of sample collection. The detection limit (DL) for chemical elements was calculated at 10 times the standard deviation of the blank solutions. To evaluate the accuracy and precision of trace-element determination, two reference solutions were used: the NIST SRM 1643e and the EnviroMAT Ground Water ES-L-1. Rhodium was used as an internal standard for ICP-MS analysis to correct for instrumental drift. The ionic balance was always better than ± 10%, as confirmed using PHREEQC (Parkhurst and Appelo, 1999)

Table1. Distance (m), source and coordinates of sampling sites along Rio San Giorgio (S) and on tributaries located on the left (LBI), and on the right (RBI) of the stream. T1-5 indicate the transport sites.

Site ID	Distance (m)	Source	Latitude N	Langitude E
01	0	S	39°17'38.35937"	08°30'59.53696"
02	283	S	39°17'30.09649"	08°30'53.87483"
03 ^{T1}	610	S	39°17'21.82390"	08°30'45.91728"
L1	680	LBI	39°17'21.46680"	08°30'53.60042"
L2	900	LBI	39°17'09.88963"	08°30'38.90403"
04	931	S	39°17'17.74898"	08°30'33.42288"
05	1234	S	39°17'19.99911"	08°30'20.92617"
L3	1390	LBI	39°17'17.34163"	08°30'13.89044"
06 ^{T2}	1397	S	39°17'18.57798"	08°30'14.75830"
07	1558	S	39°17'21.29218"	08°30'12.27634"
R1	1580	RBI	39°17'25.64750"	08°30'14.29100"
08	1650	S	39°17'26.72053"	08°30'07.31225"
09	1840	S	39°17'27.92751"	08°30'01.33434"
10	1941	S	39°17'30.05560"	08°29'58.35538"
R2	2099	RBI	39°17'38.54557"	08°30'03.84710"
R3	2100	RBI	39°17'31.32424"	08°29'59.18124"
R4	2100	RBI	39°17'27.52845"	08°29'14.41723"
11^{T3}	2312	S	39°17'33.78772"	08°29'43.75990"
R5	2350	RBI	39°17'39.82247"	08°29'44.05055"
12	3024	S	39°17'27.52845"	08°29'14.41723"
L4	3650	LBI	39°17'23.11199"	08°28'51.40731"
13^{T4}	3686	S	39°17'22.90374"	08°28'48.36161"
14	4000	S	39°17'17.95046"	08°28'36.08431"
15	4317	S	39°17'11.31899"	08°28'25.78189"
16	4492	S	39°17'08.98585"	08°28'19.16259"
17	4656	S	39°17'04.97596"	08°28'14.76826"
18^{T5}	5357	S	39°16'43.52064"	08°28'04.66254"
19	5577	S	39°16'37.05094"	08°28'01.49786"

3.2 Plant and rhizosphere samples collection and analysis

Samples of plant from this study include leaves, stem and root of *Phragmites australis* and *Juncus acutus* collected both in the Naracauli district (see Appendix 1) and San Giorgio district (see fig.4). The case of Naracauli was studied in De Giudici et al. 2009; Medas et al. 2012; Wanty et al. 2012; De Giudici et al. 2014. Additional plants of *Juncus acutus* and *Phragmites australis* were collected from rhizoboxes. These plants were grown in three different substrates, two of these were mine substrates from Naracauli area and from San Giorgio area and the third was an unpolluted substrate, and watered with polluted and unpolluted water (see paragraph 3.3). According to the commonly accepted protocol (Barbafieri et al., 1996.), plants were washed with deionized water(Fig. 8) until the water in which they were immersed has not become completely clear, and dried in stove at 40°C. As the target of the research was the biomineralization processes at the root surface and inside the roots, an aliquot of the root samples was analysed with and without washing for Scanning electron microscopy and X-Ray Absorption Spectroscopy analysis.

Figure 8Images of plant samples: dirty roots of Juncus acutus (a,b), first wash of stem of Juncus acutus (c), cleaned leaves of Phragmites australis, still wet (d)

Solid samples include rhizosphere of *Phragmites australis* and *Juncus acutus* collected by both surface (up to 40 cm) and core sampling (up to 3 meters). The core sampling of alluvial sediments (Fig. 9) was carried out with a core sampler that allowed recovery of samples in sealed plastic bags (Atlas Copco's COBRA).

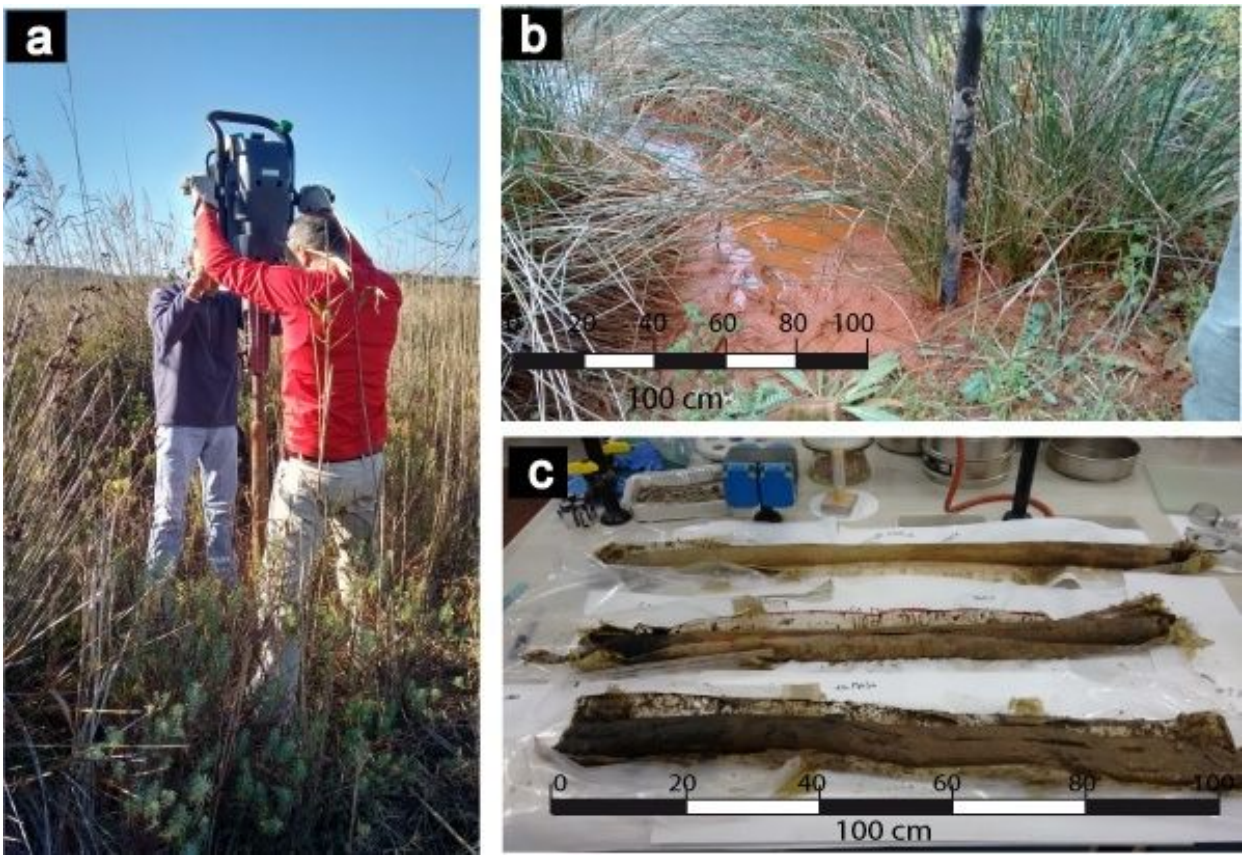

Figure 9: Core Samples carried out with Atlas Copco's COBRA (a) in the riverbed (b), and samples recovered in sealed plastic bags and analyzed in laboratory(c)

3.2.1 X-Ray Diffraction and Scanning Electron Microscopy

After drying at room temperature, 200 mg of powder of substrates of rhizobox and core samples were lightly ground in an agate mortar and subjected to X-ray diffraction (XRD) analysis, using a conventional θ–2θ equipment (PANalyticalXpert Pro) with Cu Kα wavelength radiation (λ=1.54060 Å), operating at 40 kV and 40 mA, using the X'Celerator detector .

Scanning electron microscopy (SEM) imaging and energy dispersive spectroscopy (EDS) analyses were carried out using an environmental scanning electron microscope (ESEM QUANTA 200, FEI).

3.2.2 Chemical analysis of plant and rizosphere materials.

For chemical analysis, plants were divided in leaves, stem and roots. Based on the features revealed by SEM analysis and because preliminary analysis indicated Si, Al, Fe and Zn are more concentrated in the external layer of the root, the root were divided into sub samples hereafter referred as the external surface of root and the internal part. Then they were lightly ground in electric grinder (Fig. 10). According to the commonly accepted protocol (Barbafieri et al., 1996., EPA 3052), elemental characterization of the plants was carried out on 0.5 g of each dry sample. A high-purity mixture of 2.5 ml of Milli-Q water (<0.1 μS/cm), 2 ml of H_2O_2, 0.5 ml of HF, and 5 ml of HNO_3, was added to the solid into microwave vessels. Samples were processed together with a blank and a reference material (SRM 1573a, tomato leaves) prepared with the same mixture. Acid digestion was performed by the microwave ETHOS One, Advanced Microwave Digestion System, Milestone. After cooling, the mixture was transferred into a Teflon beaker rinsing the vessel with a few ml of Milli-Q water. This mixture was heated in a hot-plate (~4 h, 150°C); following evaporation, 3 ml of concentrated HNO_3 were added for three times. Finally, the mixture was filtered (0.4 μm), and the solution was made up to 25 ml final volume using Milli-Q water. Zn was determined by ICP-OES.

For chemical analysis of substrate each sample was lightly ground in an agate mortar. Elemental characterization was carried out on 0.25 g of each sample. A high-purity mixture of 2 ml of Milli-Q water (<0.1 μS/cm), 2 ml of H_2O_2, 3 ml of HF, and 12 ml of aqua regia, was added to the solid into microwave vessels. Samples were processed together with a blank and a reference material (NIST

2710, Montana Soil) prepared with the same mixture. Acid digestion was performed by the microwave ETHOS One, Advanced Microwave Digestion System, Milestone. After cooling, the mixture was transferred into a Teflon beaker rinsing the vessel with a few ml of Milli-Q water. This mixture was heated in a hot-plate (~4 h, 150°C); following evaporation, 3 ml of concentrated HNO_3 were added for three times. Finally, the mixture was filtered (0.4 µm), and the solution was made up to 50 ml final volume using Milli-Q water. Zn was determined by ICP-OES.

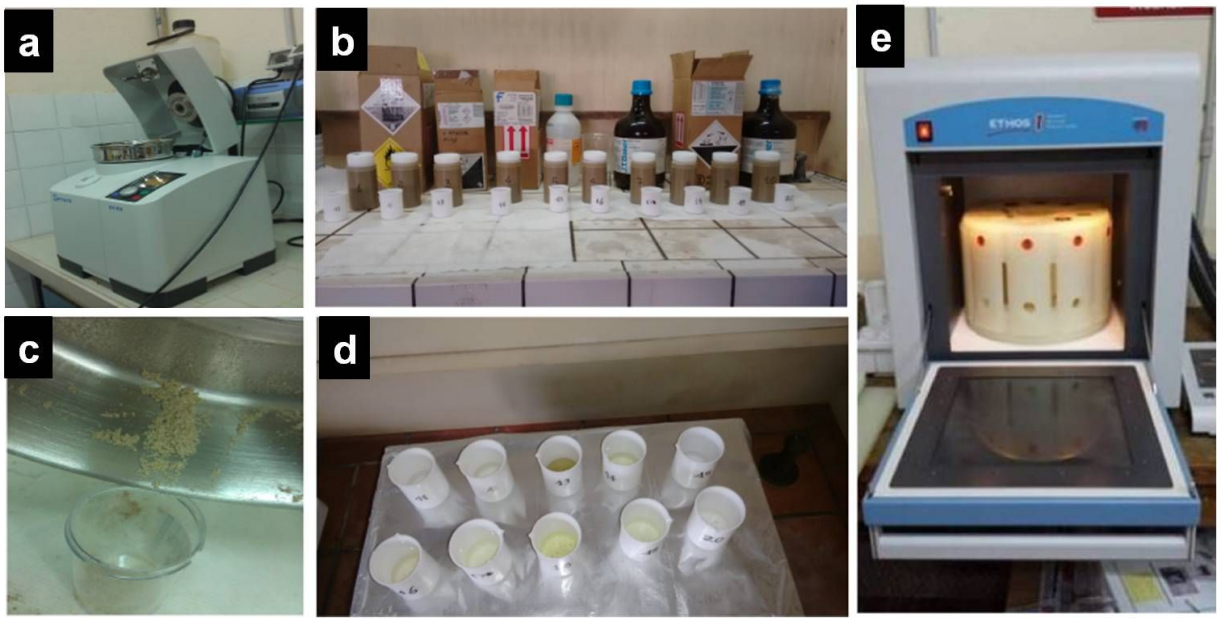

Figure 10 Preparation for chemical analysis of plants: each samples was lightly ground in electric grindel(a) after ground, samples(c) were digest in Advanced Microwave Digestion System (b,e)then solution of each sample was heated in a hot-plate (d)

3.2.3 Soft X-ray Microscopy

For soft X-ray Microscopy analysis (Elettra, Trieste), samples were dehydrated in a graded series of ethanol solutions (50, 75, 90 and 100 %) then they were washed in xylene. Each steps lasted 30 minutes and was carried out at room temperature. Samples were infiltrated overnight in liquid paraffin wax at 60 °C and the infiltrated roots were then embedded into paraffin blocks. At last, sections of 14 µm were cut with a microtome (Micron) and collected on ultralene films.

TwinMic instrument is a soft x-ray microscope operated at the Elettra synchrotron in Trieste, in the x-ray range 400 and 2200 eV (Gianoncelli, 2013), combined with low-energy XRF mapping analyses.

When TwinMic is operated in Scanning X-ray Microscopy mode (SXM), the Light Elements XRF system is used, in this case the microprobe down to sub-100 nm size is provided by a zone plate diffractive optics and the sample is raster scanned across the microprobe. The transmitted X-rays are collected by a Fast Readout CCD camera through a X-rays-visible light converting system while the emitted XRF photons are recorded by the LEXRF system.This provides simultaneously the morphological information through absorption and phase contrast images, and elemental maps generated by the LEXRF system.

The X-ray beam energy for these analysis was 1.985 keV. It was chosen to ensure the best excitation and detection of Si, Al, and Zn, with a spatial resolution (X-ray spot size) of 1 μm x 1 μm, as a compromise between good XRF signal and dimension of the features of interest. The XRF elemental maps were deconvoluted and analysed with PyMCA software.

3.2.4 Materials Characterisation by X-ray diffraction (MCX)

The beamline Materials Characterisation by X-ray diffraction MCX is aimed at the characterisation of various materials, with an experimental station allowing the structural analysis of organic and inorganic thin films, highly disordered materials in the form of films, powders and fibres.

The MCX station is based on a 4-circle diffractometer in full circle configuration with a flat sample-holder plate (Ø 100 mm) controlled by a precision (1 μm) x-y-z motor system, 360◦. The powder pattern is recorded by a translating image plate, as a fast data collection system to follow phase transformations and chemical reactions. (Lausi et al, 2015).

After drying at room temperature, few mg of powder of each sample were lightly ground in an agate mortar (Fig 11) and subjected to x-ray powder diffraction analysis (S-XRPD). Samples were placed in quartz capillary tubes with an inner diameter of 2 mm and placed inside a furnace to perform the measurements at 25° C. These analysis were made in Elettra, Trieste.

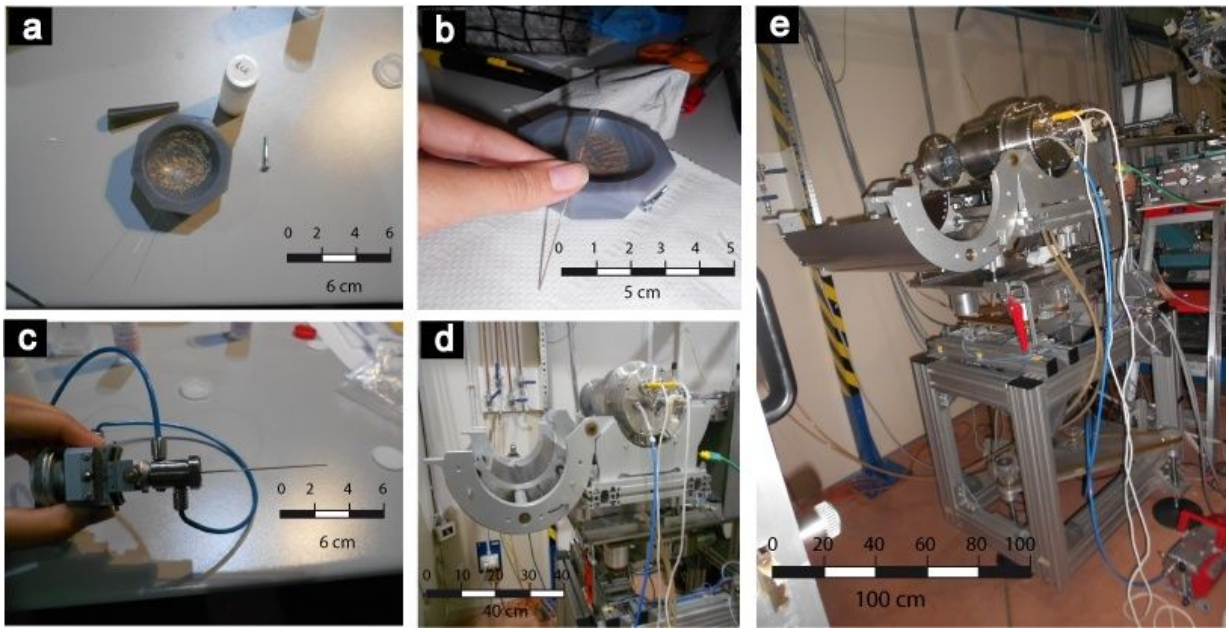

Figure 11Few mg of samples (a) were placed in quartz capillary (b) then sample was fixed in particular support (c) and it was inserted in the instrument (d,e)

3.2.5 X-Ray Absorption Spectroscopy

X-Ray Absorption Spectroscopy (XAS) experiments were carried out in the regions of Zn K-edge (E_{ZnK} = 9.659 eV), and Fe K-edge (E_{FeK} = 7.112 eV) at the ELETTRA-XAFS beamline (Trieste, Italy). The plant samples and rhizosphere materials were dried at about 30°C and ground immediately after their collection. Then samples were transported under anoxic conditions for XAS analysis. At the XAFS beamline, samples were pressed in solid pellets, and the XAS measurements were carried out in transmission and fluorescence geometry keeping the samples at the liquid

nitrogen temperature. Zn K-edge XAS spectra were also measured in transmission geometry on a set of reference compounds (Table 2) for sake of comparison and used for XANES interpretation by linear combination analysis (LCA, Benfatto and Meneghini, 2014).

Standard procedures (Rehr and Albers, 2000) were used for XAS data normalization and extracting the structural EXAFS (Extended X-ray Absorption Fine Structure) signal $\chi(k)$ using ESTRA code (Meneghini et al., 2012); these procedures include pre-edge linear back-ground removal, spline modelling of bare atomic background μ_o, and edge step normalization. Third degree polynomial splines were used to model the post-edge background μ_o. The photoelectron wave vector modulus k, was calculated choosing the edge energy at the first inflection point (first derivative maximum) of the absorption spectrum, and refined during the data fitting (ΔE).

The EXAFS data refinement was performed using the FITEXA code (Meneghini et al., 2012) for data fitting and statistical error analysis. Data refinement was performed on the raw k-weighted $k\chi(k)$ spectra (i.e. without Fourier filtering), the model curves are calculated applying the standard EXAFS formula (Rehr and Albers, 2000) with Gaussian neighbour distributions. Model atomic clusters obtained from crystallographic models (ICSD) were used to individuate the main structural contributions and calculate theoretical amplitude and phase functions with FEFF 8.4 code (Ankudinov et al., 1998, Zabinsky et al., 1995). Relevant contributions to the best fit were selected from the model clusters, accordingly to the expected composition given from LCA results. In principle, for each spectrum, edge energy shift (ΔE), coordination numbers (CN), bond distances (R) and mean square relative displacement (MSRD) factors (σ^2) can be refined for each contribution (coordination shell). However physical constraints were applied in order to reduce the number of free parameters and the correlations among them, in particular, in each fit, the same ΔE was applied to all considered shells, fitting the Zn-hydroxyapatite data it was fixed CN to the crystallographic values.

Table 2. Reference compounds analysed by XAS

Name	**Formula**
Smithsonite	$ZnCO_3$
Zn sulphate monohydrate	$ZnSO_4 \cdot H_2O$
Zn sulphate heptahydrate	$ZnSO_4 \cdot 7H_2O$
Zn oxide	ZnO
Hydrozincite	$Zn_5(CO_3)_2(OH)_6$
Hemimorphite	$Zn_4Si_2O_7(OH)_2 \cdot H_2O$
Willemite	Zn_2SiO_4
Sphalerite	ZnS
Zn phosphate	$Zn_3(PO_4)_2$
Zn citrate	$Zn_3(C_6H_5O_7)_2$
Zn hydroxyapatite	Zn in $Ca_5(PO_4)_3(OH)$
Zn acetate dehydrate	$Zn(O_2CCH_3)_2(H_2O)_2$
Zn acetate anhydrous	$Zn(O_2CCH_3)_2$
Zn cysteine	Zn in $C_3H_7NO_2S$

3.2.6 CHN analysis

The carbon, hydrogen and nitrogen contents in substrates were determined by using an elemental analyzer (CHN-1000, LECO Corporation, MI, USA). The sample was placed in a tin capsule and inserted in the furnace at 1000 ° C in excess of oxygen, then products of combustion were passed into a second furnace at 850 ° C. The gases were collected and homogenized in the ballast, then sent to detectors. Samples were processed together with a reference material (Orchard Leaves, Nist SRM 2691) prepared in the same mode.

3.3 Plant growth under controlled conditions: Rhizobox System

Rhizobox experiments were performed in the greenhouse " VivaiMurgia ", near to the town of Villacidro (SW Sardinia).This company provided plants, grown from seeds collected in mine polluted areas. The botanical support was provided by Dr. Agr. V. Murgia. Rhizobox system is commonly used in the literature (Hylander et al., 2006); the term rhizobox refers to a microcosm where the growth of plants under controlled conditions can be visually inspected.

The rhizoboxes used in this study were made up of transparent plexiglass having a length of 200 mm, a height of 300 mm and a width of 50 mm. The transparent sides of the rhizoboxes allowing visual inspection of the root growth were covered by removable strips of dark fabric in order to protect the roots from light.

Thirty rhizoboxes were divided into two groups (A and B) and were disposed in two wooden supports (Fig. 14d). In the bottom of each rhizobox, in correspondence of the water drain hole, a funnel was positioned to simplify the water sampling.

The rhizoboxes were filled by tree different substrates (Fig. 12 and Fig 13), two of these were mine substrates from Naracauli area (Naracauli substrate),and from San Giorgio area (Sa Masa substrate) and the third was an unpolluted substrate (Zn concentration was below <150 ppm, provided by "Vivai Murgia").Substrates were sieved at 2 mm, 2 kg of substrates were mixed with1 kg ofpozzolana, to improve their permeability. After mixing, each box was filled with the mixture.

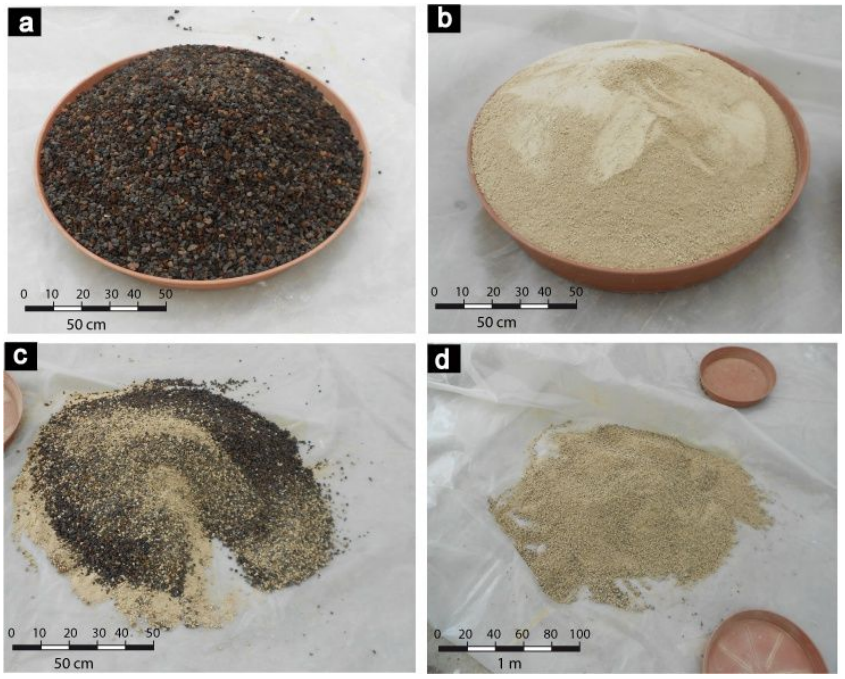

Figure 12. Preparation of substrates: pozzolana (a) were mixed with substrate (b), this mixture (c) was stirred until it became homogeneous

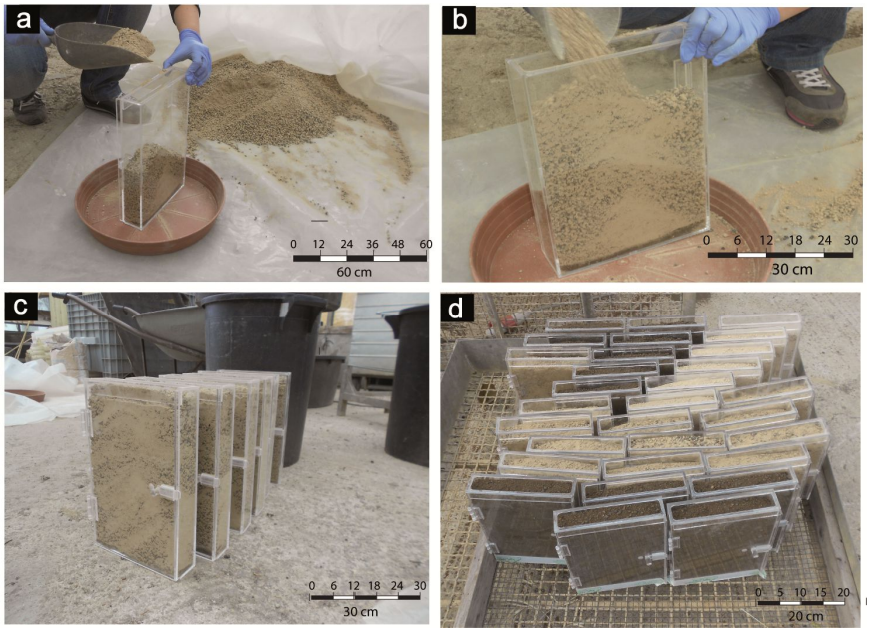

Figure 13. Preparation of rhizobox: mixtures were insert in rhizobox (a) until total filling(b). View of some rhizoboxes filled with Naracauli substrate(c), view of the thirty rhizoboxes (d)

As previously noticed, in order to increase the chances for plants to growth with high metal concentrations (Sprocati et al. 2014; Kothe and Buechel 2014), plantlets were obtained from seeds collected by Vivai Murgia from plants growing in mine-polluted areas. Plantlets were grown up to

5-10 cm in an unpolluted substrate, then transferred in rhizoboxes after gently cleaning their roots from grain of the initial substrate. Two plantlets were transplanted per each box (Fig. 14).

Watering was provided every 48 hours according to the seasonal conditions (max temperatures up to 35°C in August). All the water seepage from the bottom of the rhizobox, that is some excess of water exceeding the water retention capacity of the systems, was collected for all the rhizoboxes. A funnel was positioned in the bottom of each rhizobox, in correspondence of the water drain hole, to simplify the water collection. Water sampling was monthly carried out to check for water quality after interaction with soil minerals and plants.

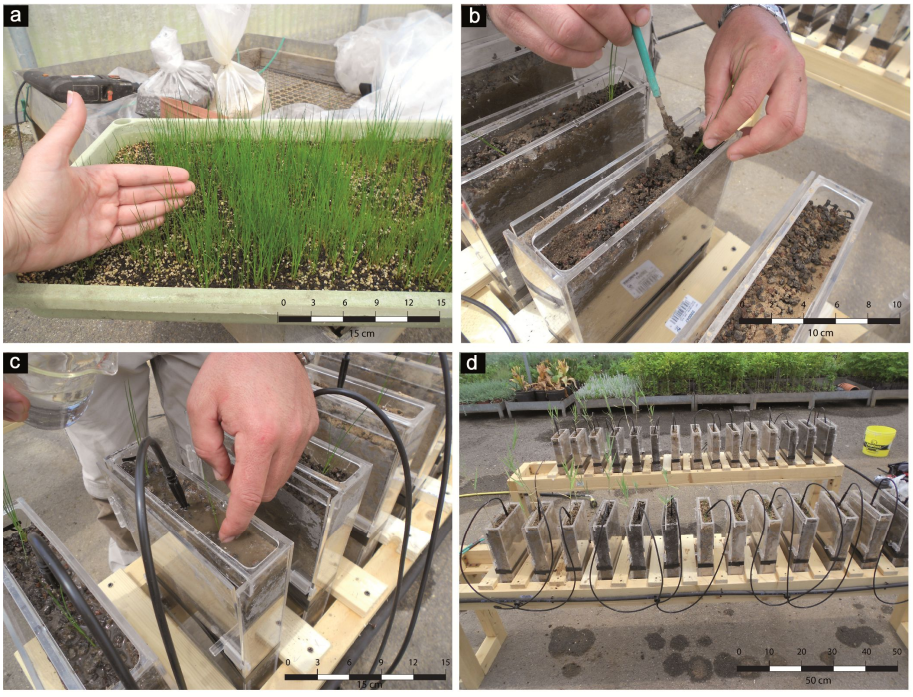

Figure 14.Plantlet of Juncus acutus (a)grown before rhizobox experiment: transplantation into the rhizobox (b) and (c), all the rhizoboxes were ready(still uncovered by dark fabric -d)

Two lines of irrigation were used, a first with polluted water (180 ppm of Zn-line A), the second with unpolluted water (50ppb of Zn-line B).Table 3 illustrates the set up of the rhizobox system, in each group there were five different combinations plan-substrate, for each combination there were three replicates.

The study began on May 2015 and ended on September 2015. In this period three parameters were isolated and studied: plants size, water quality and mineralogy and Zn content of substrates

Table 3. Scheme of rhizobox experiment, thirty rhizobox with different combination plant-substrate watered with water spiked (Line A) or unpolluted water (Line B)

	LineA[a]			LineB[b]	
	Substrate	***Plant***		***Substrate***	***Plant***
A1T	Unpolluted	*Juncus a.*	**B1T**	Unpolluted	*Juncus a.*
A2T	Unpolluted	*Juncus a.*	**B2T**	Unpolluted	*Juncus a.*
A3T	Unpolluted	*Juncus a.*	**B3T**	Unpolluted	*Juncus a.*
A4SM	Sa Masa	*Juncus a.*	**B4SM**	Sa Masa	*Juncus a.*
A5SM	Sa Masa	*Juncus a.*	**B5SM**	Sa Masa	*Juncus a.*
A6SM	Sa Masa	*Juncus a.*	**B6SM**	Sa Masa	*Juncus a.*
A7N	Naracauli	*Juncus a.*	**B7N**	Naracauli	*Juncus a.*
A8N	Naracauli	*Juncus a.*	**B8N**	Naracauli	*Juncus a.*
A9N	Naracauli	*Juncus a.*	**B9N**	Naracauli	*Juncus a.*
A10T	Unpolluted	*Phragmites a.*	**B10T**	Unpolluted	*Phragmites a.*
A11T	Unpolluted	*Phragmites a.*	**B11T**	Unpolluted	*Phragmites a.*
A12T	Unpolluted	*Phragmites a.*	**B12T**	Unpolluted	*Phragmites a.*
A13SM	Sa Masa	*Phragmites a.*	**B13SM**	Sa Masa	*Phragmites a.*
A14SM	Sa Masa	*Phragmites a.*	**B14SM**	Sa Masa	*Phragmites a.*
A15SM	Sa Masa	*Phragmites a.*	**B15SM**	Sa Masa	*Phragmites a.*

[a] water spiked with Zn, [b]water unpolluted

3.5 Zn isotope fractionation

Samples of *Juncus acutus* grown in Naracauli substrate, watered with polluted water, were selected to perform Zn isotope analyses. Zinc separation was performed using a single anion exchange resin column with hydrochloric acid media according to Borrok et al., 2007 and modified by Pribil et al. 2010. Samples of plants, substrates and water were manipulated in an ultra clean laboratory equipped with laminar flow hood. All materials used in the laboratory manipulation processes were washed in hot 10% HCl and rinsed whit MilliQ water (Fig. 15). Columns were prepared using Samco pipets (Cat #234, 14.4 cm×6.1 mm) with the narrow tips cut off and fitted with Bel-Art

porous frits (0.70 µm pore size). Pre-cleaned anion exchange resin (100–200 mesh AG MP- 1) was used to fill columns with a bed height of 5 cm. The loaded columns were rinsed using 5 mL of MilliQ water and conditioned using 4 mL of 10 M HCl. All samples were prepared to yield an adequate volume (5–10 mL) of solution with a final Zn concentration of 2,000 µg/L. The evaporation was done in a fume hood using a covered hotplate. The dried samples were reconstituted with 1 mL of 10 M HCl and loaded onto the ion exchange columns. Four 1 mL aliquots of 10 M HCl were added tothe column to elute most matrix cations and anions, allowing adequate time for each aliquot to elute from the column. Typically, eight 1 mL aliquots of 5 M HCl were used to completely elute the Cu fraction. Fe was eluted using four 1 mL aliquots of 1 MHCl, and Zn waseluted using four aliquots of 1 ml MilliQ water (Borrok et al., 2007).Spiked standard solutions and natural samples were placed in Savillex containers and evaporated to dryness.

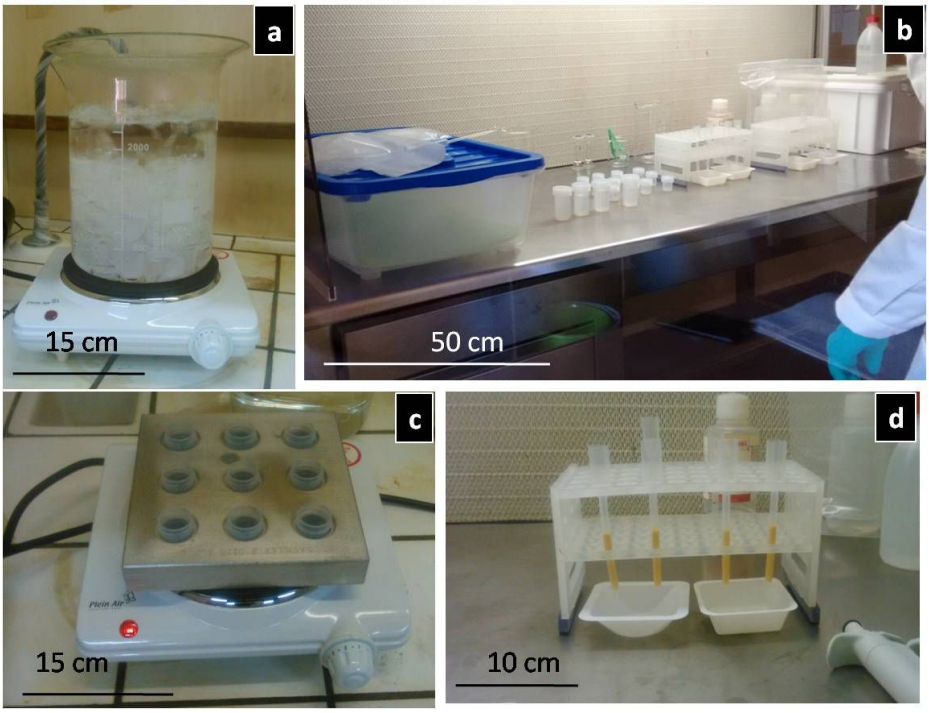

Figure 15. Preparation of samples to performed isotopic analysis: all material were washed in hot HCl (a),then all sample were prepared in a cleaned laboratory (b) samples were evaporated in hotplate (c) after being processes used set of column under laminar flow hood environment (d),

All isotopic analyses were carried out with the high resolution Nu Instruments double focusing MC-ICP-MS spectrometer in the USGS laboratory of Denver, Colorado. Liquid samples were fed to the MCICP- MS torch by using a desolvating nebulizer (DSN 100).

Double Standard-sample-standard bracketing (SSB) was used to correct for instrument drift and mass bias, using Zn-isotope standards that had been passed through the same column separation method as the samples (Wanty et al. 2013). Each individual analysis was performed as a block of 30 10-second measurements. Multireplicate separations and analyses, as well as reagent-column blanks, were used as checks on the quality of the data. Zinc isotope ratios are reported as ratios of $^{66}Zn/^{64}Zn$ using the standard δ notation.

Chapter 4- Natural processes in San Giorgio river

The Rio San Giorgio riverbed is characterized by widespread occurrence of vegetation. Plant species predominating at Rio San Giorgio are *Phragmites australis* and *Juncus acutus.* Here vegetation affects the riverbed section morphology, water velocity and, thus, erosional processes. An hydrological tracer approach was chosen to investigate the water discharge and the evolution of the metal load through the river section. The tracer data were processed to have a greater knowledge on the catchment and the hyporehic zone in the Rio San Giorgio.

4.1 Water chemistry of samples of the San Giorgio tracer

Table 4 reports distance (m), pH, Eh (V), conductivity (mS/cm), and major and trace chemical components in filtered water samples of the Rio San Giorgio (Tab. 4 and 5) and inflows (Tab.6 and7), respectively. Inflows to Rio San Giorgio were divided into right bank (R) and left bank (L) inflows. Along Rio San Giorgio, pH ranged from 7.7 to 8.3 and tends to increase downstream, likely reflecting dissolution of carbonate minerals occurring in the catchment and in the ores (calcite, dolomite, ankerite, cerussite, smithsonite, hydrozincite, etc.). Redox potential (between 0.48 and 0.56 V) indicated oxidizing conditions. Conductivity of collected waters, stream and tributaries varied significantly (0.59 mS/cm to 8.89 mS/cm). The inflow from the Fanghi Rossi had the highest value (8.89 mS/cm). Accordingly, conductivity values along the Rio San Giorgio ranged from 1.57 to 1.98 mS/cm, and showed an increase from 1.69 mS/cm to 1.98 mS/cm immediately downstream from the inflow from the Fanghi Rossi mine wastes.

Table 4. Distance (m), pH, redox potential (Eh), conductivity (Cond) and major chemical components in filtered samples collected along the Rio San Giorgio.

Site	Dist M	pH	Eh V	Cond mS/cm	Ca mg/l	Mg mg/l	Na mg/l	K mg/l	HCO_3^- mg/l	Cl mg/l	SO_4^{2-} mg/l	Zn µg/l
1	0	7.7	0.49	1.58	134	60	91	10.5	510	120	230	49
2	283	7.7	0.5	1.62	136	61	93	10.3	490	110	250	55
3	610	8.1	0.48	1.57	137	62	94	10.2	470	110	270	53
4	931	7.7	0.5	1.6	158	66	88	6.7	370	120	360	130
5	1234	8.1	0.48	1.63	166	68	92	7	390	110	380	230
7	1558	7.9	0.52	1.63	159	67	93	5.2	380	130	380	230
8	1650	7.8	0.45	1.7	178	68	92	5.2	380	120	450	590
9	1840	7.9	0.53	1.66	167	67	91	5.3	390	130	430	380
10	1941	8	0.55	1.69	169	67	95	4.5	390	134	440	360
11	2312	7.7	0.56	1.98	189	98	96	7.9	350	140	620	2500
12	3024	8	0.55	1.9	176	89	110	9.2	340	150	570	1400
13	3686	8.3	0.53	1.88	179	90	110	8.9	350	160	570	1300
14	4000	8.2	0.5	1.86	175	87	110	9	350	160	560	1400
15	4317	8.2	0.52	1.81	172	84	110	9.7	340	160	540	1700
16	4492	8.3	0.53	1.66	170	85	110	10	350	160	510	1600
17	4656	8.1	0.55	1.83	161	79	97	8.8	340	160	500	1600
18	5357	8.2	0.53	1.84	163	81	110	9.5	330	160	530	1600
19	5577	8.2	0.51	1.82	164	82	100	8.8	340	160	570	1500

Table 5. Trace chemical components in filtered samples collected along the Rio San Giorgio. DL indicates Detection Limit.

Site	Mn µg/l	Cd	Pb	Sr	Mo	Co	Ni	Cu	Ba	U	Sb	Fe	B	Al
1	1100	0.03	1.6	200	0.22	0.96	1.7	0.8	53	0.38	0.17	47	110	5
2	1120	0.04	1.8	200	0.22	0.92	1.8	< DL	55	0.4	0.16	30	110	6
3	1070	0.04	1.6	210	0.21	0.87	1.9	1	53	0.4	0.16	27	110	5
4	57	0.1	0.63	280	0.55	0.5	1.8	2.1	22	0.44	0.21	<DL	110	6
5	7.7	0.2	0.91	290	0.78	0.4	1.7	2.4	27	0.46	0.31	<DL	100	2
6	70	0.1	0.62	290	0.83	0.46	1.9	2.2	29	0.48	0.33	<DL	110	3
7	53	0.1	0.69	280	0.87	0.41	1.8	2.2	29	0.49	0.32	<DL	110	<DL
8	13	0.46	1.9	310	0.78	0.47	2.2	3.3	30	0.47	0.34	<DL	130	<DL
9	16	0.27	1.4	300	0.88	0.46	2	3.5	32	0.46	0.33	<DL	110	4
10	32	0.23	4.6	300	0.84	0.4	2	2.4	32	0.47	0.35	<DL	110	3
11	270	31	3.6	330	0.76	0.86	2.6	2.4	31	0.41	0.27	<DL	130	<DL
12	260	6.5	2.9	310	0.72	0.72	2.3	2	36	0.49	0.31	<DL	120	3
13	280	5.1	3.2	310	0.72	0.77	2.6	2.4	36	0.51	0.32	<DL	120	4
14	260	8	12	310	0.8	0.79	2.5	3.1	35	0.54	0.41	<DL	120	<DL
15	200	13	16	300	0.81	0.7	2.1	3.1	33	0.59	0.47	<DL	130	<DL
16	190	11	16	300	0.83	0.7	2.5	5.8	33	0.56	0.51	<DL	130	6
17	200	12	15	300	0.85	0.76	2.2	3.6	32	0.6	0.48	<DL	140	5
18	200	13	14	300	0.85	0.69	2.4	3.7	33	0.63	0.5	<DL	140	2
19	190	9.6	12	310	0.89	0.67	2.2	3.2	34	0.61	0.53	<DL	120	<DL

DL_{Cu} = 1 µg/l; DL_{Fe} = 20 µg/l; DL_{Al} = 2 µg/l

Table 6. Distance (m), pH, redox potential (Eh), conductivity (Cond) and major chemical components in filtered samples collected in tributaries

Site	Dist	pH	Eh	Cond	Ca	Mg	Na	K	HCO_3^-	Cl	SO_4^{2-}	Zn
	M		V	mS/cm	mg/l	mg/l	mg/l	mg/l	mg/l	mg/l	mg/l	µg/l
L1	680	7.7	0.49	2.18	400	115	105	12	140	1290	24	1300
L2	900	7.1	0.50	0.59	74	42	86	5.7	150	43	387	410
L3	1390	7.9	0.54	2.81	372	149	290	18.8	430	1380	350	8100
R1	1580	7.0	0.55	3.15	550	133	170	17	230	1900	302	17000
R2	2099	7.7	0.47	2.39	273	234	67	29	100	1600	180	19000
R3	2100	7.6	0.49	2.28	275	228	71	30	100	1500	155	12000
R4	2100	7.2	0.52	8.89	433	1130	68	38	90	7100	52	470000
R5	2350	8.6	0.47	0.85	106	76	68	10	96	320	347	310
L4	3650	7.2	0.53	1.01	78	69	190	6.3	460	98	219	9

Table 7. Trace chemical components in filtered samples collected on tributaries. DL indicates Detection Limit.

Site	Mn	Cd	Pb	Sr	Mo	Co	Ni	Cu	Ba	U	Sb	Fe	B	Al
	µg/l													
L1	570	0.10	0.25	1100	1.3	0.95	3.3	2.1	20	0.63	0.08	< DL	84	<DL
L2	80	3.5	3.6	170	< DL	0.14	1.0	1.3	140	1.0	0.33	< DL	62	3
L3	29	8.0	9.4	720	1.1	0.42	7.7	2.2	10	1.46	0.20	< DL	240	<DL
R1	1600	24	51	690	< DL	14	7.2	3.2	11	0.61	0.14	< DL	180	<DL
R2	560	230	19	450	0.60	1.7	9.2	1.0	16	0.23	0.38	< DL	200	<DL
R3	480	200	57	420	0.40	1.5	5.2	1.6	24	0.16	0.17	< DL	130	<DL
R4	8200	2200	340	650	< DL	44	120	2.5	16	< DL	0.05	< DL	85	2
R5	6.6	2.8	7	210	0.59	0.15	0.72	1.7	44	1.9	0.19	< DL	74	<DL
L4	0.4	0.11	0.88	380	< DL	0.10	< DL	< DL	89	0.25	< DL	< DL	94	2

DL_{Mo} = 0.15 µg/l;DL_{Ni} = 0.6 µg/l; DL_{Cu} = 0.8 µg/l; DL_{U} = 0.05 µg/l;DL_{Sb} = 0.15 µg/l;DL_{Fe} = 20 µg/l; DL_{Al} = 2 µg/l

A Piper diagram was used to classify waters from Rio San Giorgio and the inflows (Fig. 16). Rio San Giorgio waters can be divided into 3 groups, which mostly differ in the concentrations of SO_4^{2-} and HCO_3^-, and have Ca and Mg as predominant cations. The groups include reach 1 from point 01 to point 03 (blue squares) showing a dominant Ca-Mg-bicarbonate composition, reach 2 from point 04 to point 10 (pink squares) characterized by a Ca-Mg-sulphate (bicarbonate) composition, and reach 3 from point 11 to point 19 (green squares) showing a dominant Ca-Mg-sulphate composition. Observed variation, from upstream to downstream, are due to inflow waters from

tailings dumps located on both sides of the Rio San Giorgio. Except for samples L2 and L4, tributaries have a predominant Mg and/or Ca sulphate composition.

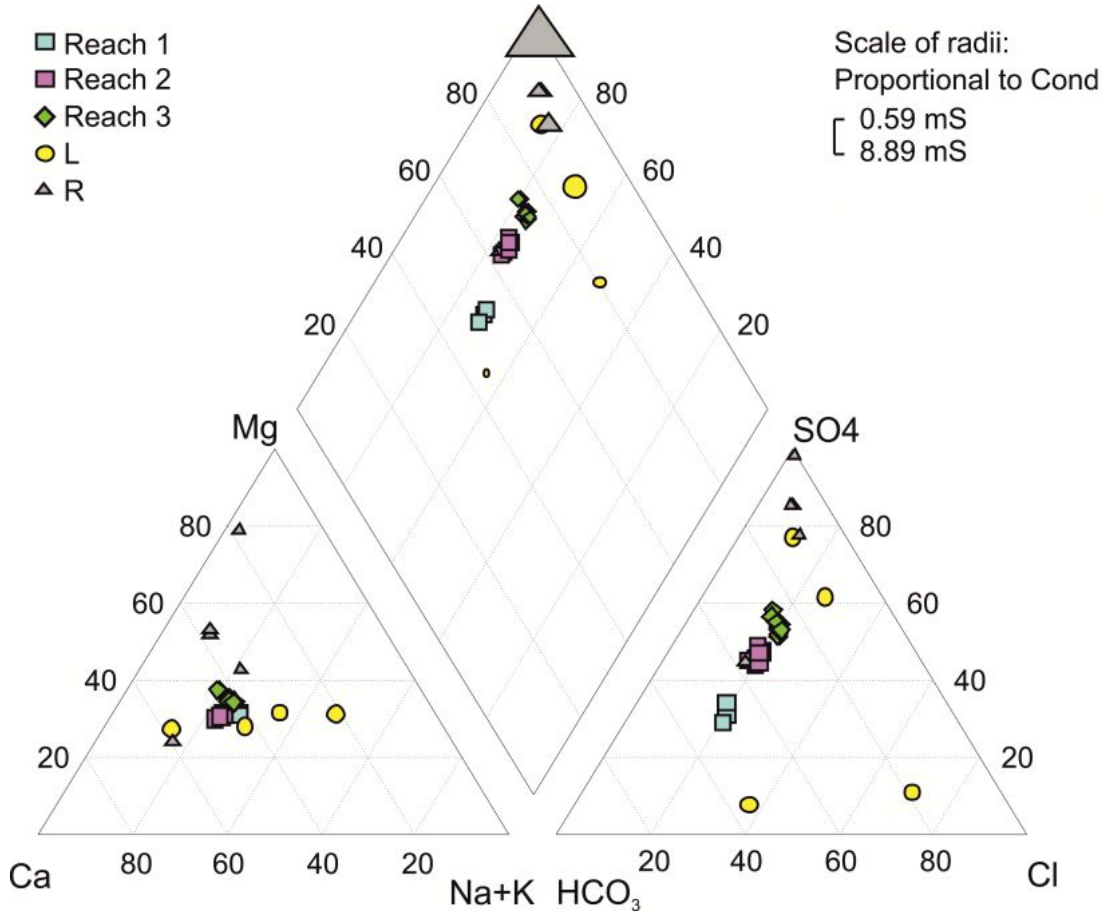

Figure 16. Piper diagram of San Giorgio river waters (reach 1: from 0 m to 931 m, reach 2: from 931 to 2312; reach 3: 2312 m to 5577 m) and tributaries (L and R).

Zn, Cd, Pb, Ni and Cu concentrations in Rio San Giorgio waters and tributaries are shown in Table 4, 5, 6 and 7. These metals tend to increase from upstream to downstream along Rio San Giorgio, mainly because of the drainages from mine tailings. Despite studies indicating generally extreme values of Zn concentrations for other streams affected by mine drainage in Sardinia (Cidu and Fanfani, 2002; Cidu et al., 2011; Frau et al., 2015), concentrations of Zn and other harmful metals in Rio San Giorgio show values either below or above the freshwater pollution thresholds (as defined by Italian Decree 152/2006: Zn 500 µg/l, Pb 200 µg/l, Cd 20 µg/l, Ni 2000 µg/l, Cu 100

µg/l and SO_4 1000 mg/kg). In fact, Zn concentration values range from 49 µg/l to 2500 µg/l, Pb ranges from 0.63 µg/l to 16 µg/l, Cd ranges from 0.03 µg/l to 31 µg/l, Cu ranges from < DL to 5.8 µg/l, Ni ranges from 1.7 µg/l to 2.6 µg/l and SO_4 ranges from 230 to 620 mg/l. Pb concentrations ranging from 1.1 µg/l to 53 µg/l in Rio San Giorgio waters.

Mn and Co, in filtered samples, show the highest concentrations from station 1 to station 3 (Mn 1070-1120 µg/l, Co 0.87-0.96 µg/l), then decrease showing the lowest concentration at station 5 (Mn 7.7 µg/l, Co 0.4 µg/l), and increase between station 10 (Mn 32 µg/l, Co 0.4 µg/l) and 11 (Mn 270 µg/l, Co 0.86 µg/l). Further downstream, Mn and Co do not show significant variation. Fe values are above the detection limit (DL_{Fe} 20 µg/l) at stations 1 to 3, showing concentrations between 27 and 47 µg/l.

4.2 Diel variation in Zn concentrations

A 48-hour diel sampling at the 5 Transport sites was carried out before the synoptic experiment, from 31 May to 2 June 2012. The upstream site was at site 03, and the downstream site was between sites R5 and 12. The concentration of Zn varied throughout the 2-day period (Fig. 17), likely due to Zn adsorption to streambed Fe solids. This fluctuation of Zn is in phase opposition respect a fluctuation of the Fe oxides observed by Nimick et al., 2003; Gammons et al., 2005 that changes with diel variation in temperature, pH, biological activity, and other properties. The data on Zn diel variation give the opportunity to make adjustments to the longitudinal Zn profile from the synoptic sampling and thus, the loading calculations of Zn (De Giudici et al., 2014). Because Zn concentrations vary sinusoidally in a 24-hour period, the ideal synoptic sample design would be for a simultaneous collection of samples from each site at the peak or trough of the daily Zn variation,

where Zn is less variable over short time spans. The most intense diel variation was observed at station T4, where the night (04:00) Zn concentration is about double that which was measured at 17:00. For the other Transport sites this effect is smaller, but not negligible. The synoptic sampling was conducted during a period when the Zn concentration was decreasing with time. As sampling proceeded from downstream to upstream sites during the morning, actual measured Zn concentrations were progressively lower at each site than they would have been had they been sampled concurrently with the downstream site, i.e., a true synoptic sampling. For the temporally long tracer of Rio San Giorgio, it was preferred to avoid diel correction for Zn. Plotting Zn concentration from the two synoptic samplings (Syn. 9 AM and Syn. 5 PM) indicates that the shape of the Zn profile is not affected by diel variation, but the differences in magnitude are particularly marked after the Fanghi Rossi inflow.

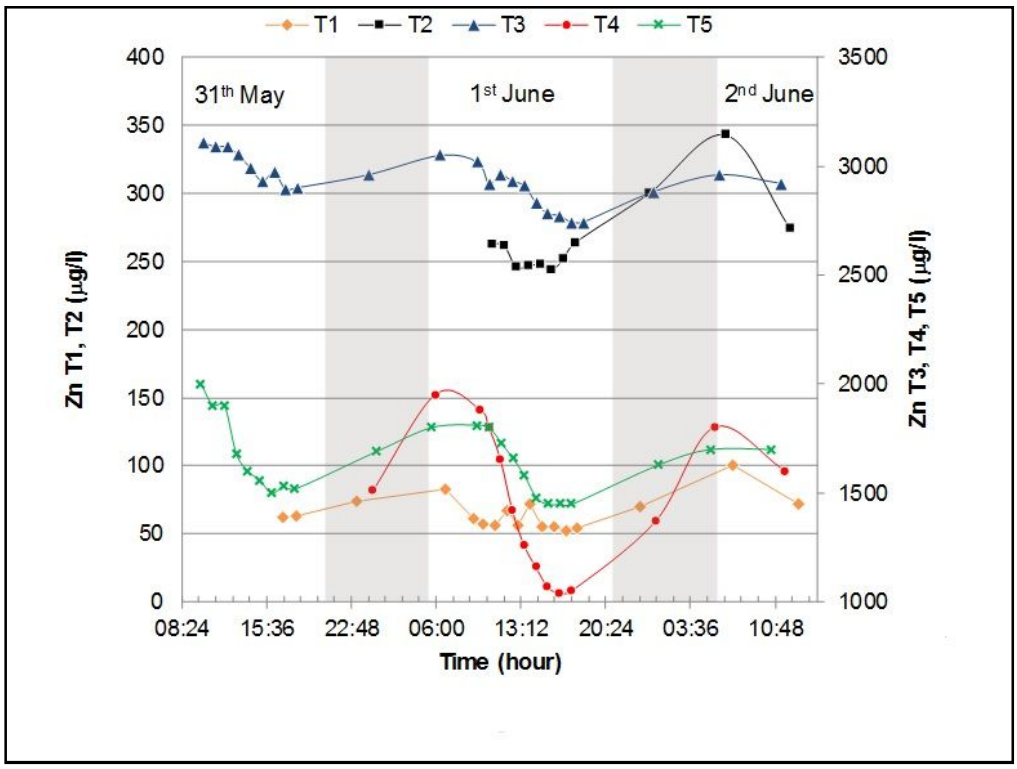

Figure 17. Diel variation for Zn in filtered samples at T sites. Note that T1 and T2 (above input from Fanghi Rossi) are plotted on different axes than T3, T4, and T5.

4.3 Discharge

A Br solution of 183,200 mg/L (RSD 0.61%) was injected at a rate of 30.2 mL/min (RSD 1.84%) for 90 hours before the synoptic sampling and an additional 9 hours during the sampling. The Br background concentration measured upstream before the injection was 0.5 mg/l, while at the first site downstream after the injection the Br concentration reached 5.8 mg/l, and then decreased downstream, due to dilution from inflows. At the end of the study reach, the concentration was about 1.0 mg/l (Fig. 18).

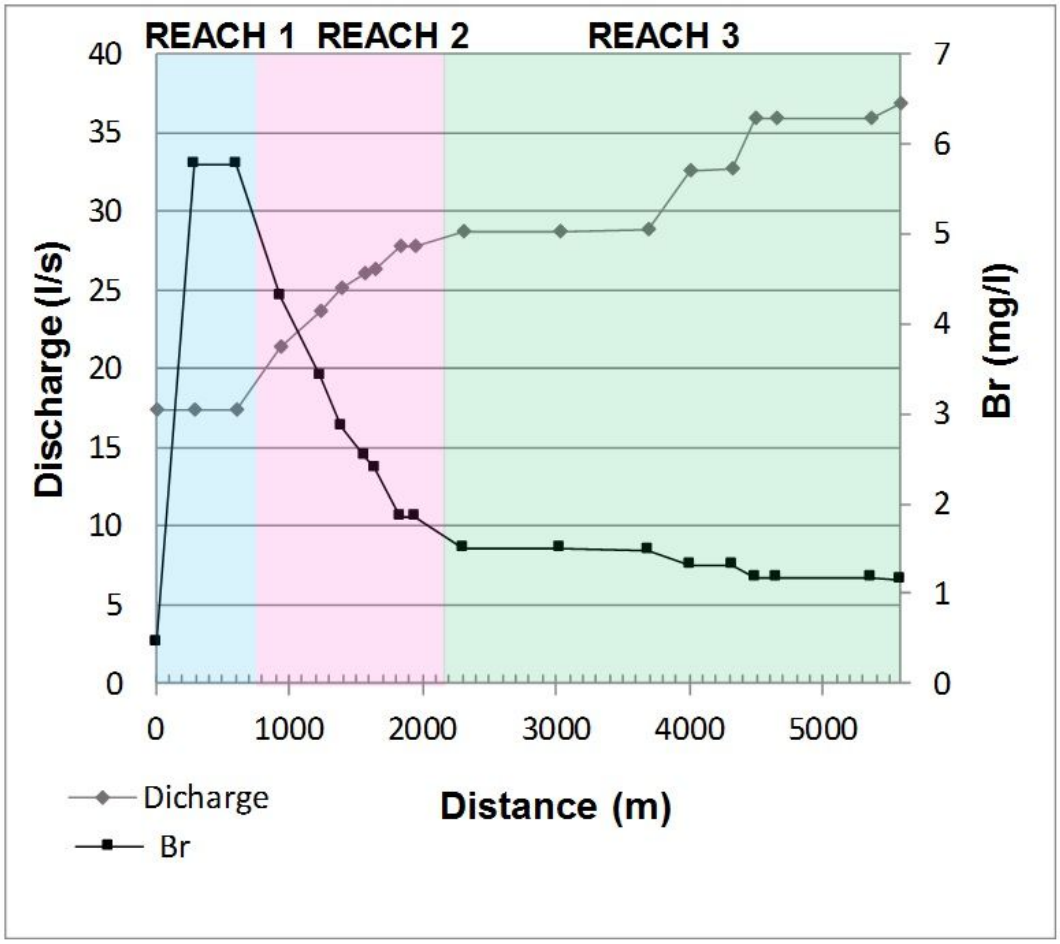

Figure 18. Diagram of discharge (l/s) and Br concentration (mg/l) vs distance (m) along the Rio San Giorgio (reach 1, from 0 m to 931 m; reach 2, from 931 m to 2312 m; reach 3, from 2312 m to 5577).

Discharge values for every sample site were calculated applying an equation for Br mass balance downstream from the injection site (Kimball et al., 2002). According to the recent literature, these values can be affected by "double counted discharge" (Bencala et al., 2011). Mass balance, which allows the calculation of a tracer-dilution discharge, assumes that all the Br that enters hyporheic flow paths is balanced by an equal mass of Br exiting the same hyporheic flow paths. However, depending on the porosity, grain size distribution, and length of the flow path, it is possible that this mass balance might not be attained in the time frame of the experimental injection. If this is true, then those particular flow paths would be discharging water, free of the injected Br, that would contain Br if the time frame of the experiment had been longer to reach that equilibrium for Br. Thus, by tracer dilution, there appears to be a new inflow, and an increase in discharge, when that is not really the case. To check for this possibility, "slug injections" can be carried out to compare that instantaneous discharge measurement of water in the stream channel to that calculated by tracer dilution. Slug injections were conducted at three sites along the study reach, at site 2 (283 m), site 13 (3686 m) and site 18 (5357 m). In addition to these three points, we can use the discharge calculated at the first stream sampling site downstream from the Br injection because the "double counting" effect is assumed to be minimal or to not exist at that short distance along the study reach. At the most downstream site, 18, the slug discharge was 36.7 l/s, which was more visually consistent with the amount of water in the stream channel, rather than the four-fold higher value calculated from Br dilution at that point. Thus, it was assumed that the "double-counting" effect was significant, most likely due to the amount of sandy substrate that could increase travel time in the hyporheic zone.

Based on the discharge values from the three slug injections and the initial discharge downstream from the continuous Br injection point, the discharge profile of Rio San Giorgio was "lowered," by pro-rating based on the distance of the site between each set of these 4 points. From site to site the

relative change in discharge was still calculated from the Br dilution between the two points, but was constrained by the discharge values calculated from the slug injections. This does not indicate an error in the method, but a recalibration of discharge based on independent secondary measurements.

Figure 18 illustrates the downstream increase of discharge from 17.4 l/s to 36.7 l/s. After a constant discharge at the first three points of reach 1, a continuous increase occurred from the fourth to tenth point in reach 2. Then, in reach 3, discharge increased to a plateau in the last few points. Figure 19 also shows the Zn load versus distance observed for the two sets of synoptic samples collected on 4 June 2012.

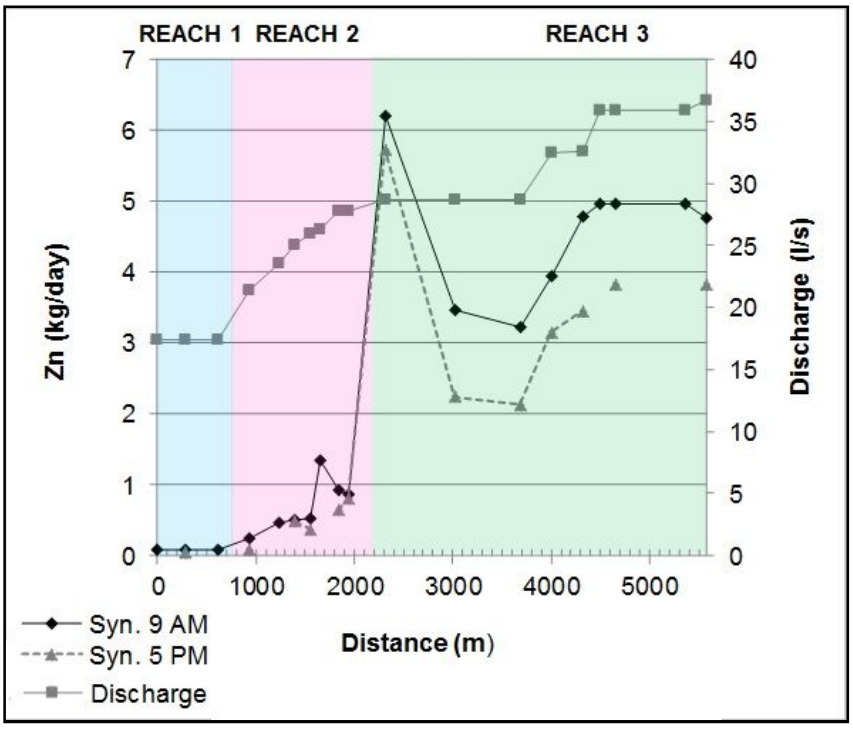

Figure 19. Difference in Zn load (kg/day) along the Rio San Giorgio observed for the two samplings on 4 June 2012 and discharge (l/s). Reach 1, from 0 m to 931 m; reach 2, from 931 m to 2312 m; reach 3, from 2312 m to 5577 m.

Zn concentration of inflow points is shown in Fig. 21. The general trend of Zn load showed a constant value in reach 1, a small increase in reach 2, and then had a marked increase in reach 3. The diel effect on the Zn load leads to somewhat different peaks. For the "true" synoptic at 17:00

(Syn. 5 PM) the maximum peak had a value of 5.7 kg/day and then decreased to 2.2 kg/day; for the synoptic made at 9:00 (Syn. 9 AM) the maximum peak had a value 6.2 kg/day and then decreased to 3.48 kg/day. The loads of Cd, Pb and SO_4^{2-} are shown in Fig. 20 a-b. Cd, Pb and SO_4^{2-} concentrations of inflow points are shown in Fig. 21 and c. The load of Cd (Fig. 20 b) is highly correlated to Zn (r= 0.92) load throughout the entire study reach of Rio San Giorgio. The load of Pb (Fig. 20b), even if generally correlated to Zn load (r= 0.66), does not show the same peak at the beginning of reach 3. Only for Pb, the difference in concentration shows an increase from filtered to unfiltered samples ranging from a factor of 2 to 3. The load of SO_4^{2-} (Fig. 20a) gradually increased from 245 to 1810 kg/d, and also did not show a marked peak at the beginning of reach 3.

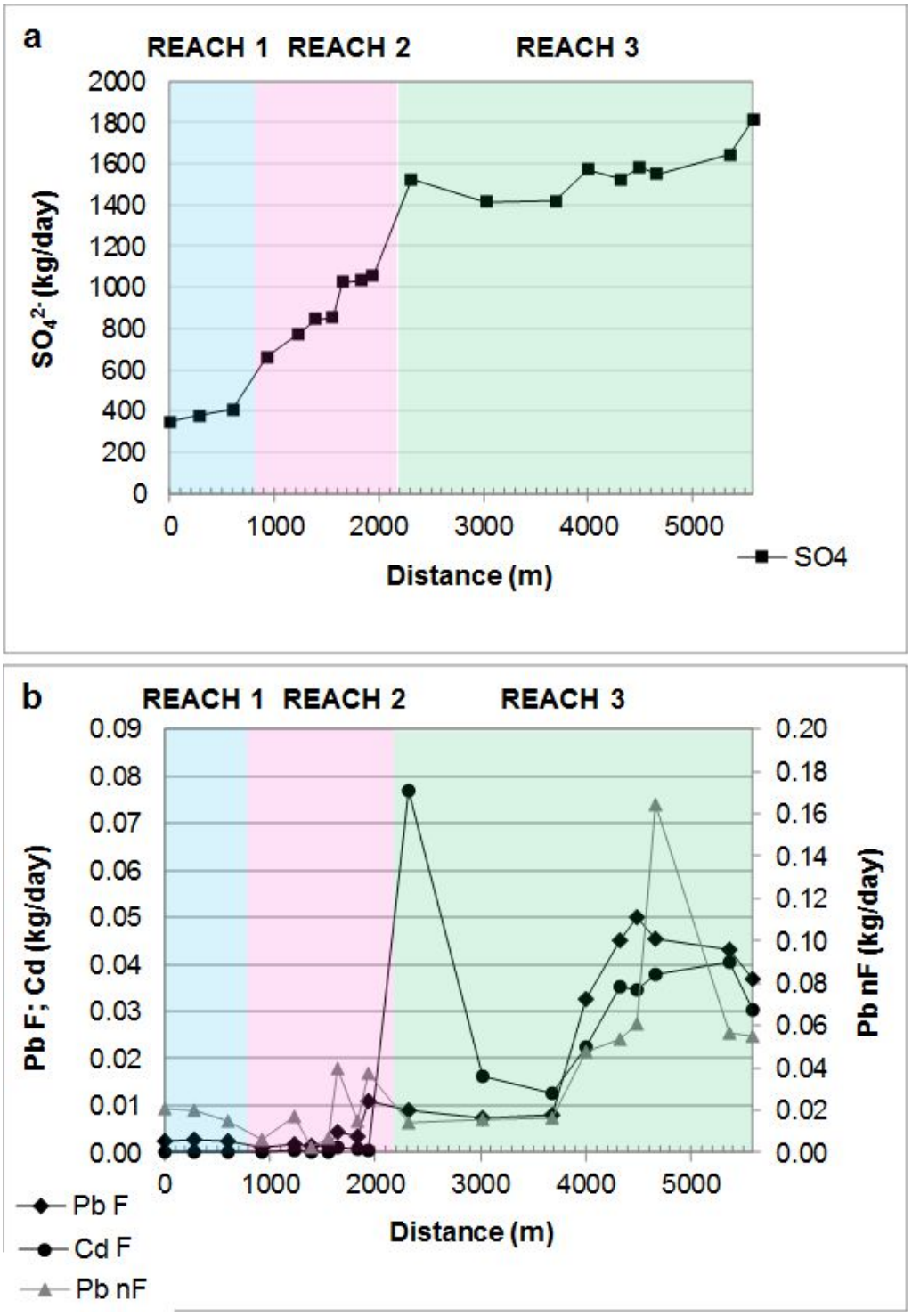

Figure 20. Diagrams of SO_4^{2-} (a) Cd and Pb (b) loads (kg/day) in filtered samples (reach 1, from 0 m to 931 m; reach 2, from 931 m to 2312 m; reach 3, from 2312 m to 5577 m). Pb load is reported both for filtered (F) and unfiltered samples (nF).

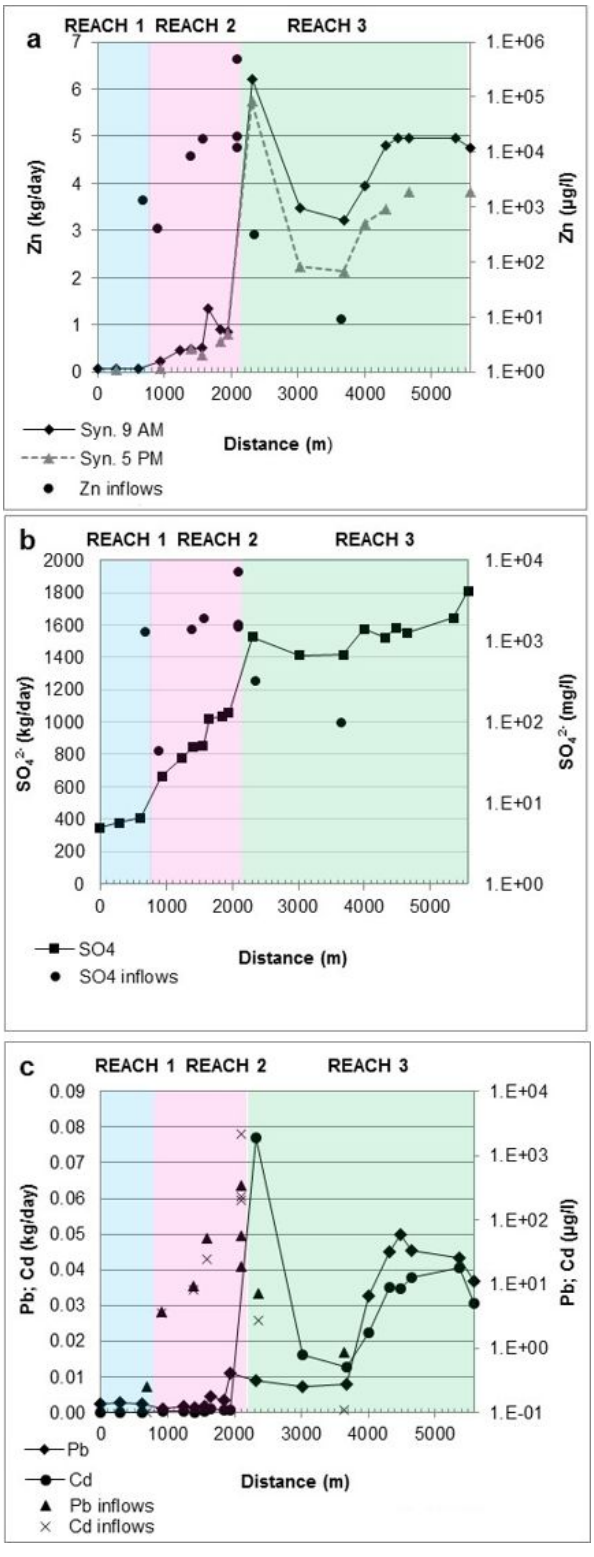

Figure 21. Diagrams of Zn (a), SO_4^{2-} (b), Cd and Pb (c) loads (kg/day) in filtered samples (reach 1, from 0 m to 931 m; reach 2, from 931 m to 2312 m; reach 3, from 2312 m to 5577 m). Also, Zn (a), SO_4^{2-} (b), Cd and Pb (c) concentrations of inflows are reported

4.4 Core sampling in San Giorgio area

Unconsolidated sequences of reddish sand and grey silts and clays occurred irregularly in the four sediment cores, location of these core was shown in figure 7. Primary mineralogy (Fig. 22) consisted of minerals commonly found in the ores (sphalerite, galena, pyrite, goethite, hemimorphite, cerussite), and did not change among the four cores.

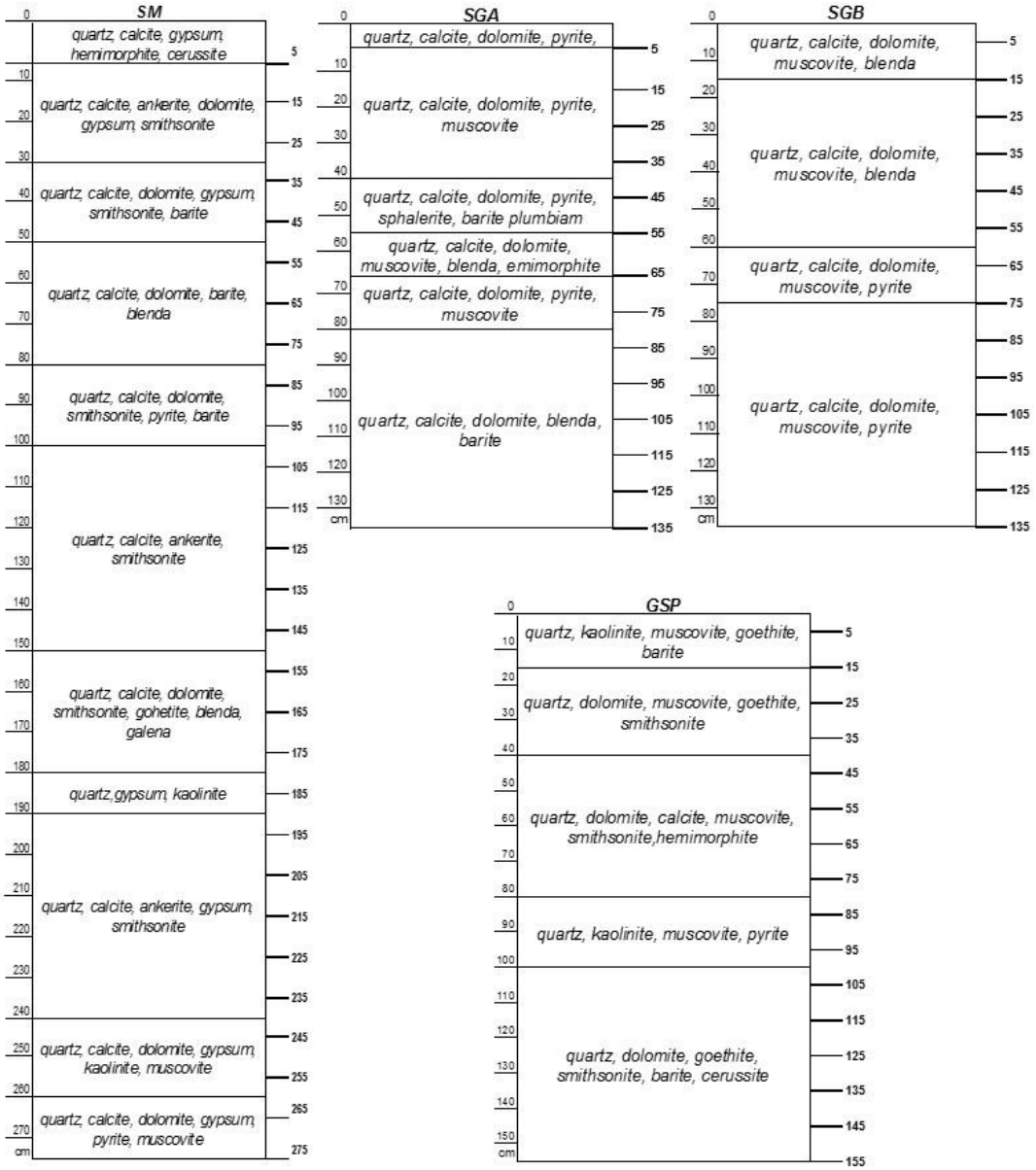

Figure 22. Mineralogical Stratigraphy of core samples: SM and GSP.

Pyrite, detected by XRD, was present as a newly formed mineral (Fig. 23). In fact, framboidal pyrite, made of individuals having octahedral habit, was found to be abundant in the sediments (Fig. 23 a-e). These micrometric framboids likely resulted from the process of microbial sulphate reduction and consequent formation of secondary pyrite, indicating that their formation is due to supergene processes driven by biogeochemical processes.

Fragments of plant roots were abundant in all the cores. SEM imaging with EDS microanalysis (Fig. 23, 24) allowed recognition of micrometric framboids of pyrite occurring also at the root surface of both *Phragmites australis* and *Juncus acutus*, at a depth from 60 to 200 cm. In detail, Fig. 23b shows the surface of a root of *Phragmites australis* with a framboid of microbial iron sulphide of about 40-µm diameter at depth of 180 cm.

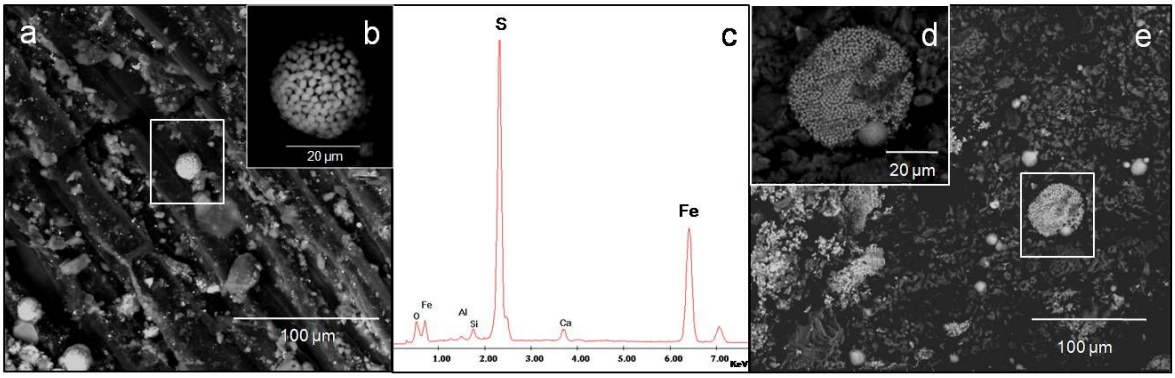

Figure 23. SEM image of framboidal iron sulphide (a-b and d-e) on root of Phragmites australis with EDS microanalysis (c), core SM.

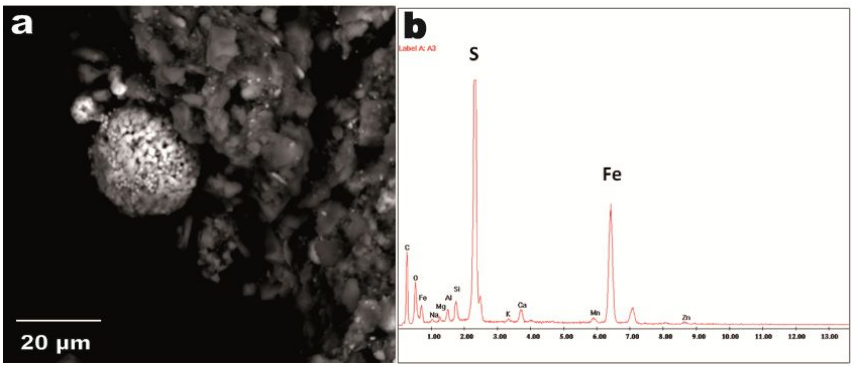

Figure 24. SEM image of framboidal pyrite on surfaces of Juncus acutus roots (a). EDS analysis (b), core GSP.

4.5 Scanning Transmission X-ray Microscopy and X ray absorption spectroscopy

Chemical analysis of *Phragmites australi,* performed by ICP-OES after acid digestion of the solid samples, indicates that the Zn concentration in the root epidermis shows a value of 830 mg/kg, in the inner part of the root the value is 530 mg/kg, while in stems and leaves the values are 130 and 70 mg/kg, respectively. Fe values in the root epidermis are 1,500 mg/kg, in the inner part of the root 670 mg/kg, while in stem and leaves the values are 450 and 430 mg/kg, respectively. This tiered decrease in Zn and Fe concentration is reflected in Scanning Transmission X-ray Microscopy (STXM) maps of thin slices of *Phragmites australis* root shown in Fig. 25. Light Elements X – Rays Fluorescence (LEXRF) maps of Fe, Zn, Si and Al were acquired in areas 1, 2 and 3 and are reported in Fig. 25b with the corresponding bright field (absorption) images. LEXRF analysis shows that Fe, Zn, Si and Al are mainly localized in the root epidermis.

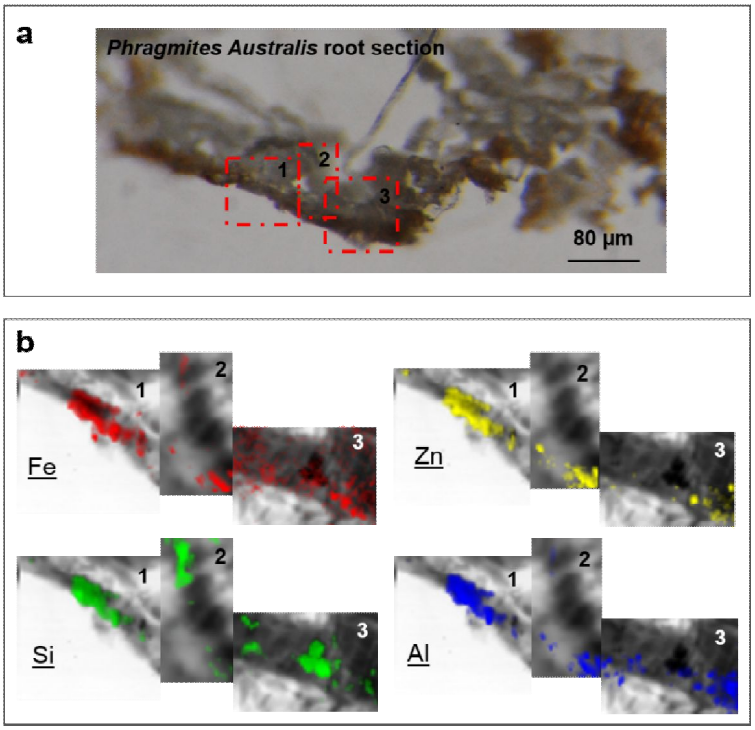

Figure 25.Selected sample of Phragmites australis. Ordinary light stereo-microscope image (a) and areas (1, 2, 3) for LEXRF mapping. Bright field (absorption) images and LEXRF maps of Fe, Zn, Si and Al (b).

X-ray absorption spectroscopy (XAS) provides detailed information about the average local coordination chemistry and valence state of the absorbing ions. The near edge (XANES) regions of the Fe K-edge XAS spectra (Fig. 26 a and b) measured on plant roots reveal a predominance of Fe^{3+} in an oxo- or hydroxyl coordination environment. The quantitative analysis of the Fe XAS features of roots of *Phragmites australis* has been carried out by fitting the area of the pre-edge peak (Fig. 26c). According to Wilke et al. (2001), the pre-edge centroid position is related to the average Fe valence state, and the area to the Fe-O coordination number. It was found the Fe pre-edge centroid at c_{pre} = 2.38(3) eV above the Fe^0 edge (7112 eV) and its area A_{pre} = 0.069(±0.002) eV, these values are in agreement with Fe^{3+} state 6 coordinated in FeO_6 octahedral configurations (Wilke et al., 2001).

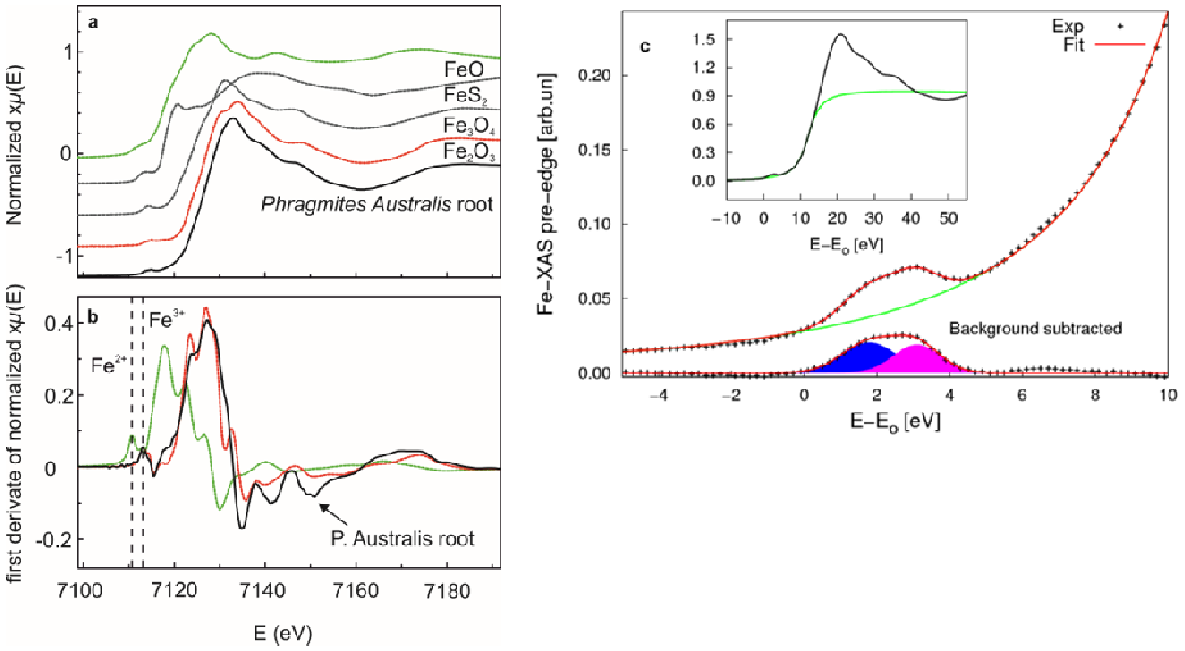

Figure 26. Fe K-edge XANES spectra for Phragmites australis root and reference compounds: a) normalized spectra, b) first derivate, c) pre-edge best fit of Phragmites australis roots. Pre-edge fit as achieved using an arctangent background (green curve) and two gaussian contributions (blue and violet).

Zn K-edge XAS analysis allowed us to focus on the Zn speciation in rhizosphere materials and in parts of *Phragmites australis*. Figure 25 shows normalized Zn K-edge absorption spectra in the near

edge (XANES) region of plant roots (external, that is epidermis, and inner part), stem, leaves, rhizosphere solid materials samples, and selected reference compounds. Considering the Zn XANES spectral features of the plant samples, in comparison with those of selected reference compounds (Fig. 27), rhizosphere solid materials and external root (cleaned and not cleaned) depict main spectral features similar to those of hydrozincite (Fig. 27, red solid lines); while stem and inner root depict main spectral features similar to those of Zn in hydroxyapatite (Fig. 27, green dashed line). Leaves samples show intermediate characteristics.

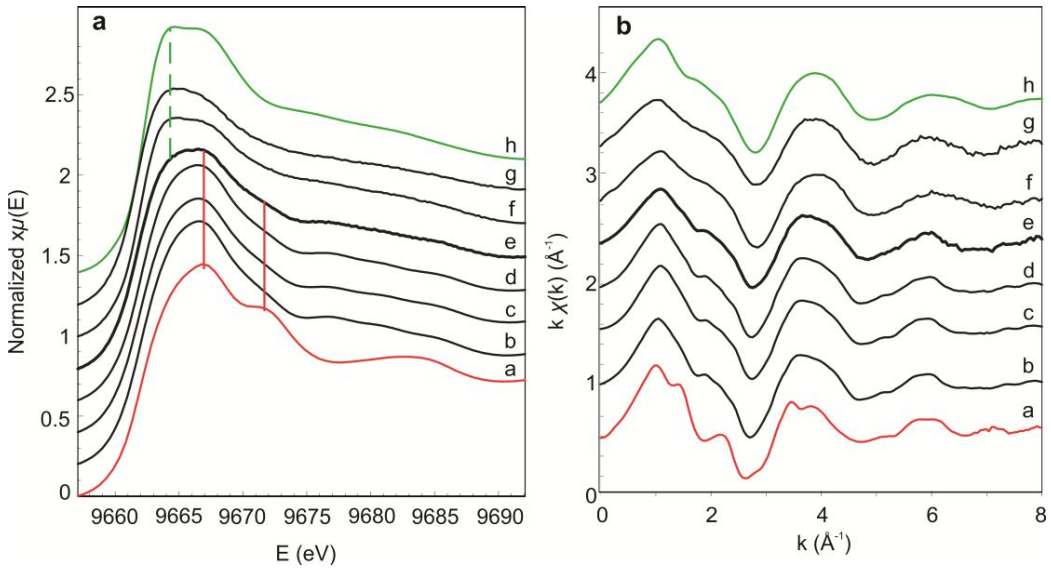

Figure 27. XANES spectra (a) and k χ(k) (b) at the Zn K-edge collected on selected reference compounds (a: hydrozincite; h: Zn hydroxyapatite), rhizosphere materials (b), external root not cleaned (c), external root cleaned (d), leaves (e), inner root (f), and stem (g) of Phragmites australis vertically shifted for the sake of clarity. Similar features among plant samples, rhizosphere materials and reference compounds are highlighted in the XANES region. The leaves sample depicts intermediate behaviour and is put in evidence with ticker line.

Linear combination analysis of XANES spectra was used to get information about Zn phase fractions in the samples. Reference spectra for the LCA were selected from a large dataset chemically compatible with our samples (see Table 2 and Fig. 25b), following a trial and error procedure, based on a statistical analysis of the best fit residue (χ^2-test and F-test), to identify the individual components giving the best agreement. The results are shown in Table 8. For group 1, it

was found that the main contribution was hydrozincite, then Zn-acetate-hydrate and smithsonite were found to provide a relevant contribution. Finally, we found that Zn in cysteine and Zn in hydroxyapatite significantly improved the quality of LCA fit for this group (Table 8). Zn is complexed with organic acids or amino acids including cysteine and sequestered in the root, making it less available for roots loading to the shoots (Zeng et al., 2005). For the stem, an additional contribution was provided by hydrozincite and smithsonite, the last did not significantly improve the fit for the inner root sample. Results of LCA for the leaves sample (thicker line in the Fig. 25) show intermediate characteristics between group 1 and 2, quantitatively supporting previous observations on the XANES spectral features (see Fig. 25). These results suggest that Zn is present in our samples in two main different coordination environments, related to both inorganic phase and organic compounds.

Table 8.Results and fit parameters of the best fits for rhizosphere materials, external root (not cleaned and cleaned), inner root, stem and leaves of Phragmites australis. The sum of contribute fractions is fixed to 100%, the incertitude on the fraction values is around 5-8%.

	Hydrozincite **%**	**Smithsonite** **%**	**Zn acetate hydrate %**	**Zn cysteine %**	**Zn hydroxyapatite %**	**R-factor x10^3**
Rhizosphere	42	15	20	13	12	0.17
External root not cleaned	43	14	16	20	7.6	0.16
External root cleaned	36	12	14	17	21	0.13
Leaves	36	10	4.9	30	19	0.25
Inner root	24	-	-	24	52	0.52
Stem	17	5.2	-	41	37	0.47

The results of EXAFS region data fitting are presented in in Table 9.

Table 9. Parameters for EXAFS analysis. EXAFS data analysis procedure is explained in the main text.

Shell	CN	R (Å)	$\sigma^2 x10^3$ (Å^2)	R^2
Zn in hydroxyapatite				0.009
ZnO	4*	1.93(1)	10.9(4)	
ZnP	1.9(1)	2.56(1)	22(5)	
ZnP	3.9(2)	2.82(1)	28(4)	
Rizosphere				0.05
ZnO	4.3(2)	2.01(1)	8.9(5)	
External root not cleaned				0.05
ZnO	4.4(2)	2.02(1)	9.1(6)	
External root cleaned				0.05
ZnO	4.2(2)	2.02(1)	9.6(4)	
Leaves				0.05
ZnO	4.3(2)	2.01(1)	8.9(7)	
Inner root				0.03
ZnO	4.3(2)	1.92(1)	10(1)	
ZnP	1.4(1)	2.64(1)	8.8(6)	
ZnP	2.1(1)	2.88(1)	12(3)	
Stem				0.03
ZnO	4.8(2)	1.97(1)	11(1)	
ZnP	1.5(1)	2.67(1)	1.9(3)	
ZnP	2.3(1)	2.90(1)	9.1(9)	

CN = coordination number; R = interatomic distance; σ^2 =Debye-Waller; R^2 = best fit factor; *fixed parameter
The number in brackets indicates the uncertainty on the last digit of the refined parameters.

In all the samples, Zn is bound to oxygen, the average Zn-O coordination number in plant samples is near 4.5, with bond distances at around 2 Å, slightly shorter for stem and inner root samples. All the samples have σ^2 around 10^{-2} Å^2, slightly higher for stem and inner root samples. This demonstrates that Zn is mainly tetrahedrally coordinated to O atoms in plant matrices.

For two samples: inner root and stem, the analysis was reliably extended to the next neighbour coordination shells to get some more information about the average Zn chemical environment. These spectra are compared with that of hydroxyapatite, because this is the main phase in these samples observed by LCA. Figures S7a and b report k-space experimental data and best fit curves, and moduli of the Fourier transforms of experimental data and best fit curves, respectively. When fitting the hydroxyapatite spectrum, the CN was fixed to the crystallographic values. The best fits show that Zn occurs mainly in tetrahedral coordination (CN 4.3) for the oxygen shell at 1.92 Å in

the inner root. In stems, a weak elongation of the ZnO shell (1.97 Å) and the small increase of the ZnO coordination number (CN 4.8) suggest some larger fraction of octahedrally coordinated ZnO_6.

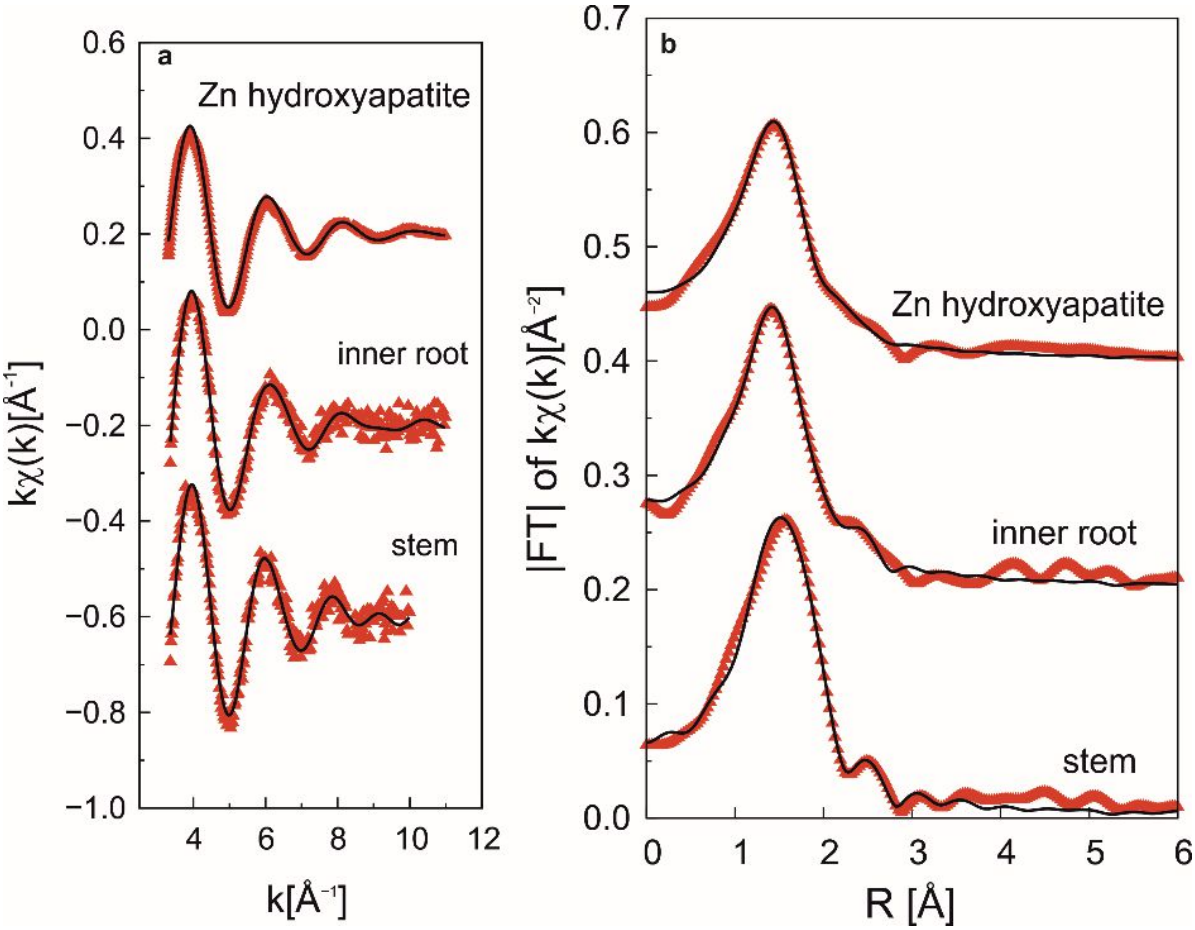

Figure 28. Experimental data (red triangles) and best fits (smooth lines) of Zn hydroxyapatite reference compound, inner root and stem samples EXAFS spectra (a), and Moduli of the Fourier transforms of experimental k χ(k) and best fit curves.

The analysis was extended to the next neighbour coordination shells and two ZnP shells were found at about 2.66 Å and 2.89 Å. These contributions improve the quality of the best fit in the R region up to 3 Å in the Fourier Transforms characterized by a weak but evident tail in the experimental curves. It is worth noting that XAFS technique can provide structural information restricted to a few Å (up to about 5-6 Å) around the absorber. Therefore, our results (XANES and EXAFS analysis) provide evidence that the coordination environment of Zn in these samples is similar to that of some

reference compounds. While the presence of a hydroxyapatite phase cannot be definitively demonstrated, our results suggest that Zn mainly occurs in a tetrahedral coordination environment in the inner root, and that a fraction of Zn could have 6-fold coordination in the stem. This is consistent with the increase of both the coordination number and interatomic distance (Tang et al., 2009), and with the contribution from smithsonite required for the LCA.

Chapter 5 - Analysis of plants grown in natural catchment

5.1 Chemical and mineralogical characterization

X-ray powder diffraction analysis of internal part of the root of *Juncus acutus* (Fig. 29a) and *Phragmites australis* (Fig. 30a) and external surface (Fig. 29b and 30b) showed the presence of amorphous cellulose recognizable from the wide peaks at 2θ values of approximately 10°–14°. Minor peaks also were seen and can be attributed to the presence of quartz and whewellite [$Ca(C_2O_4) \cdot (H_2O)$]. These minerals were observed in both the parts of the root. Rhizosphere mineralogy of *Juncus acutus* from Naracauli (Fig. 29c) consisted of quartz, hemimorphite, hydrozincite, siderite, gypsum, while rhizosphere of *Phragmites australis* (Fig. 30c) from San Giorgio consisted of quartz, calcite, dolomite, smithsonite, and hemimorphite.

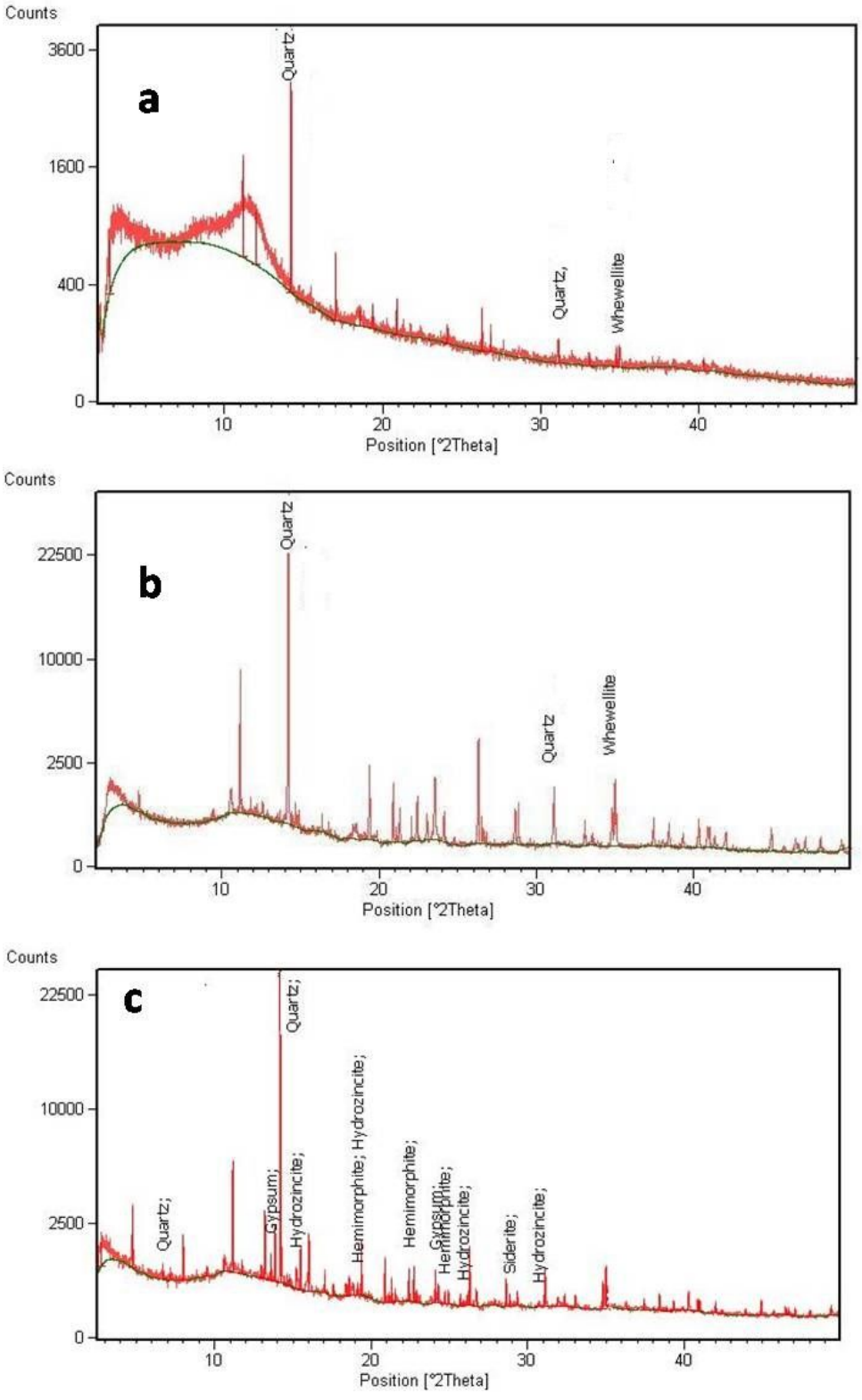

Figure 29. S-XRPD analysis of internal part of root (a) and external surface (b) of Juncus acutus of Naracauli (a) showed peaks of whewellite, quartz and amorphous cellulose. S-XRPD analysis of rhizosphere (c) of Juncus acutus of Naracauli showed quartz, gypsum, hemimorphite, siderite, hydrozincite (λ=0.82954; in figure are showed only mainly peak)

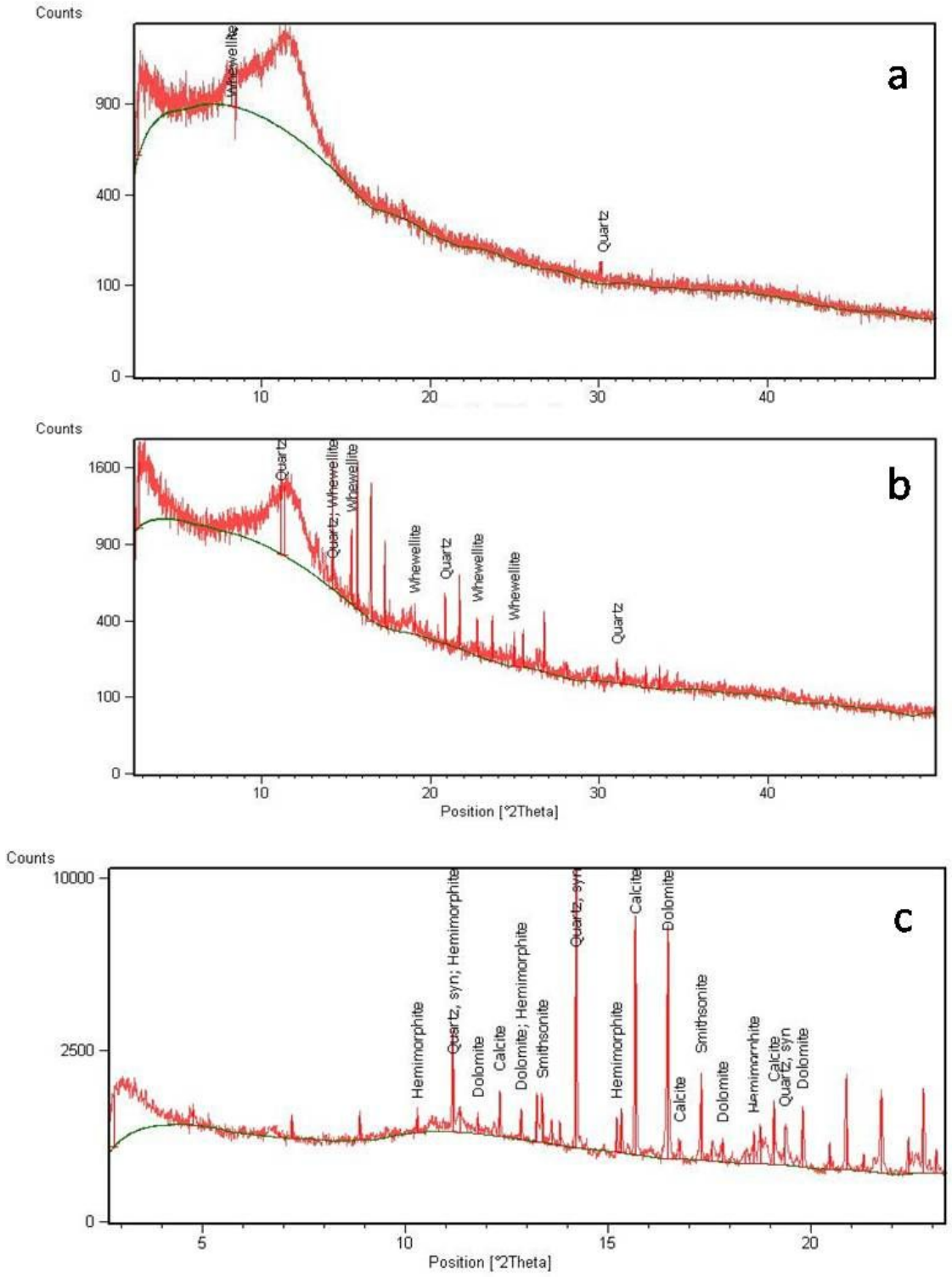

Figure 30 S-XRPD analysis of internal part of root (a) and external surface (b) of Phragmites australis of San Giorgio (a) showed peaks of whewellite, quartz and amorphous cellulose. S-XRPD analysis of rhizosphere (c) of Phragmites australis of San Giorgio showed quartz, gypsum, hemimorphite, siderite, hydrozincite (λ=0.82954; in figure are showed only mainly peak)

Table 10 shows Zn contents in *Juncus acutus* and *Phragmites australis* collected in mine areas in SW Sardinia. *Juncus acutus* had greater contents of Zn than *Phragmites australis*, and *Juncus acutus* grown in San Giorgio areas had greater contents of Zn than plants in the Naracauli area.

Table 10. Content of Zn in plant collected in mine areas, root surface was gently washed before chemical analysis.

	Leaves	***Stems***	***Inner part of Roots***	***External surface of Roots***
	(ppm)	(ppm)	(ppm)	Ppm
Phragmites australis Naracauli	68 (±2)	125 (±4)	545(±16)	799(±24)
Phragmites australis Rio San Giorgio	72 (±2)	132(±4)	524(±16)	833(±25)
Juncus acutus Naracauli		467(±14)	2675(±80)	17500(±525)
Juncus acutus Rio San Giorgio		650(±20)	3050(±92)	19050(±572)

Figure29 shows SEM images of root, not washed prior to observation as for chemical analysis, of *Juncus acutus* and *Phragmites australis*. Morphology of the inner part and external surface shows significant differences, and grains of minerals adhering to the plant roots. External surface of root was mainly made up of Si, Al, Fe and Zn. The O and C signal derives from the organic matter, whereas Si, Al, Zn and Fe were related to the mineral. Signals of Si, Al, Zn and Fe decrease in intensity in the inner part of the root with respect to the external part. These data clearly suggest that the plant root activity, through processes occurring at the rhizosphere and root surfaces, drives mineral evolution and results in formation of layered mainly made of Si, Al, Fe, Zn and O likely originating from biomineralization processes.

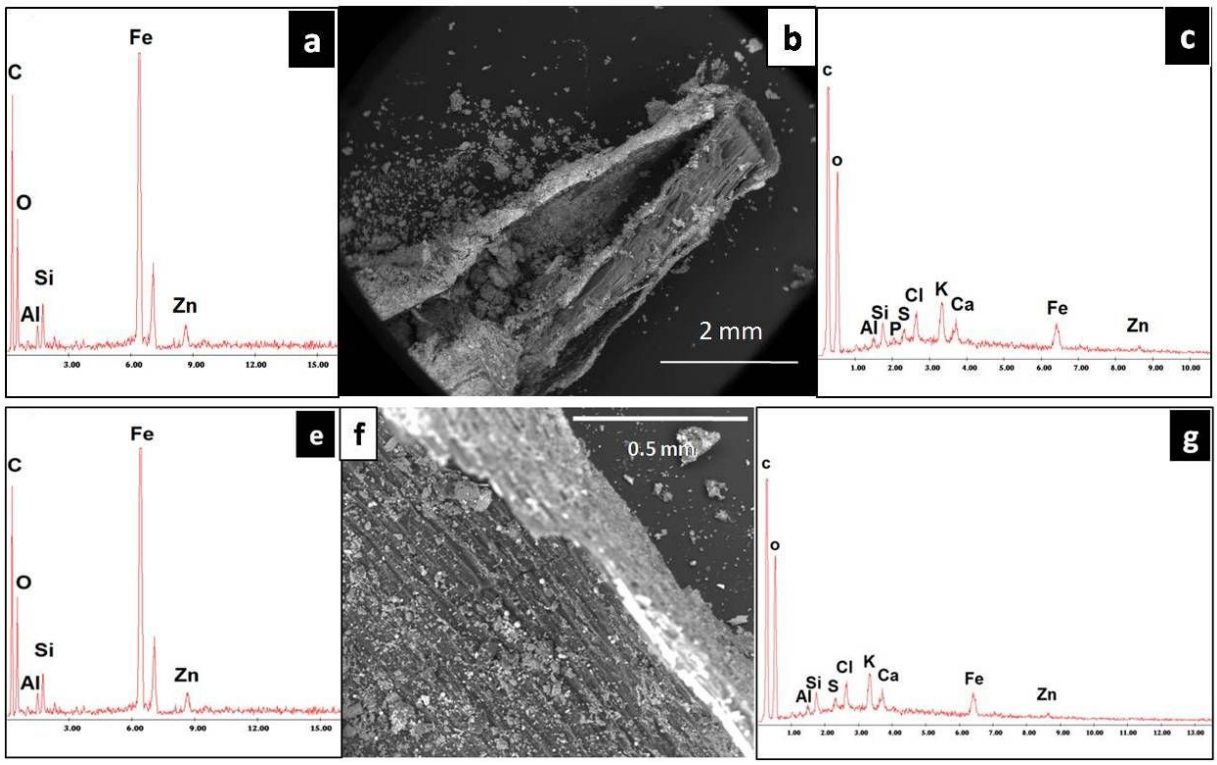

Figure 31. SEM image of root of Juncus acutus -Naracauli (b), EDS analysis of external surface (a) and internal part (c) and SEM image of root ofPhragmites australis (f), EDS analysis of external surface (e) and internal part (g)

5.2 Element distribution

Figure 30 shows two different kinds of images: i) bright field (absorption) image (Fig.30a and 30c); ii) LEXRF maps of Al, Si, Zn and Fe (30 b,d). Images of *Juncus acutus* and *Phragmites australis* show the same pattern of element localization. Al and Si are mainly localized in the external surface of the roots, forming a rim (Fig.30), whereas Fe and Zn are localized also in the inner part of the plant root.

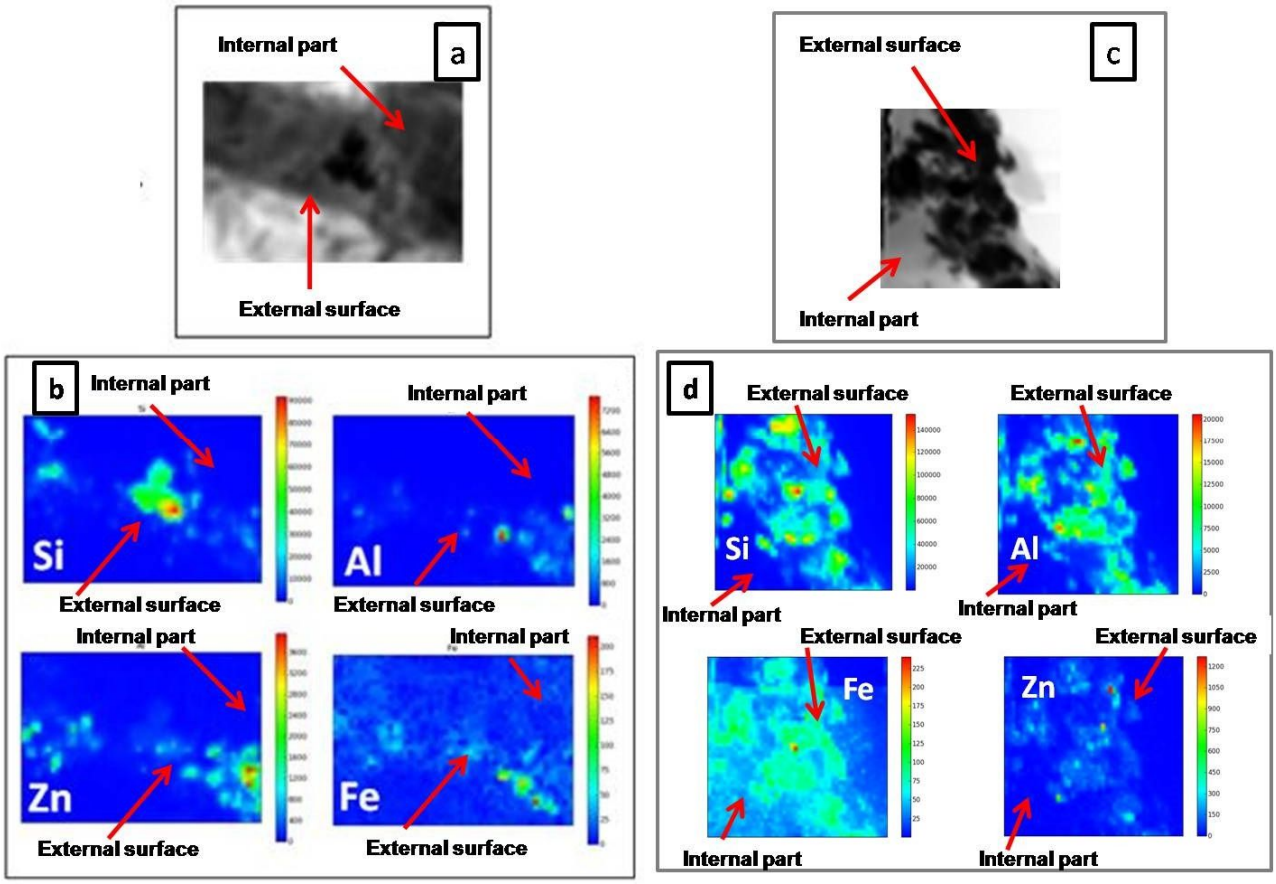

Figure 32. Selected samples of Juncus acutus (a) and Phragmites australis (c) For each sample the following images are shown: i) ordinary light ii) LEXRF maps of Al, Si, Zn and Fe (size 80 × 80 µm2, scan 80 × 80 pixels).

Plants have developed different mechanisms to minimize exposure to high concentrations of trace metals (Manara et al.,2012) by controlling metal bioavailability to their roots. One of these mechanisms is to secrete root exudates, that can result in acidification, chelation, precipitation and redox reactions, or by inducing variations in physical and chemical properties of the rhizosphere by which plants are able to affect metal bioavailability (Kidd et al. 2009). The most recent literature suggests mechanisms of Zn (bio)storage in *Phragmites australis* and *Juncus acutus* roots include metal-organic complexes, but also to biomineral phases of Si and P for istance emimorphite (Medas et al. 2015; De Giudici et al. 2015; Caldelas et al. 2016, for a review). Analysis of *Phragmites australis* and *Juncus acutus* in this work show that Si and Al are mainly concentrated in

the external surface of the roots, and crystalline forms (quartz, whewellite) occur both in the surface of the plant roots and internally. This process is intrinsically biologically driven, and leads to a decrease of Zn concentration from the root surface to the internal part of the root.

Chapter 6 - Studies in controlled system: rhizobox experiment

The rhizobox experiments were devised to shed light on the individual roles of water, plant and substrate in the interaction between biosphere and geosphere.

6.1 Water characterization

Rhizoboxes were watered by two lines of irrigation, the first with polluted water (180 ppm of Zn-line A), the second with unpolluted water (0.050 ppm of Zn-line B). Table 11 shows samples of water drainage collected at the end of the experiment. Zn concentration, after interaction with plants and substrates (polluted and unpolluted), was lower with respect to the starting condition except for line B Sa Masa and Naracauli substrates. For all the other conditions Zn is removed from the water by mineral precipitation, adsorption processes or biogeochemical processes.

Table 11. ***Zn content in the water drainage collection at the end of the experiment in rhizoboxes with Juncusacutus and Phragmites australis***

	Juncus acutus		*Phragmites australis*	
	Line A (180 ppm initial)	**Line B (0.050 ppm initial)**	**Line A (180 ppm initial)**	**Line B (0.050 ppm initial)**
	Zn (ppm)		*Zn (ppm)*	
Unpolluted Substrate	0.01	0.01	0.01	0.01
Sa Masa Substrate	1.2	1	2	0.9
Naracauli Substrate	8	0.5	-	-

6.2 Substrate characterization

At the begin of the rhizobox experiments, Zn concentration was higher in Sa Masa substrate (20390 ppm) than in Naracauli substrate (9720 ppm). In unpolluted substrate Zn concentration was 140ppm.

XRD analysis shows no significant differences between the initial mineralogy and the mineralogy at the end of the experiment. However, efflorescent salts were observed in the surface of substrate, indicating that processes of mineral dissolution and reprecipitation were active. XRD analysis (Fig. 31) shows that these salts consisted mainly of gypsum, hemimorphite, and hydrozincite.

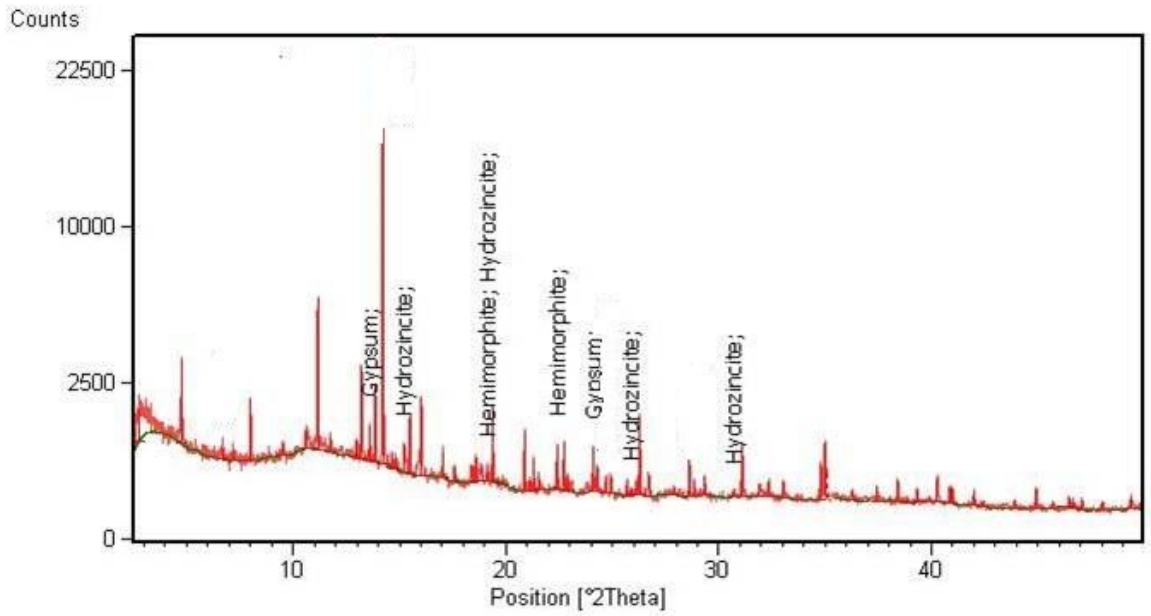

Figure 33. S-XRPD analysis of efflorescent salt precipitated in rhizoboxes withNaracauli substrate and Juncus acutus shows gypsum, hemimorphite, hydrozincite (λ=0.82954)

Figure 34 shows the near-edge region of the normalized spectra of salts precipitated on the surface of substrate, and selected reference compounds, hydrozincite and hemimorphite. The Zn K-edge XANES spectra of salt samples are highly similar, indicating that the ionization state and

coordination chemistry are largely the same for the two samples. Comparing the Zn XANES features of salts with the reference compounds, the analogies with the hydrozincite (green dashed lines) and hemimorphite (red dashed lines) spectra are evident (Fig. 32a). The Zn EXAFS spectra kχ(k) of salts and reference compounds are shown in Fig. 32b. The comparison of the EXAFS spectra of the salt samples with reference compounds, confirms the close analogy among the Zn local structure in salt samples and that in hydrozincite and hemimorphite. This result suggests that hemimorphite and hydrozincite could reprecipitate as efflorescent salts temporarily limiting the mobility of Zn.

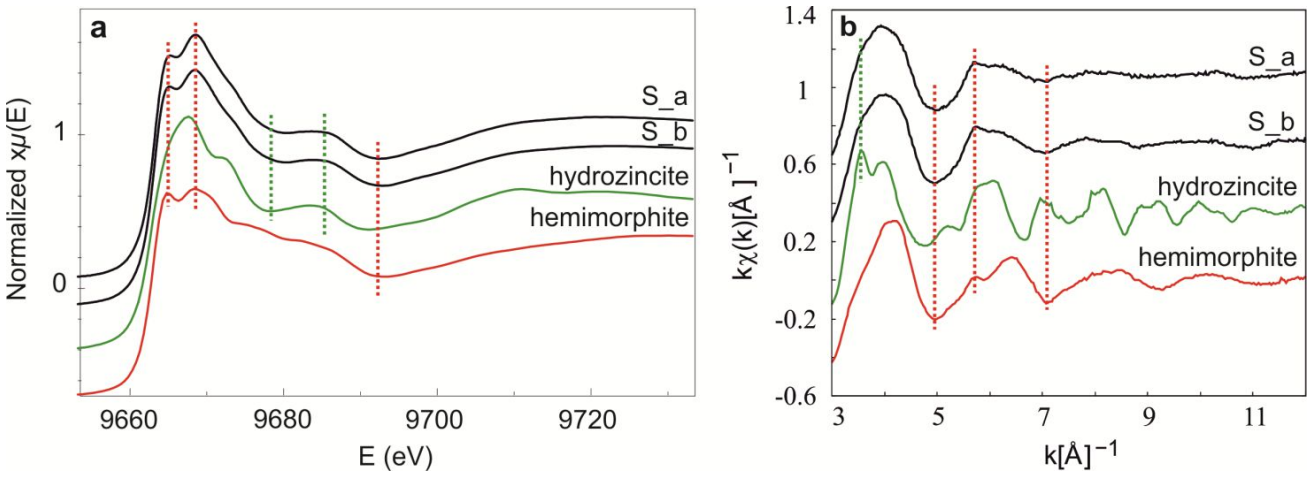

Figure 34 Zn XANES spectra (a) and Zn EXAFS spectra (b) collected on salt samples (S_a and S_b), and selected reference compounds (hydrozincite and hemimorphite), vertically shifted for the sake of clarity. Green and red dashed lines indicate similarities of salt spectra with hydrozincite and hemimorphite spectra, respectively.

Table 12 shows contents of C, H and N (expressed in %) of three substrates used in the rhizobox experiment. The highest content of C was observed in Sa Masa substrate (8.95%), unpolluted substrate and Naracauli show values of, respectively, 3.04% and 1.16%.The highest content of H was in unpolluted substrate (1.01%) followed by Naracauli and Sa Masa (0.428 and 0.225%, respectively). No N was detected in Sa Masa substrate.

Table 12. Contents of C, H and N expressed in % (n.d.: value not detected)

	C %	H%	N%
Unpolluted substrate	3.04	1.01	0.361
Sa Masa substrate	8.95	0.225	n.d.
Naracauli substrate	1.16	0.428	0.257

The overall amount of Zn supplied to each rhizobox (3 kg of substrate) via watering during the whole experiment is 3000 mg . Figure 35 shows Zn contentin substrate irrigated with polluted water (Line A) after the experiment. No significant variation was observed in Sa Masa substrate, while in Naracauli substrate Zn increases from 9720 ppm to 12490 ppm (28%).Also the increase in Zn concentration for unpolluted substrate was around 3000 ppm (from 137 ppm to around 3000 ppm). Concentration of Zn in substrate of rhizobox irrigated whit unpolluted water (Line B) is shown in Figure 35. Substrates irrigated with unpolluted water show variation within the experimental errors.

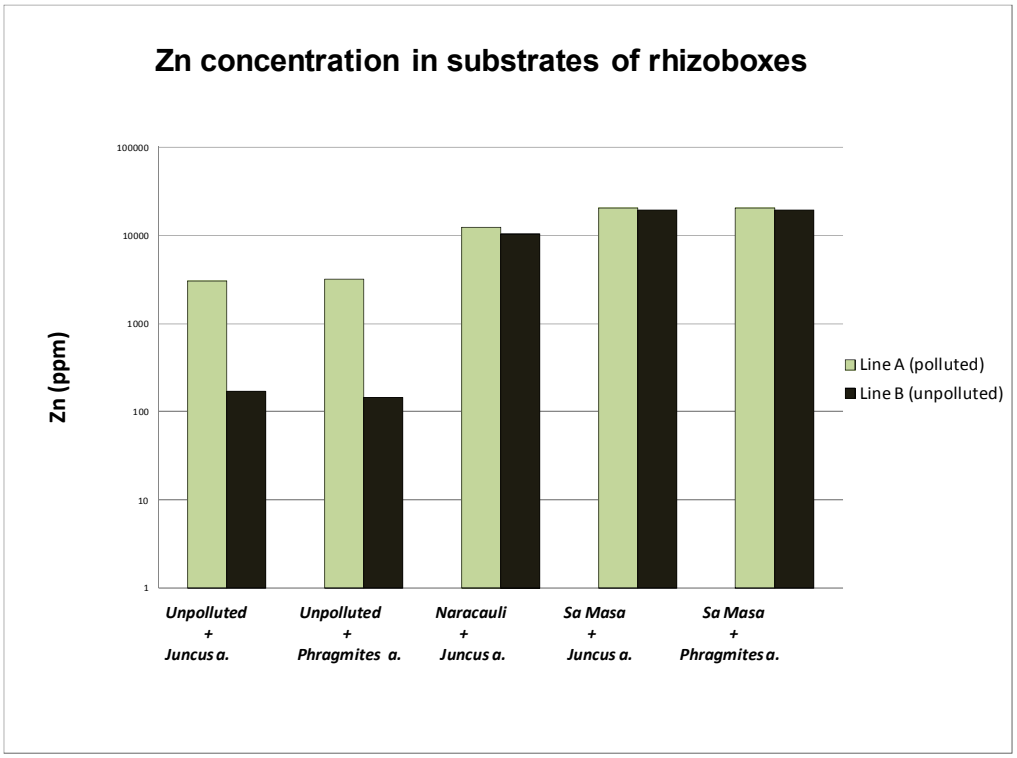

Figure 35. Graphic shows concentration of in substrates after experiment. Line A and B refers to the watering quality (Zn content).

6.3 Plant characterization

Growth of plants during rhizobox experiment was monitored monthly from May to September 2015. As a parameter to define the plant growth, height of *Juncus acutus* and *Phragmites australis* was measured from the surface of substrate to the highest part of the plant (Appendix 6). Growth of *Juncus acutus* watered with polluted water is shown in Fig. 34a while growth under watering with unpolluted water is shown in Fig.36b. The three curves represent height of *Juncus acutus* in different substrates, unpolluted, Sa Masa and Naracauli.

Plants of *Juncus acutus* grown in unpolluted substrate have shown higher development (maximum value: 29 cm) than plants grown unpolluted substrates (maximum value: 20 cm) .*Juncus acutus* grown in Sa Masa substrate was slightly favoured, likely by the higher concentration in C. However, given the limited number of rhizoboxes, statistics are poor and the slight differences in plant growth depending on the quality of watering lines (A, B) cannot be further treated.

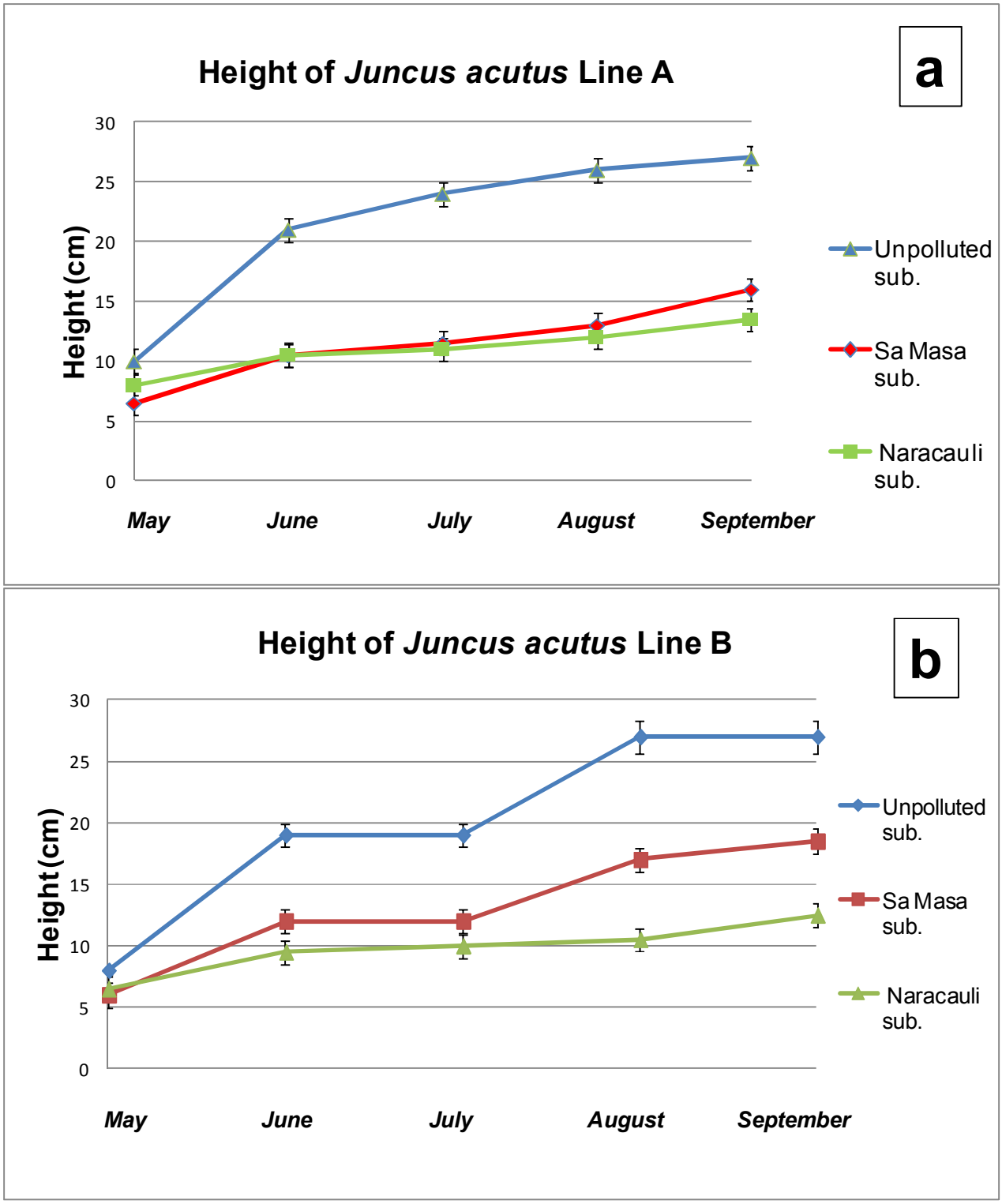

Figure 36. Graphics shown growth of Juncusacutus in unpolluted substrate (blue line), Sa Masa substrate (red line) and Naracauli substrate (green line)watered with polluted water (a) and unpolluted water (b,),

The mean height of *Phragmites australis* individuals grown in different substrates and watered with polluted water and unpolluted water is shown in Figure 37 a and b. Plants grown in unpolluted substrate have shown a greater increase in size than plants grown in Sa Masa substrate.

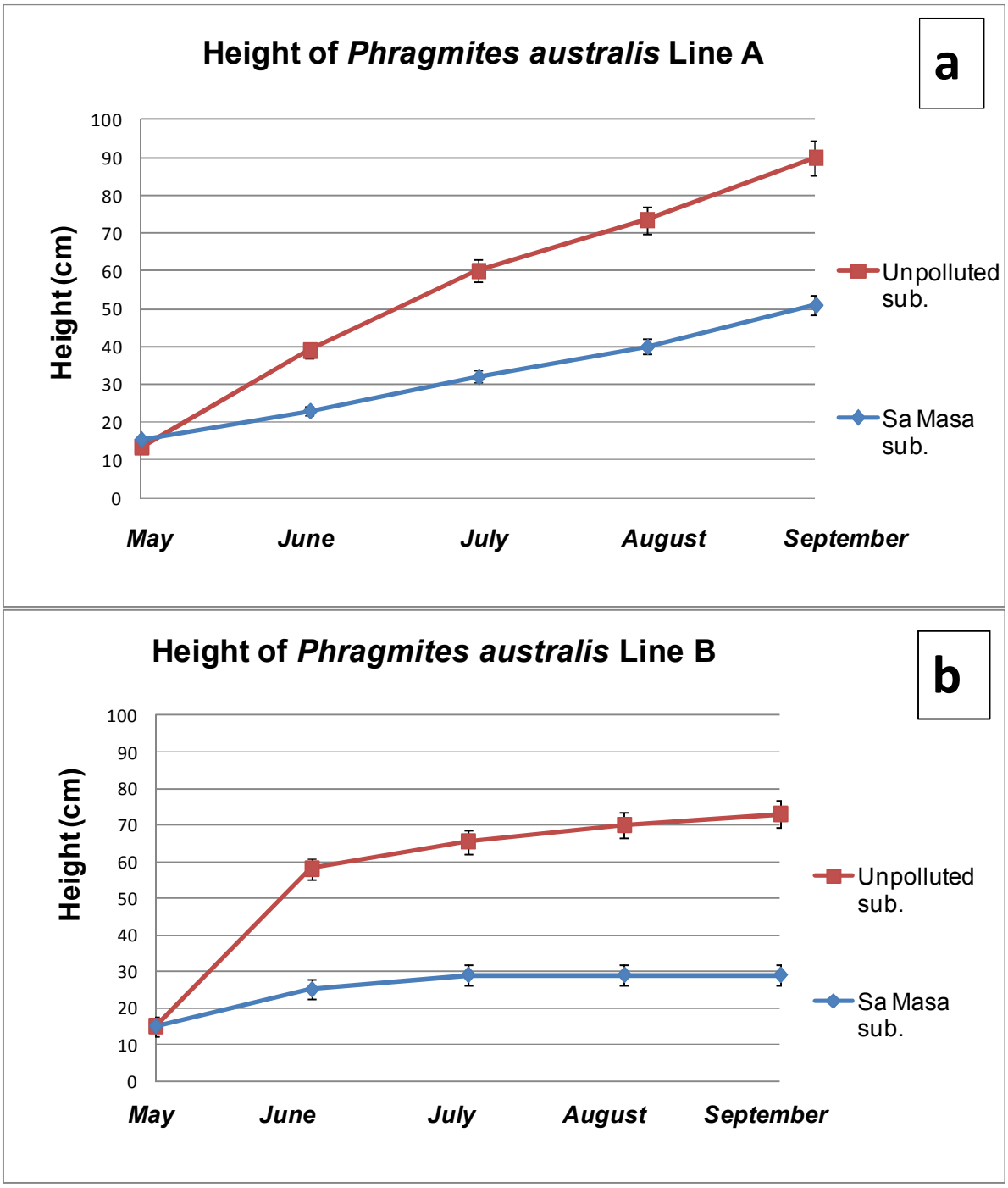

Figure 37. Graphics shown growth of Phragmites australis in all substrates irrigated with polluted water (a) and unpolluted water (b), unpolluted substrates (red line - APT, BPT) and Sa Masa substrate (blue line - APSM, BPSM).

The availability of organic matter, thus nutrient availability, indicated by CHN analysis, suggests that the most suitable substrate for the plants growth are, respectively, unpolluted substrate, followed by Sa Masa substrate and Naracauli substrates. Metal content is higher for Sa Masa than for Naracauli, however the mineralogy differs by the presence of hydrozincite, gypsum, siderite and muscovite in Naracauli, while smithsonite is abundant in Sa Masa. This could imply a different bioavailability of the metals in the different substrates. Plant growth values confirms that unpolluted is better than Sa Masa and that the worst substrate is Naracauli.

After six months, plants were removed and processed in the laboratory. All triplicates were composited because there was not enough material in each rhizobox to performed chemical analyses. Due to the nature of the plants, and their shape in the rhizobox, two kinds of samples were obtained from *Juncus acutus*: stems and roots. Three kind of samples were obtained for plants of *Phragmites australis* leaves, stems and roots. Trends for Zn concentration indifferent parts of the plants are shown in Fig. 38 (see Appendix 7). Zn concentration increases in the order: i) leaves, ii) stem, and iii) roots for *Phragmites australis* and i) stem, and ii) roots for *Juncus acutus*. Under the same experimental conditions *Juncus acutus* had greater concentrations of Zn than *Phragmites australis*. The maximum value of Zn was observed for *Juncus acutus* grown in Sa Masa substrate, in both lines. In *Phragmites australis* grown in Sa Masa, the values of Zn in leaves and stem are slightly smaller in line A (leaves 1200 ppm and stem 1240 ppm) than in B (leaves1340 ppm and stem 1350 ppm). On the other hand, the value of Zn in root is clearly higher in line A (4110 ppm) than in line B (1560 ppm). In *Phragmites australis* grown in unpolluted substrates, all the Zn concentration values are higher under polluted water supply (line B) compared to unpolluted water of line A. *Juncus acutus* showed a direct relationship between the content of Zn in plant compartment, in soil and in water. As pointed out by Caldelas et al. (2011) and Caldelas and Weiss (2016), the observed variability in Zn concentration trends for *Phragmites australis* is ruled by

mechanisms adopted by plant physiological response to a need for Zn or an excess of Zn. It is worth noting that Caldelas and co-authors, and many literature works considered in the Caldelas and Weiss (2016) review, investigated hydroponic grow of plants (that is, no minerals nor solid substrate but only water added with nutrients).Thus, this work makes some step ahead to the understanding of the relationship between physiology of plants and bioavailability controlled by soil minerals.

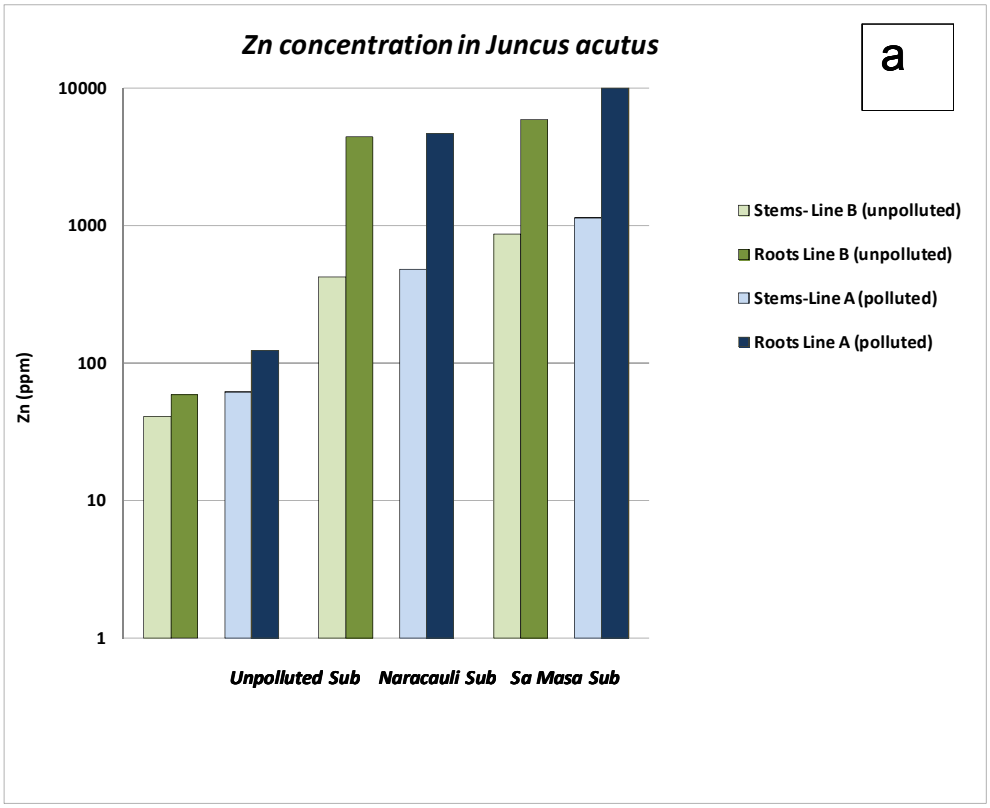

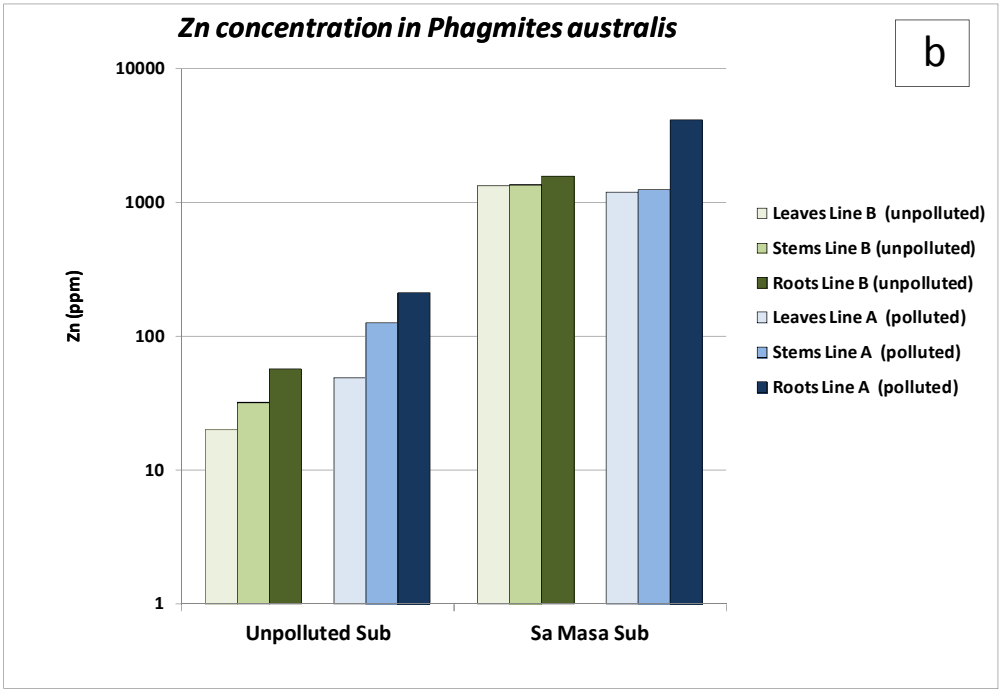

Figure 38. Concentration of Zn in each part of Juncus acutus and Phragmites australis is higher in roots that in aerial part and it depends of substrate where plants are grown.

In tolerant plants grown in environments with excess Zn, roots play an important role in Zn detoxification and sequestration. The physiological response of tolerant plants to high Zn levels can cause significant changes in the distribution of Zn isotopes across the plant organs in some species (Caldelas, 2016). Zn excess can lead to precipitation with insoluble phosphates or silicates at the root epidermis (Medas et al. 2015; De Giudici et al. 2015; De Giudici, Pusceddu et al. 2017), the intercellular spaces, and the cell walls of the roots, a process termed biomineralization, that might reduce Zn influx into the symplast (Neumann and zur Nieden 2001; Straczek et al. 2008).In Figure 38two different kinds of images are reported: i) bright field (absorption) image (a,c); ii) LEXRF maps of Al, Si, Zn and Fe (b,d). Images of *Juncus acutus* and *Phragmites australis* roots sections shows the same shape in the localization of elements. Al and Si are mainly localized in the root epidermis, whereas Fe and Zn are localized also in the inner part of the plant root, showing a general decrease in concentration from the root rim towards the internal part. STXM analysis suggests that the localization of Zn at the roots of *Juncus acutus* is similar to that found for *Pistacia Lentiscus*, *Phragmites australis* and *Euphorbia pithyusa* (De Giudici et al, 2015, 2017; Medas et al, 2015). Likely,also for *Juncus acutus*, this distribution is due to a biomineralization process driven by the plant and aimed to decrease the translocation of Zn from the roots to the stems.

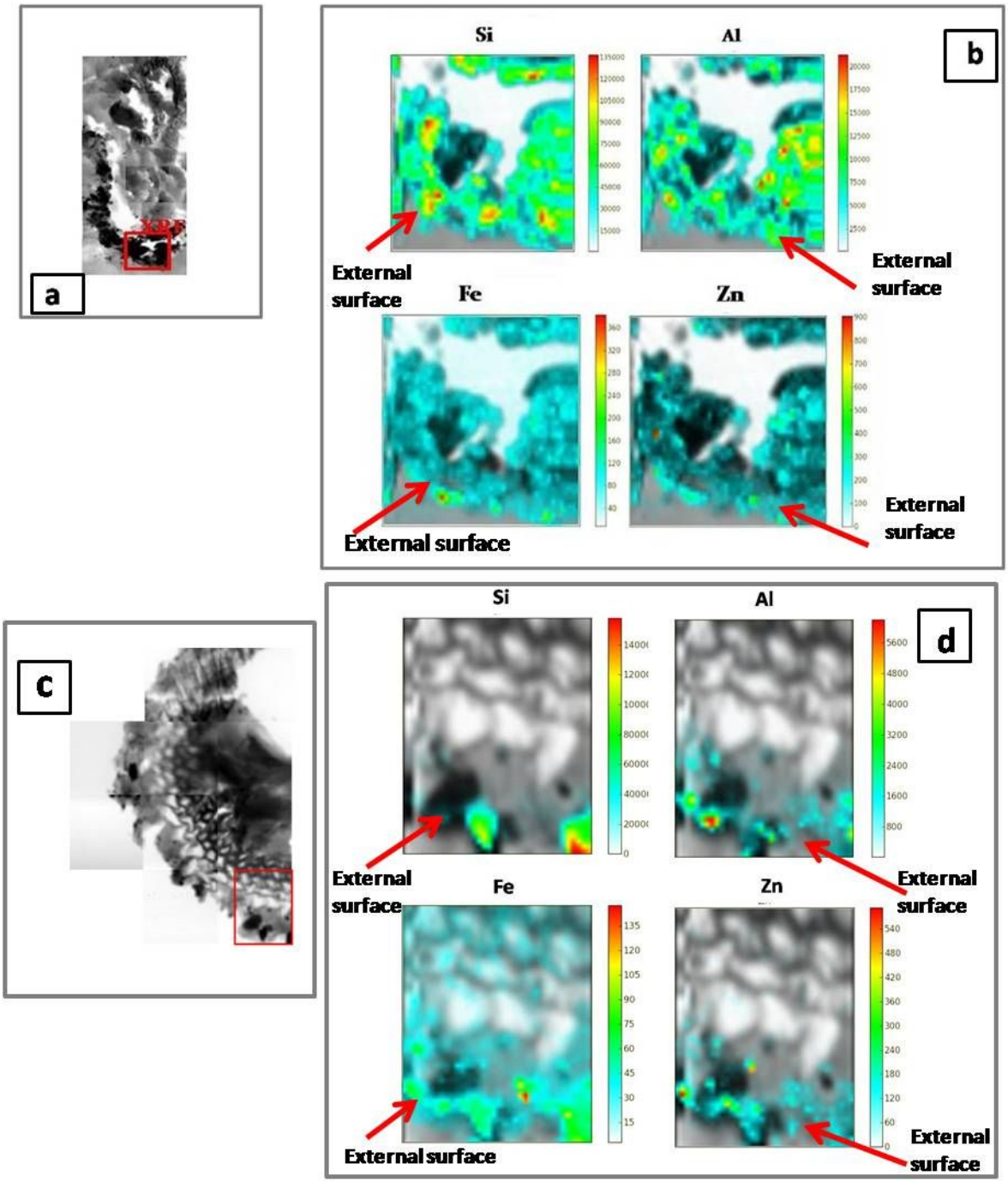

Figure 39 STXM Distribution of Zn, Si, A land Fe in external surface of root of Juncus acutus 80x80 µm (a, b) and Phragmites australis in Sa Masa substrate 60x80 µm (c,d)

In our greenhouse experiment, Zn levels were much higher in the below-ground parts of *Juncus acutus* (Naracauli substrate) than in the aerial structures, reaching maximum values ca. 2500 ppm in the roots. These results revealed that *Juncus acutus* could have the basic characteristics of a tolerant

plant with high capacity for the phytostabilization of metal in its below-ground structures. The lower Zn concentration observed in stems of *Juncus acutus* compared to that in roots could be related to the development of mechanisms such as compartmentalization, which would control ion transport into the aerial part, thereby improving plant tolerance to heavy metals (Mateos-Naranjos et al., 2014). Thus, at a first glance, this species may have accumulated in the roots most of the Zn that was taken up, to minimize Zn translocation to above-ground tissues.

The intensity of metal uptake by plants can be described by using coefficients already defined in the literature (Fellet et al., 2007). Some slight difference in the use of these coefficients is to be noticed, particularly in the threshold values to be adopted to distinguish between different behaviours of plants. In this work, the following parameters were adopted: translocation factor (TF),biological concentration factor (BCF) and accumulation coefficient (BAC). These are defined as follows:the ability of the plant to transfer metal from roots to stems, leaves, fruits and seed is the translocation factor (TF). This is defined as the ratio between the concentration of a given metal in the aerial part of the plant (leaves, stems- [Me]) and the concentration of the metal in the roots ([Mr]); (Brunetti et al, 2009)

$$TF=[Me]/[Mr]$$

The ability of the plant to transfer metal from substrates to roots is often defined as the biological concentration factor (BCF). This is the ratio between the concentration of a given metal in roots- ([Mr]) and the concentration of the metal in the substrate ([Ms])(Fellet et al. 2007):

$$BCF=[Mr]/[Ms]$$

The ability of the plant to transfer metal from substrates to stems, leaves, fruits and seed is often defined as the bioaccumulation factor (BAC). This is the ratio between the concentration of a given

metal in leaves and stem- ([Mp]) and the concentration of the metal in the substrate ([Ms]) (Marchiol et al. 2013):

$$BAC=[Mep]/[Ms\ ]$$

Figure 40a shows values of translocation factor of *Juncus acutus* and *Phragmites australis*. *Juncus acutus* had a low value to TF in polluted substrate (Sa Masa TF=0.1 and Naracauli TF=0.1 for both lines of water) while TF value is higher in unpolluted substrate, especially in the unpolluted line (polluted line TF=0.5, unpolluted TF=0.7). *Phragmites australis* had greater values of TF than *Juncus acutus;* in unpolluted substrate the TF value is 0.8 for the polluted line and 0.9 for the unpolluted line, in Sa Masa substrate the biggest difference between the polluted line (TF=0.6) and unpolluted line (TF=1.7) was observed.

Figure 40b shows value of BCF for *Juncus acutus* and *Phragmites australis. Juncus acutus* in polluted substrate had BCF values between 0.30 and 0.40. Unpolluted substrate had values of 0.04 for the polluted line and 0.30 for the unpolluted line. *Phragmites australis* in Sa Masa substrate had values of 0.20 for the polluted line and 0.07 for the unpolluted line, while unpolluted substrate had values of 0.39 for polluted line and 0.07 for unpolluted line. In unpolluted substrate with *Juncus acutus* and *Phragmites australis* the water influences the value of these factors. BCF of Naracauli substrate did not depend on the quality of water in the lines, in fact both are very similar.

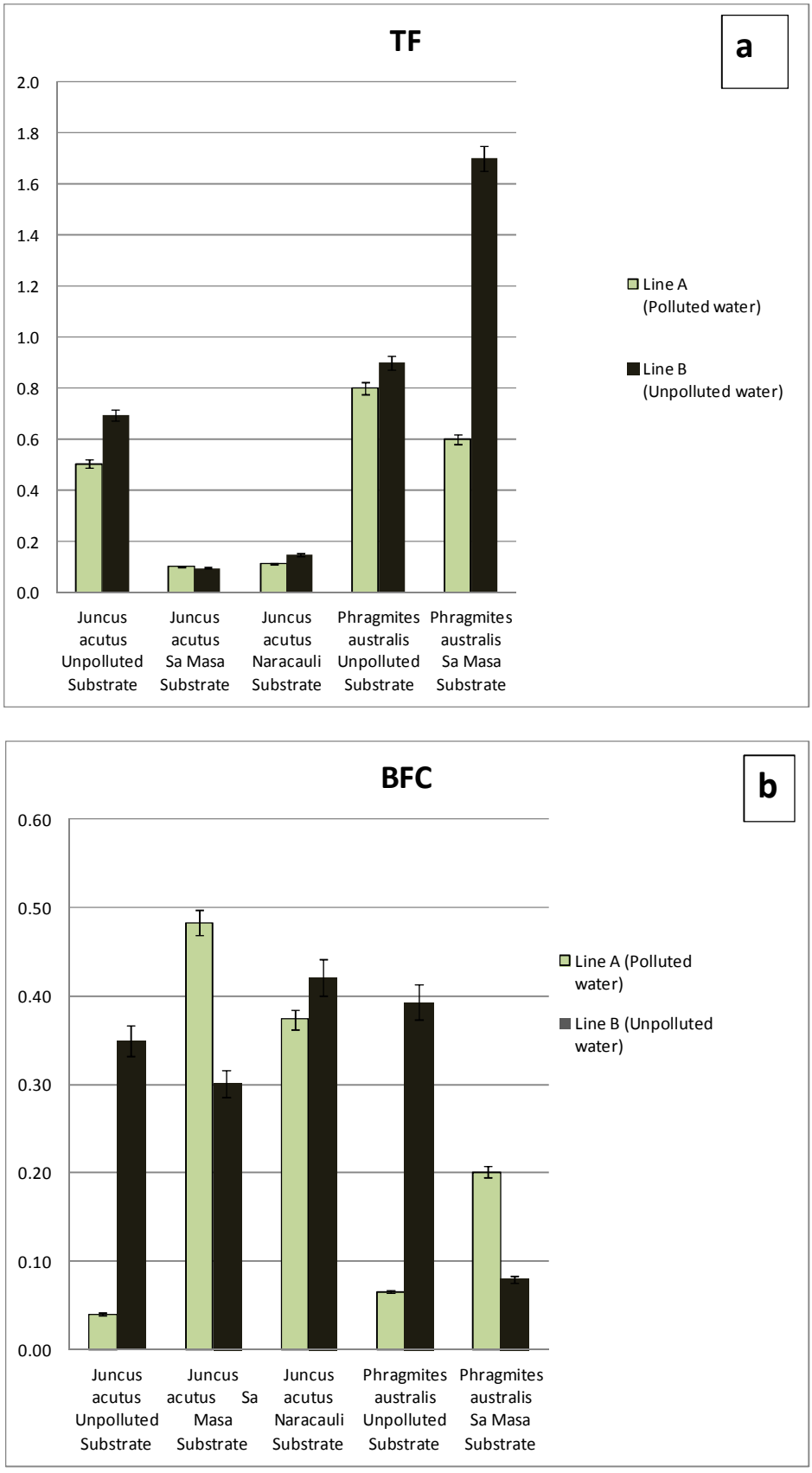

Figure 40. Graphics of translocation factor (a) and biological concentration factor (b)

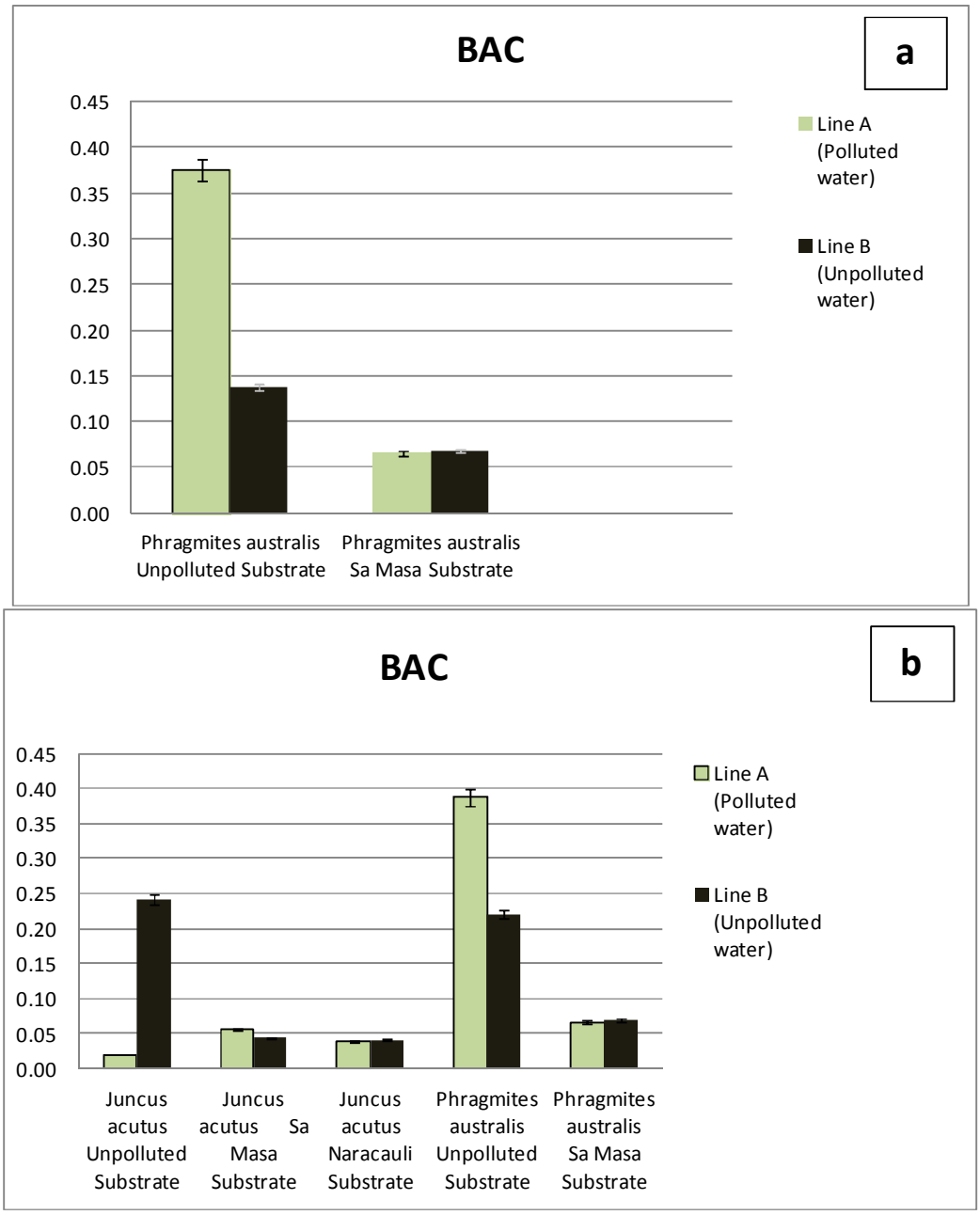

Figure 41. Graphics of Bioaccumulation factor calculated as ratio between leaves and substrate (a) and stems and substrate (b)

6.4 Zn isotope fractionation factors, preliminary results on *Juncus acutus* grown in Naracauli substrate with polluted water

As previously mentioned, isotopic fractionation factor is recognized to be a useful tool to understand how plants respond to excess Zn conditions. Rhizobox experiments allows us to investigate multiple parameters such as mineralogy of the substrate and excess of Zn in water and substrates.

$\delta^{66/64}$Zn isotopic ratios are defined as:

$$\delta^{66}Zn = \left[\frac{(^{66}Zn/^{64}Zn)_{sample}}{(^{66}Zn/^{64}Zn)_{JMCave}} - 1\right] \times 1000$$

Actually, samples of *Juncus acutus* grown in Naracauli substrates and watered with spiked water were analysed for Zn isotopes (completion of isotopes analysis is planned for the next months). According to Caldelas and Weiss (2016) this corresponds to a specific condition where Zn is in excess for the plant. At the starting conditions of our experiment, the value of δ^{66}Zn for polluted water was 0.37 ‰, while for Naracauli substrate this value was 0.11‰, for Naracauli substrate at the end of the experiment, the value was 0.20‰. The δ^{66}Zn value for the roots was 0.11‰, while for stems the δ^{66}Zn value was -0.56‰.

The Zn isotopic fractionation between two samples (i and j) is calculated using Eq. 2:

$$\Delta^{66}Zn_{i-j} = \delta^{66}Zn_i - \delta^{66}Zn_j \qquad Eq.2$$

The magnitude of the fractionation factor between roots and water is $\Delta^{66}Zn_{root\text{-}solution}$- 0.26‰.$\Delta^{66}Zn_{stem\text{-}root}$ is -0.67 ‰. The $\Delta^{66}Zn_{root\text{-}final\ substrate}$ is -0.09 ‰.The $\Delta^{66}Zn_{root\text{-}final\ substrate}$ is 0‰.

Thus, fractionation factors showed a consistent depletion in heavy isotopes relative to polluted water, and a high isotope fractionation was observed during Zn translocation (Fig. 42).

In the literature (Weiss et al. 2005; Jouvin et al. 2012; Smolders et al. 2013; see also in Caldelas,2016), for hydroponically grown crops in presence of excess of Zn, the magnitude $\Delta^{66}Zn_{root\text{-}solution}$reported was smaller($\Delta^{66}Zn_{root\text{-}solution}$between -0.02 to 0.16‰) as well as $\Delta^{66}Zn_{stem\text{-}root}$ ($\Delta 66Zn_{shoot\text{-}root}$between −0.25 to -0.56‰). In this work, as the plant species was grown in a solid substrate, rather than hydroponically, the fractionation effect cannot be compared with previous values. The $\Delta^{66}Zn_{\ finalsubstrate\ -\ initial\ substrate}$ is 0.09‰ that indicates an increase in heavy isotopes. Thus, the simultaneous effect of fractionation between the matrices involved in this experiment could enhance the fractionation effect relative to that observed for experiments driven under hydroponic conditions. A new run at the USGS isotope measurement facility is actually under planning for the next months to finish the collection of isotopic data.

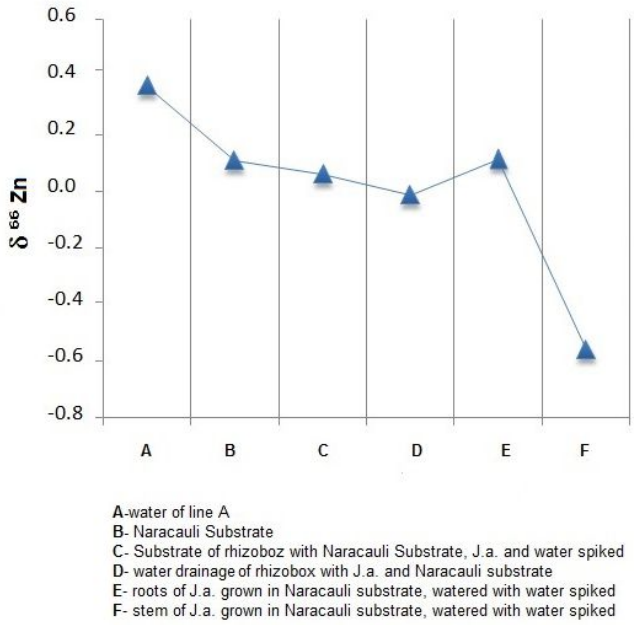

Figure 42. Graphic of fractionation factors of Zn in substrate, water, roots and stems of rhizobox with Naracauli substrate, Juncus acutus watered with spiked water.

A significant variability in the sensitivity of plants to metal exposure is documented in the literature, under high Zn supply. Caldelas et al. (2011) observed an enrichment in light isotopes in stems. On the other hand, pioneer species used to restore contaminated sites usually develop some mechanism of defence or adaptation to decrease the bioavailability of metals (Bacchetta et al.,2013; Medas et al. 2015; De Giudici 2015). Overall, the investigation of Zn localization in plant roots, chemical analysis and isotope fractionation indicates that *Juncus acutus* is clearly a metal tolerant species. The Zn tolerance is facilitated by the plant's ability to limit the translocation from roots to aerial parts, likely by biomineralization processes occurring in the roots, as shown in recent literature investigations on pioneer plants in Sardinia mines (Concas et al. 2015; Medas et al. 2015; De Giudici et al. 2015) and in other kind of substrates and climatic conditions (Neumann and zur Nieden 2001; Straczek et al. 2008;John et al.2007, Gélabert et al., 2006)

Chapter 7 Summary and Conclusion

This study investigates how the interaction between mineral and biosphere can mitigate the dispersion of trace metals in the mine environment. The focus of the study is on i) the processes that can control attenuation of trace metals, and ii) the role of the factors that participate in these processes.

Different scales of study and different investigation methods were used. Catchment scale investigation was carried out by applying hydrological tracer technique to rio San Giorgio (Iglesias, SW Sardinia; De Giudici et al. 2017). The rio San Giorgio Valley is the area with maximum amount of mine waste in Sardinia. With a synoptical sampling, both discharge and metal load were quantified. A maximum Zn load of 5,7 kg/day was found. In addition, the apparent Zn load drops from 5.7 to 2.2 kg per day, ca. 60 %, in few hundreds of meters downstream from the peak. Comparing Rio San Giorgio with Naracauli river (De Giudici et al. 2014.), the measured metal load in Rio San Giorgio was observed to be lower by, at least one order of magnitude.

By applying synchrotron techniques and other microscopic isotopic analysis the following biogeochemical barriers were recognized to be active in the hyporheic zone:

- Presence of framboidal pyrite in sediments of Rio San Giorgio, and concentration of elements at the surfaces of roots, showed a first mechanism limiting trace metal mobility
- X-ray microscopy (STXM) of thin sections of *Phragmites australis* and *Juncus acutus* roots indicates that Fe and Zn are co-located together with Si and Al on the external parts of the roots.
- XAS analysis indicates that Fe speciation inside the root is dominated by oxides; Zn speciation inside the roots comprises carbonates (hydrozincite and smithsonite), Zn hydroxyapatite, and organic molecules such as Zn cysteine and Zn acetate hydrate. In the San Giorgio river, plants act as a second biogeochemical barrier by the uptake of significant amounts of Fe and Zn; the excess of Fe

and Zn inside the plants is then dropped by biomineralization processes leading to the formation of Zn hydroxyapatite-like phases.

Rhizobox experiments and isotopic analyses were conceived to make a step forward in understanding the mechanisms that rule the interaction between mineral, water and plants under controlled conditions. A different response of the plants to Zn supply was found and this depended on mineralogy, Zn concentration in waters, and the plant.

This work points out that natural abatement processes in Rio San Giorgio are favoured by multiple conditions. Specifically; the factors ruling efficiency of biogeochemical barriers in San Giorgio are:

- Dense vegetation increases water exchange between riverbed and hyporheic zone;
- Rhizopores increase vertical permeability, and/or the wide streambed section;
- Plant roots likely enhance permeability; rhizopores induced permeability;
- Plant roots host biofilm of microbes where sulphur reduction occurs, leading to an environment that limits metal mobility.

Results from rhizobox experiments indicate that the response of the plants to Zn supply can slightly change depending of the amount and the way Zn is supplied. Overall, *Phragmites australis* and *Juncus acutus* are metal tolerant species that are suitable for phytoremediation. Particularly, as their roots are effective substrates for the formation of S-reducing microbe biofilms, these metal tolerant species are excellent candidates for phytostabilization of metals.

The innovative approach of this work was to combine research in the field with a reproduction in a controlled system to know effects of interaction between minerals and biosphere. The results obtained in this work have clarified natural attenuation processes that occur in hyporheic zone of rio San Giorgio.

The resulting information provides useful knowledge to design phytoremediation techniques in areas affected by mine pollution.

Reference

https://www.elettra.trieste.it/

Assorgia A., Brotzu P., Morbidelli L., Nicoletti M., Traversa G. (1984). Successione e cronologia (K-Ar) degli eventi vulcanici del complesso calco-alcalino oligo-miocenico dell'Arcuentu (Sardegna centro-occidentale). Period. Mineral., 53: 89-102.

Bacchetta, G., Cappai, G., Carucci, A., Tamburini, E. (2015). Use of Native Plants for the Remediation of Abandoned Mine Sites in Mediterranean Semiarid Environments. Bull. Environ. Contam.Toxicol. 94, 326–333.

Baker A J M, McGrath S P, Reeves R D and Smith J A C 2000 Metal hyperaccumulator plants: A review of the ecology and physiology of a biological resource for phytoremediation ofmetal-polluted soils. Ed G B N. Terry, and J. Vangrosveld. pp pp.85-107.

Barbafieri M, Lubrano L, Petruzzelli G. (1996). Characterization of pollution in sites contaminated by heavy metals: a proposal. Ann Chim 86, 585–594.

Bencala, K.E. (2011). Stream–Groundwater Interactions, in: Wilderer, P. (Ed.), Treatise on Water Science, Reference Module in Earth Systems and Environmental Sciences, vol. 2, pp. 537–546.

Bencala, K.E., Gooseff, N.M., Kimball, B.A. (2011). Rethinking hyporheic flow and transient storage to advance understanding of stream-catchment connection. Water Resour. Res. 47, W00H03.

Benfatto, M., Meneghini, C. 2014. A Close Look into the Low Energy Region of the XAS Spectra: The XANES Region, in: Mobilio, S., Boscherini, F., Meneghini, C. (Eds.), Synchrotron Radiation, Basic, methods and applications. Springer-Verlag, Berlin, pp. 213–240.

Boni, M., Gilg, H.A., Aversa, G., Balassone, G. (2003). The "Calamine" of southwest Sardinia: Geology, mineralogy, and stable isotope geochemistry of supergene Zn mineralization. Econ. Geol. 98, 731–748.

Byrne P., Binley, A., Heathwaite, A. L., Ullah, S., Heppell, C. M., Lansdown, K., Zhang, H., Trimmer, M., Keenan, P. (2014). Control of river stage on the reactive chemistry of the hyporheiczone. Hydrol. Process. 28, 4766–4779.

Byrne, P., Reid, I., Wood, P. J. (2010). Sediment geochemistry of streams draining abandoned lead/zinc mines in central Wales: the AfonTwymyn. J. Soils Sediments 10, 683–697.

Byrne, P, Zhang H, Ullah, S, Binley, A, Heathwaite, AL, Heppell, CM, Lansdown, K, Trimmer, M. (2015). Diffusive equilibrium in thin films provides evidence of suppression of hyporheic exchange and large-scale nitrate transformation in a groundwater-fed river. Hydrol. Proc. 29, 1385-1396

Boni M., Costabile S., De Vivo B., Gasparrini M. (1999).Potential environmental hazard in the mining district of southern Iglesiente (SW Sardinia, Italy) Journal of Geochemical Exploration 67 (1999) 417–430

Borrok, DM, Wanty, RB, Ridley, WI, Wolf, RE, Lamothe, PJ, Adams, M. (2007).Separationof copper, iron, and zinc from complex aqueous solutions for isotopic measurement.ChemGeol; 242: 400-414.

Caldelas. C., Weiss D.J. (2016). Zinc Homeostasis and isotopic fractionation in plants: a review Plant SoilDOI 10.1007/s11104-016-3146-0

Caldelas, C., Dong, S., Araus, J. L., Weiss, D. J. (2011). Zinc isotopic fractionation in *Phragmitesaustralis*in response to toxic levels of zinc. J. Exp. Bot. 62, 2169–2178.

Carmignani L., Barca S., Oggiano G., Pertusati I., Conti P., Eltrudis A., Funedda A., Pasci S. (1997). Carta Geologica della Sardegna 1:200.000. Serv Geol d'Italia.

Cavinato A., Zuffardi P. (1948). Geologia della miniera di Montevecchio. In: Notizie sull'industria del Piombo e dello Zinco in Italia, 1: 427-464. Montevecchio Società Italiana del Piombo e dello Zinco

Cidu, R., Fanfani L. (2002). Overview of the environmental geochemistry of mining districts in southwestern Sardinia, Italy. Environ. Geol. 2, 243–251.

Cidu R., Frau, F., Da Pelo, S. (2011). Drainage at Abandoned Mine Sites: Natural Attenuation of Contaminants in Different Seasons. Mine Water Environ. 30, 113–126.

Couder (2013).Zn biogeochemical cycle in highly Zn-contaminated soil-plant systems

De Giudici, G., Medas, D., Meneghini, C., Casu, M.A., Gianoncelli, A., Iadecola, A., Podda, S., Lattanzi, P. (2015). Microscopic biomineralization processes and Zn bioavailability: a synchrotron-based investigation of Pistacia lentiscus L. roots Env. Sci. Pol. Res. 22, 19352-19361.

De Giudici G., PuscedduC., MedasD., MeneghiniC., Gianoncelli A., Rimondi V., Podda F., CiduR., Lattanzi P., Wanty R., Kimball B. (2017). The role of natural biogeochemical barriers in limiting metal loading to a stream affected by mine drainage Applied Geochemistry

De Giudici, G., Wanty, R. B., Podda, F., Kimball, B.A., Verplanck, P.L., Lattanzi, P., Cidu, R., Medas, D. (2014). Quantifying biomineralization of zinc in the Rio Naracauli (Sardinia,Italy), using a tracer injection and synoptic sampling. Chem. Geol. 384, 110–119.

De Giudici, G., Podda, F., Sanna, R., Musu, E., Tombolini, R., Cannas, C., Musinu, A., Casu M. (2009). Structural properties of biologically controlled hydrozincite: An HRTEM and NMR spectroscopic study. Am. Mineral. 94, 1698–1706.

Fitz WJ, Wenzel WW (2002). Arsenic transformations in the soil-rhizophere-plant system: fundamentals and potential application to phytoremediation. J Biotechnol 99:259–278

Frau, F., Medas, D., Da Pelo, S., Wanty, R.B., Cidu, R. (2015). Environmental Effects on the Aquatic System and Metal Discharge to the Mediterranean Sea from a Near-Neutral Zinc-Ferrous Sulfate Mine Drainage. Water Air Soil Poll. 226, 55.

Gardea-Torresdey J.L., Peralta-Videa J.R., de la Rosa G., Parsons J.G. (2005). Phytoremediation of heavy metals and study of the metal coordination by X-ray absorption spectroscopy Coordination Chemistry Reviews 249 1797–1810

Gianoncelli, A., Kaulich, B., Alberti, R., Klatka, T., Longoni, A., de Marco, A., Marcello, A., Kiskinova, M. (2009). Simultaneous Soft X-ray Transmission and Emission Microscopy. Nucl. Instrum. Methods 608, 195–198.

Gianoncelli, A., Kourousias, G., Stolfa, A., Kaulich, B. (2013). Recent developments at the TwinMic beamline at ELETTRA: an 8 SDD detector setup for low energy X-ray. J. Phys. Conf. Ser. 425 pp. 182001.

Gianoncelli, A., Kourousias, G., Altissimo, M., Bedolla, D., Merolle, L., Stolfa, A., Shin, H. (2016a). Combining multiple imaging techniques at the TwinMic X-ray microscopy beamline. AIP Conference Proceedings, 1764 - Y, pp. 030002.

Gianoncelli, A., Kourousias, G., Merolle, L., Altissimo, M., Bianco, A. (2016b). Current status of the TwinMic beamline at Elettra: a soft X-ray transmission and emission microscopy stat. J. Synchrotron Rad. 23, in press.Gianoncelli, A., Morrison, G.R., Kaulich, B., Bacescu, D., Kovac, J. 2006. A fast read-out CCD camera system for scanning X-ray microscopy. Appl. Phys. Lett. 89, 251117–251119.

Giordani, P.; Modenesi, P.; Treatiach, M. (2003).Determinant factors for the formation of the calcium oxalate minerals, weddellite and whewellite, on the surface of foliose lichens. Lichenologist, 35 (3), 255–270.

Gran, G. 1950. Determination of the equivalence point in potentiometric titrations. Acta Chem. Scand. 4, 559–577.

Hylander L.D. (2016) Improvements Of Rhizoboxes Used For Studies Of Soil–Root Interactions - Communications in Soil Science and Plant Analysis

Kaser, D.H., Binley, A., Heathwaite, A. L., Krause, S. (2009). Spatio-temporal variation of hyporheic flow in a riffle-step-pool sequence. Hydrol. Process. 23, 2138–2149.

Kimball, B.A., Broshears, R.E., Bencala, K.E., McKnight, D.M. (1994). Coupling of Hydrologic Transport and Chemical Reactions in a Stream Affected by Acid Mine Drainage. Environ. Sci. Technol. 28, 2065–2073.

Kimball, B.A., Runkel, R.L., Walton-Day, K., Bencala, K.E. (2002). Assessment of metal loads in watersheds affected by acid mine drainage by using tracer injection and synoptic sampling: Cement Creek, Colorado, USA. Appl. Geochem. 17, 1183–1207.

Killpatrick, A.F., Cobb, E.D. (1985). Measurement of discharge using tracers, USGS, United States Government Printing Office: Washington, https://pubs.usgs.gov/twri/twri3-a16/pdf/TWRI_3-A16.pdf

Kothe, E.; Büchel, G. (2014)UMBRELLA: Using MicroBes for theREgulation of heavy metaL mobiLity at ecosystem and landscape scAle(Editorial). Environ. Sci. Pollut. Res. 2014, 21 (11), 6761−6764

.Lausi A., Polentarutti M., Onesti S., Plaisier J.R., Busetto E., BaisG.,Barba L., Cassetta A., Campi G., Lamba D., Pifferi A., Mande S.C., Sarma D.D., Sharma S.M. and Paolucci G. (2015) Status of the crystallography beamlines at Elettra Eur. Phys. J. Plus 130: 43 1543-3

Ma Y., N.M. Dickinson, M.H. Wong (2003) Interactions between earthworms, trees, soil nutrition and metal mobility in amended Pb/Zn mine tailings from Guangdong, China Soil Biology & Biochemistry 35 (2003) 1369–1379

Maestri E., Marmiroli M., Visioli G., Marmiroli N. (2010) Metal tolerance and hyperaccumulation: Costs and trade-offs between traits and environmentEnvironmental and Experimental Botany 68 (2010) 1–13

Marcello A., Pretti S., Valera P., Agus M., Boni M., Fiori M. (2004). Metallogeny in Sardinia (Italy): from the Cambrian to the Tertiary, 32nd international geological congress, APAT 4, 14-36, Firenze.

Mateos-Naranjo E., Castellanos E. M., Perez-Martin A. (2014). Zinc tolerance and accumulation in the halophytic species *Juncusacutus*. Environ. Exp. Bot. 100, 114–121.

McLaughlin, M. J., Zarcinas, B. A., Stevens, D. P. and Cook, N. (2000). Soil testing for heavy metals. Communications in Soil Science and Plant Analysis, 31: 1661-1700.

Medas, D., De Giudici, G., Casu, M.A., Musu, E., Gianoncelli, A., Iadecola, A., Meneghini, C., Tamburini, E., Sprocati, A. R., Turnau, K., Lattanzi, P. (2015). Microscopic Processes Ruling the Bioavailability of Zn to Roots of *Euphorbia pithyusa* L. Pioneer Plant. Environ. Sci. Technol., 49, 1400−1408.

Medas, D., Lattanzi, P., Podda, F., Meneghini, C., Trapananti, A., Sprocati, A., Casu, M.A., Musu, E., De Giudici G. (2014). The amorphous Zn biomineralization at Naracauli stream, Sardinia: electron microscopy and X-ray absorption spectroscopy. Environ. Sci. Pollut. R. 21, 6775-6782.

Medas D., Cidu R., Lattanzi P., Podda F., Wanty R.B., De Giudici G. (2012) Hydrozincite seasonal precipitation at Naracauli (Sardinia – Italy): Hydrochemical factors and morphological features of the biomineralization process Applied Geochemistry 27 (2012) 1814–1820

Mendoza-Sanchez, I., Phanikumar, M.S., Niu, J., Masoner, J.R., Cozzarelli, I.M., McGuire, J.T. (2013). Quantifying wetland–aquifer interactions in a humid subtropical climate region: An integrated approach. J. Hydrol. 498, 237–253.

Meneghini, C., Bardelli, F., Mobilio, S. (2012). ESTRA-FitEXA: a software package for EXAFS data analysis. Nucl. Inst. Methods B 285, 153–157.

Moore R.D. (2005) Slug Injection Using Salt in Solution Streamline Watershed Management Bulletin Vol. 8 n. 2.

Morrison, G.R., Gianoncelli, A., Kaulich, B., Bacescu, D., Kovac, J. (2006). A fast read-out CCD system for configured-detector imaging in STXM. Conf. Proc. Series IPAP 7: 277-379.

Nematian M. A. & Kazemeini F. Accumulation of Pb, Zn, Cu and Fe in plants and hyperaccumulator choice in Galali iron mine area, Iran International Journal of Agriculture and Crop Science 426-432

Nimick, D.A., Gammons, C.H., Cleasby, T.E., Madison, J.P., Skaar, D., Brick, C.M., (2003). Diel cycles in dissolved metal concentrations in streams: occurrence and possible causes. Water Resour. Res. 39, 1247.

Parkhurst D.L., Appelo C.A.J. (1999). User's guide to PHREEQC (version 2) - A computer program for speciation, batch-reaction, one-dimensional transport, and inverse geochemical calculations. U.S. Geol. Surv. Water-Resour. Invest. Rep. 99-4259.

Payn R.A., Gooseff M.N., Glynn M.G., K.E. Bencala, Wondzell S.M (2009).Channel water balance and exchange with subsurface flow along a mountain headwater stream in Montana, United States.Water Resources Research, Vol. 4

Pribil, M., Wanty, R.B., Ridley, W.I., Borrok, D.M., (2010). Influence of sulfur-bearing polyatomic species on high precision measurements of Cu isotopic composition.Chem. Geol. 272, 49-54.

R.A.S. (2008)Piano di bonifica delle aree minerarie dismesse del Sulcis-Iglesiente-Guspinese

R.A.S. (2003)Piano regionale di gestione dei rifiuti- piano di bonifica dei siti inquinati

R.A.S. (1998). Nuovo studio dell'idrologia superficiale della Sardegna. Regione Autonoma della Sardegna, Cagliari, Ente Autonomo del Flumendosa (Scientific Responsible: C. Cao Pinna), Cagliari (in Italian).

Rascio N.. Navari-Izzo F.(2011) Review Heavy metal hyperaccumulating plants: How and why do they do it? And what makes them so interesting? Plant Science 180 169–181

Rees F., Sterckeman T., Morel J.L. (2016).Root development of non-accumulating and hyperaccumulating plants in metal-contaminated soils amended with biochar Chemosphere 142 48–55

Runkel, R.L., McKnight, D.M., Rajaram, H., (2003). Modeling hyporheic zone processes: Adv. Water Resour. 26, 901–905.

Runkel, R.L., Walton-Day, K., Kimball, B.A., Verplanck, P.L., Nimick, D.A. (2013). Estimating instream constituent loads using replicate synoptic sampling, Peru Creek, Colorado, Jour. of Hydrol. 489, 26–41.

Rycewicz-Borecki, M., McLean, J. E., Dupont, R.R. (2016). Bioaccumulation of copper, lead, and zinc in six macrophyte species grown in simulated storm water bioretention systems. J. Environ. Manage. 166, 267–275.

Salvadori I., Zuffardi P. (1973). Guida per l'escursione a Montevecchio e all'Arcuentu. Itinerari Geologici, Mineralogici e Giacimentologici in Sardegna, 1: 29-46.

Secchi F.A.G., Brotzu P., Callegari E. (1991). The Arburese igneous complex (SW Sardinia). An example of dominant igneous fractionation leading to peraluminous cordierite-bearing leucogranites as residual melts. Chem. Geol., 92(1-3): 213-249.

Shadid M. Dumat C. , Khalida S., Schreckb E., Xiongd T., Niazi N.K. (2017). Foliar heavy metal uptake, toxicity and detoxification in plants: A comparison of foliar and root metal uptake Journal of Hazardous Materials 325 36–58

Shuhe W. and Qixing Z. (2004). Identification of weed species with hyperaccumulative characteristics of heavy metals. Progress in Natural Science, 14(6), 495-503.

Stara P., Rizzo R., Tanca G.A. (1996). Iglesiente e Arburese. Miniere e Minerali, vol. 2, EMSA (Ed.) Cagliari

Sprocati A.,R., Alisi C., Pinto V., Montereali M.R. Marconi P. Tasso F., Turnau K., De Giudici G., Goralska K., Bevilacqua M., Marini F, Cremisini C. (2013).Assessment of the applicability of a "toolbox" designed for microbially assisted phytoremediation: the case studyat Ingurtosu mining site (Italy) Environ Sci Pollut Res. 2154-3

Wanty R.B., Podda F., De Giudici G. (2013) Zinc isotope and transition-element dynamics accompanying hydrozincite biomineralization in the Rio Naracauli, Sardinia, Italy. Chemical Geology 337–338

Weis JS, Weis P. (2004). Metal uptake, transport and release by wetland plants: implications for phytoremediation and restoration. Environment International 30, 685–700.

Weiss, D. J., Mason, T. F. D., Zhao, F. J., Kirk, G. J. D., Coles, B. J.and Horstwood, M. S. A. (2005). Isotopic discrimination of zinc inhigher plants. *New Phytologist,* 165: 703-710.

Weiss, D. J., Rausch, N., Mason, T. F. D., Coles, B. J., Wilkinson, J.J., Ukonmaanaho, L., Arnold, T. and Nieminen, T. M. (2007). Atmospheric deposition and isotope biogeochemistry of zinc in ombrotrophic peat. Geochimica et Cosmochimica Acta, 71: 3498-3517.

Tang Y.T., Cloquet C.,Deng T.H.B.,Sterckeman T, Echevarria,Yang W.J., Morel J.L.and Rong-Liang Qiu (2016). Zinc Isotope Fractionation in the Hyperaccumulator Noccaea caerulescens and the Nonaccumulating Plant Thlaspi arvense at Low and High Zn Supply Environ. Sci. Technol. 50, 8020−8027

Zeng X.W., Ma L. Q.,, Qiu R. L., Tang Y. T. (2011) Effects of Zn on plant tolerance and non-protein thiol accumulation in Zn hyperaccumulator Arabis paniculata Franch Environmental and Experimental Botany 70 227–232

Zhang J, Yin R, Lin X, Liu W, Chen R and Li X (2010). Interactive effect of biosurfactant and microorganism to enhance phytoremediation for removal of aged polycyclic aromatic hydrocarbons from contaminated soils.Journal of Health Science 56:257-266.

APPENDIX 1 *Geological data, ore deposit and mine activity of Naracauli*

In the Arburesethe main unit is represented by an allochthonous low-grade metamorphic complex made up of sedimentary and volcano-sedimentary successions, dating to Cambrian-Ordovician time (Carmignani et al. 1996). Arburese tectonic unit is part of the external nappe zone of the Variscan chain in south-western Sardinia, and was thrusted over the autochthonous successions of the Iglesiente complex during the Variscan orogeny. The Arburese igneous complex was emplaced, at the end of the orogeny (ca. 300 Ma). This igneous complex is characterized by a roughly concentric structure, with dominant granodiorite in the border zone, and leucogranite in the core (Secchi et al. 1991). The igneous complex is characterized by radial fractures filled by acid and basic magmatic dykes, and by quartz and metalliferous hydrothermal veins. The mineralized vein system of Montevecchio-Ingurtosu occurs in the northern side of the Arburese igneous complex; minor deposits occur in the southern edge. Post-Paleozoic formations include a Cenozoic sedimentary complex made up of sandy, conglomeratic, marly and carbonate facies (Carmignani et al. 1996), and the volcanic complex of Monte Arcuentu. The latter is made up of basaltic flows overlapped by breccias and pillow lavas (Assorgia et al. 1984), dating to Upper Oligocene-Lower Miocene. Aeolian dunes along the coast (Piscinasdunal complex) and fluvial deposits in the internal area constitute the Quaternary covers.

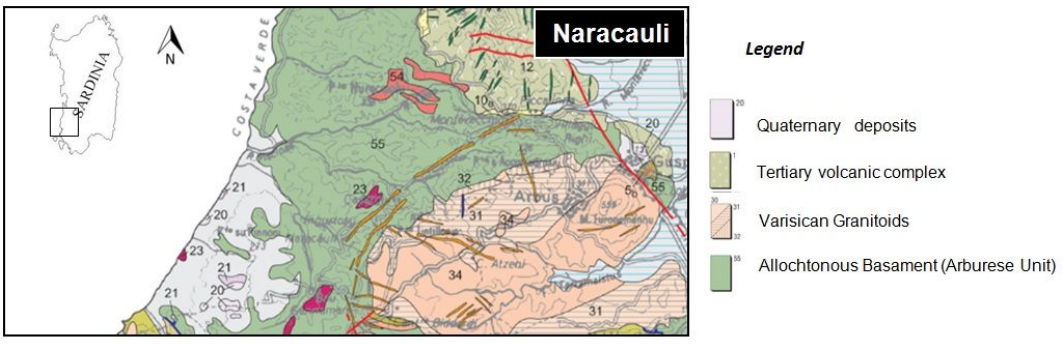

Figure A1. Geological map of Naracauli (mod Carmignani et al., 1996)

Ore deposits located in the Montevecchio-Ingurtosu district are attributable to the metamorphism and magmatism related to Varisican Orogeny.. These events had strong effects both as a promoter of the remoulding of pre-existing ore/mineral concentrations (by tectonic effects and/or by post-magmatic fluid circulation) and as a source of new ore and industrial minerals. Ore deposits are classified as hydrothermal base-metal and industrial-mineral veins, some of which were among the most important mining reserves of Sardinia (Marcello et al., 2004). The vein system extends in a NNE-SSW direction for at least 12 km. The vein bodies were mostly emplaced within the thermo-metamorphic aureole of the Variscan intrusion, but partly cut the intrusion itself (so-called radial veins). The main veins at Ingurtosu were the Brassey vein and the Ingurtosu vein. The Brassey vein was the most important both for its length (more than 2 km) and for the mineralization grade.

The main ore minerals were galena and sphalerite; chalcopyrite and pyrite were present in small amounts. Gangue minerals were quartz and Fe-bearing carbonates (ankerite and siderite; Cavinato et al., 1948). Other accessory minerals were greenockite, arsenopyrite, Ni- and Co-sulfides, sulfosalts, goethite, hematite, and cuprite (Stara et al., 1996). Calcite and dolomite were locally found in the gangue. Secondary minerals include smithsonite, cerussite, azurite, malachite, barite, anglesite, pyromorphite, and mimetite.

At Montevecchio-Ingurtosu, total tonnage was estimated at about 50-60 M tons of crude ore, grading 10-11 % combined Pb+Zn, 500-1,000 g Ag per ton of Pb, and 1,000 g of Cd per ton of Zn (Marcello et al., 2004). Metal production from the Montevecchio ores between 1848 and 1973 was 1.6×10^6 tons of Pb, 1.1×10^6 tons of Zn, and about 1×10^3 tons of Ag. By-products were Bi, Cd, Cu, Sb, and Ge (Salvadori et al., 1973). Currently, in Naracauli area there are 1.5 million cubic meters of open pit excavations, 2 million cubic meters of dump and 1 million cubic meters of tailings (RAS, 2003).

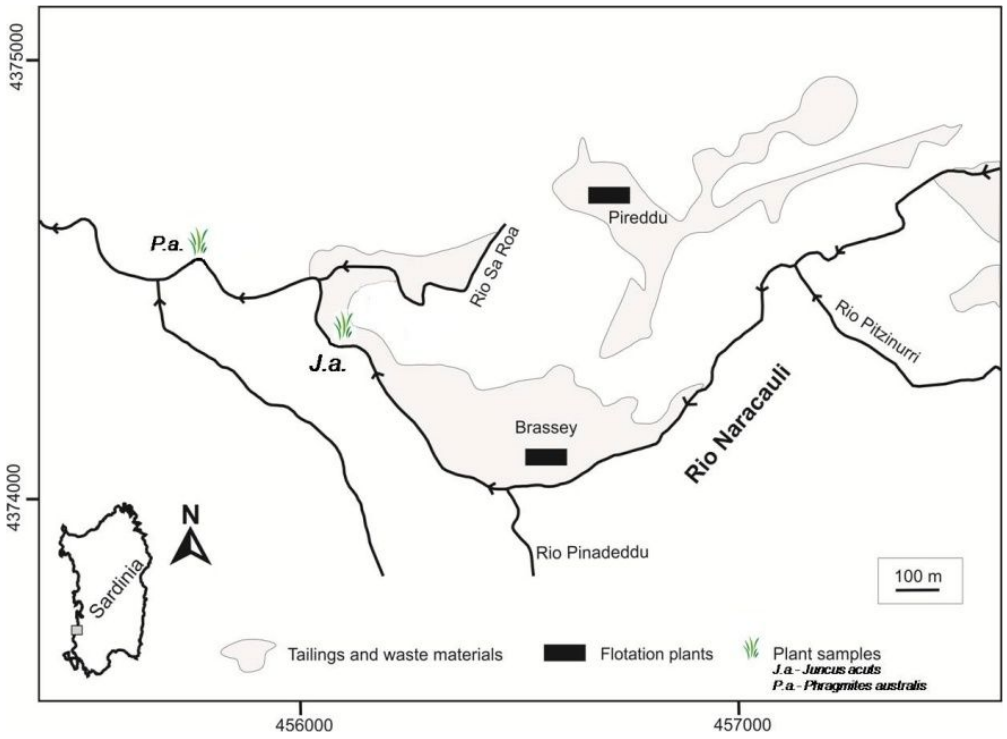

Figure A2.Map of Naracauli area showing the location of plant samples (J.a Juncus acutus, P.a Phragmites australis)

APPENDIX 2- *Diagrams of Cl, Na, Mn, Sr, B loadS (kg/day) in filtered samples (reach 1, from 0 m to 931 m; reach 2, from 931 m to 2312 m; reach 3, from 2312 m to 5577 m).*

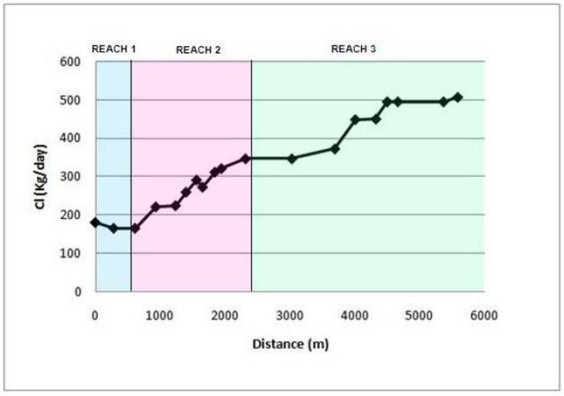

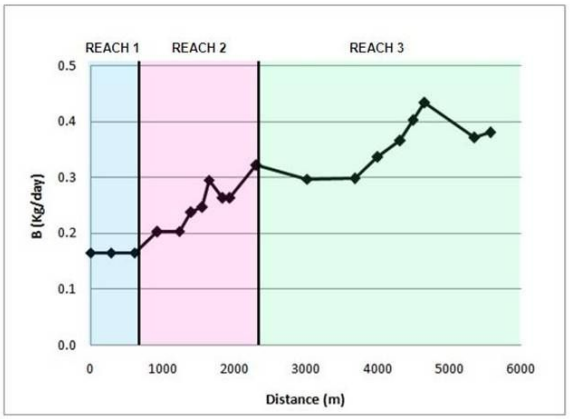

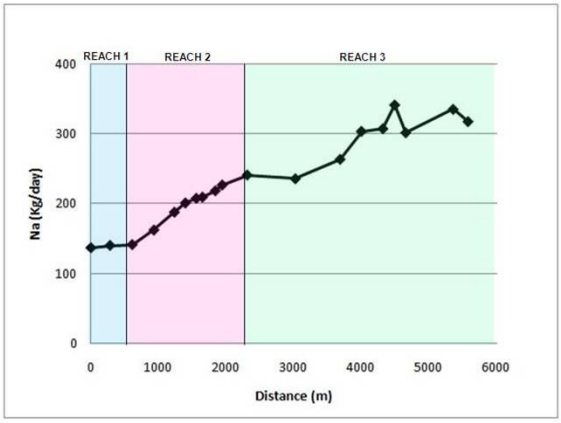

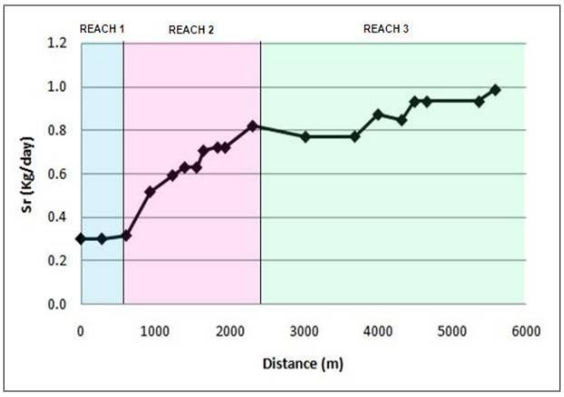

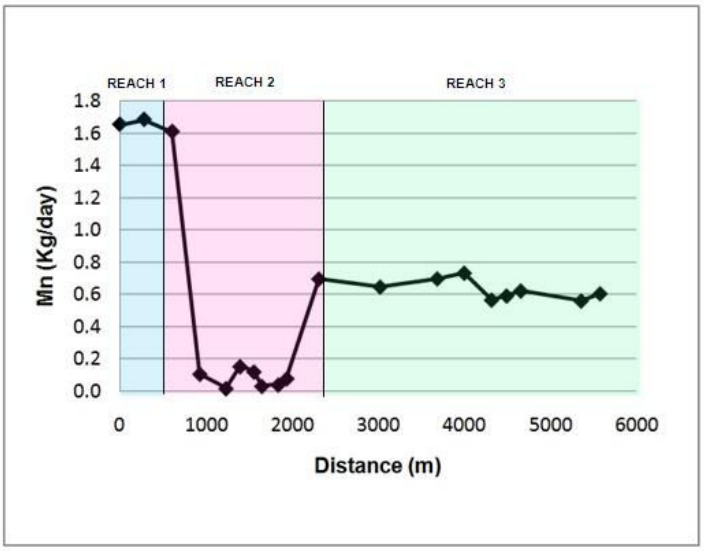

APPENDIX 3-*XRD analysis of layer of core samples GSP, SGA, SGB, SM*

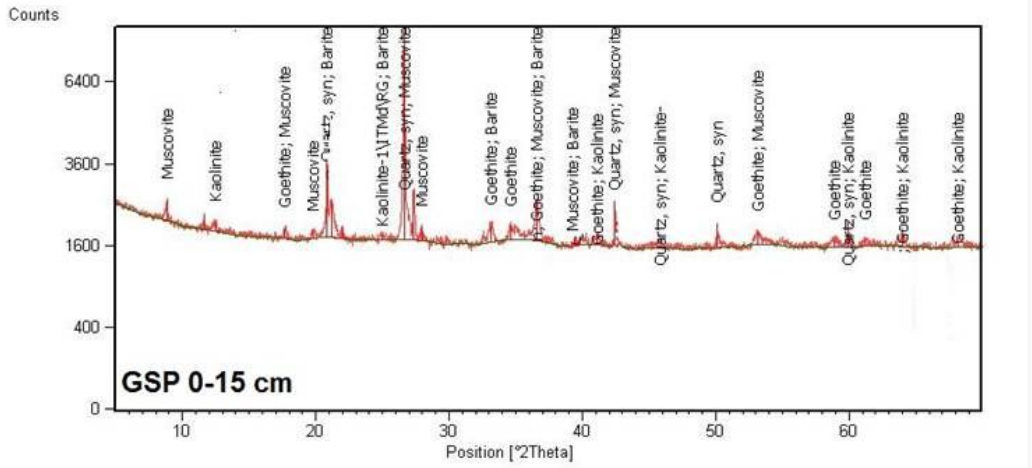

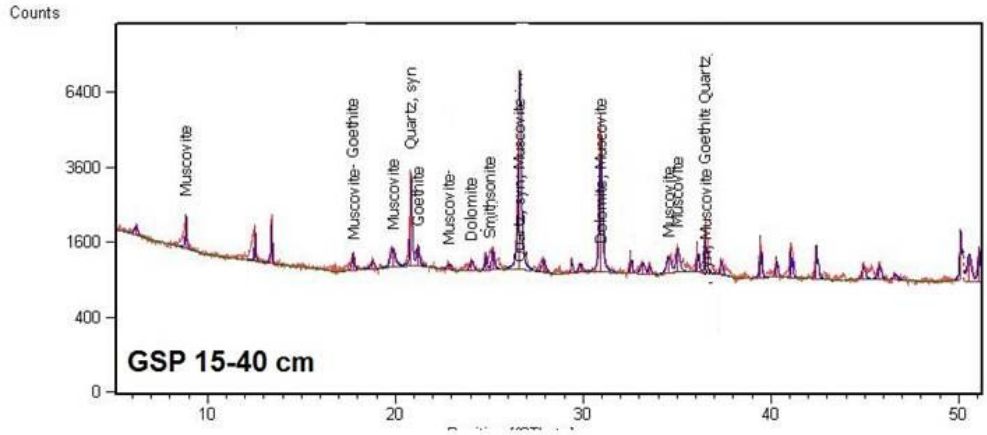

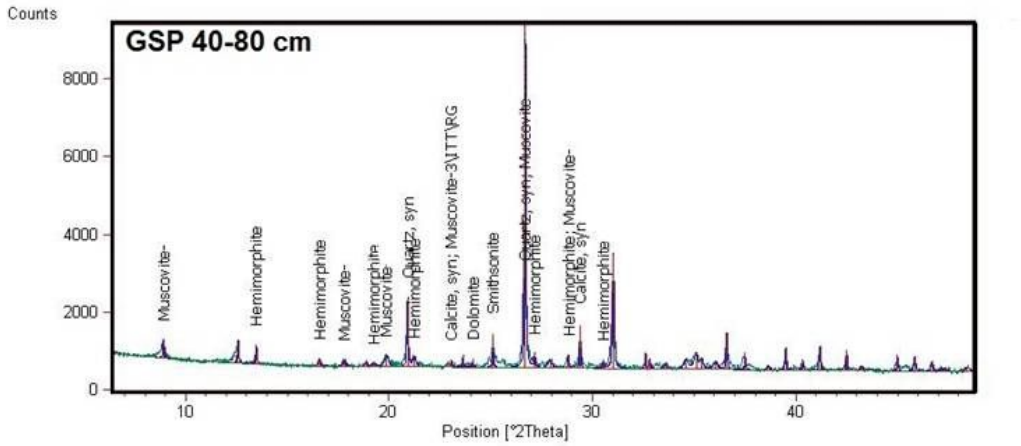

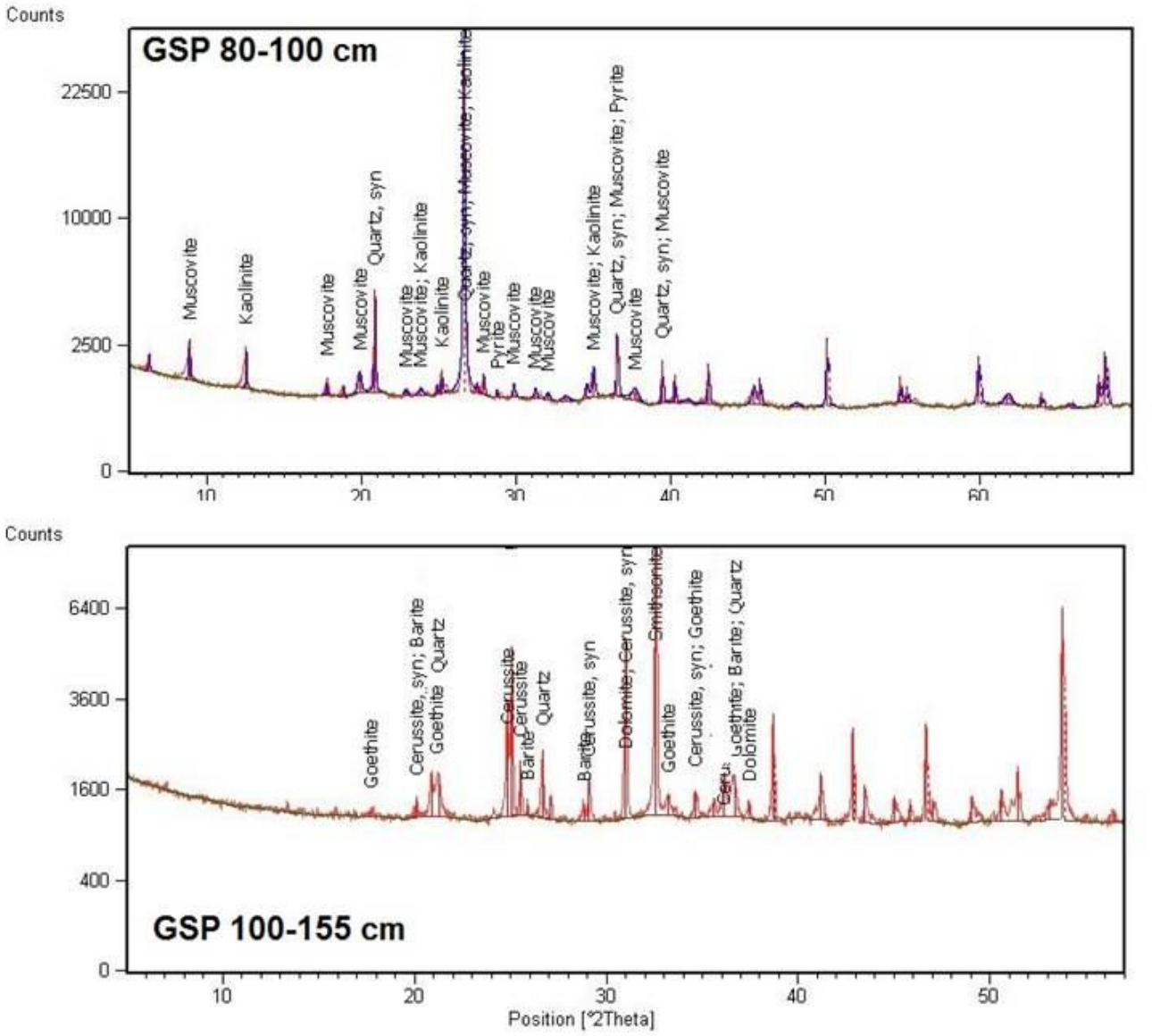
Counts
GSP 80-100 cm
22500
10000
2500
0
Muscovite
Kaolinite
Muscovite
Muscovite
Quartz, syn
Muscovite
Muscovite; Kaolinite
Kaolinite
Quartz, syn; Muscovite; Kaolinite
Muscovite
Pyrite
Muscovite
Muscovite
Muscovite
Muscovite; Kaolinite
Quartz, syn; Muscovite; Pyrite
Muscovite
Quartz, syn; Muscovite
10
20
30
40
50
60
Counts
6400
3600
1600
400
0
Goethite
Cerussite, syn; Barite
Goethite
Quartz
Cerussite
Cerussite
Barite
Quartz
Barite
Cerussite, syn
Dolomite; Cerussite, syn
Smithsonite
Goethite
Cerussite, syn; Goethite
Goethite; Barite; Quartz
Dolomite
GSP 100-155 cm
10
20
30
40
50
Position [°2Theta]

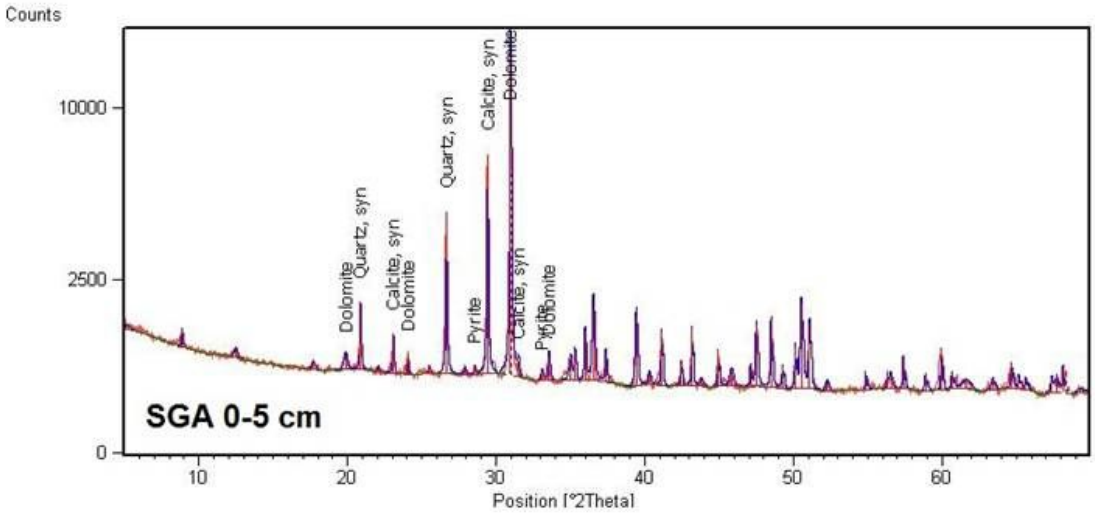
Counts
10000
2500
0
Dolomite
Quartz, syn
Calcite, syn
Dolomite
Quartz, syn
Pyrite
Calcite, syn
Dolomite
Pyrite
Dolomite
SGA 0-5 cm
10
20
30
40
50
60
Position [°2Theta]

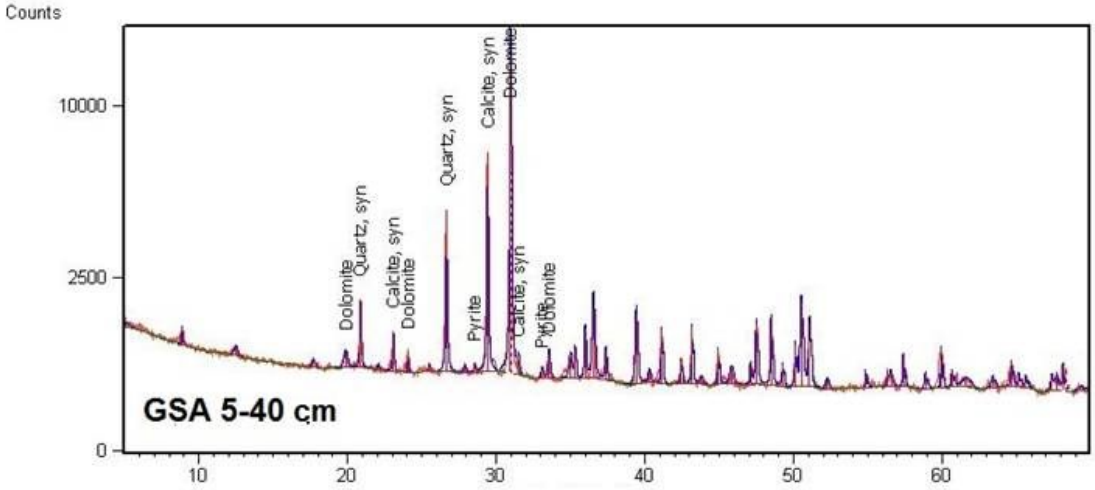
Counts
10000
2500
0
Dolomite
Quartz, syn
Calcite, syn
Dolomite
Quartz, syn
Pyrite
Calcite, syn
Dolomite
Pyrite
Dolomite
GSA 5-40 cm
10
20
30
40
50
60

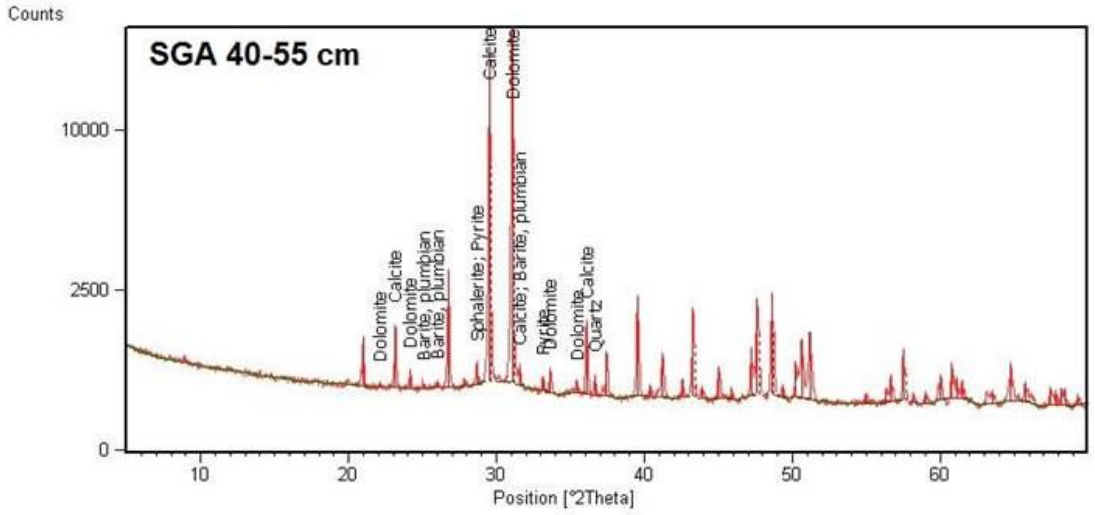
Counts
SGA 40-55 cm
10000
2500
0
Dolomite
Calcite
Dolomite
Barite, plumbian
Barite, plumbian
Sphalerite; Pyrite
Calcite
Dolomite
Calcite; Barite, plumbian
Pyrite
Dolomite
Dolomite
Calcite
Quartz
10
20
30
40
50
60
Position [°2Theta]

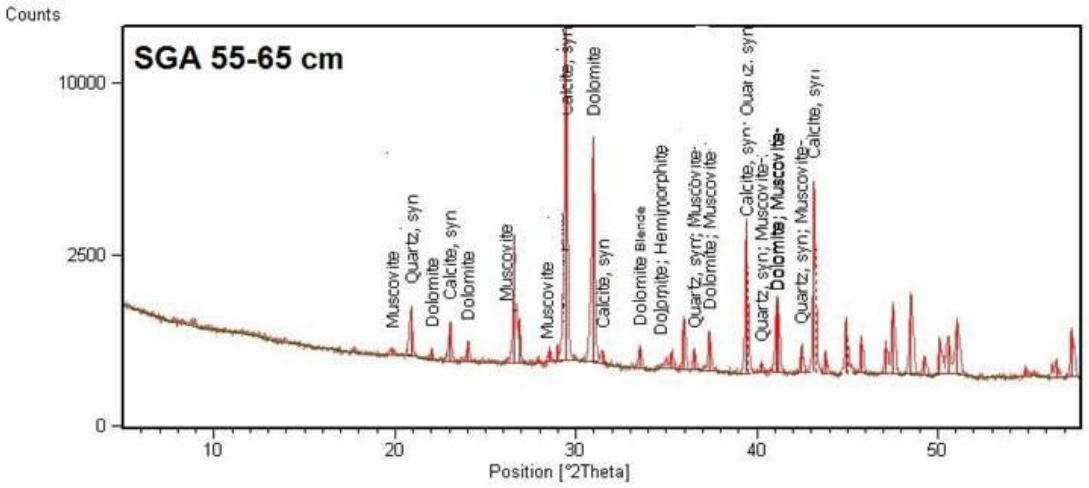
Counts
SGA 55-65 cm
10000
2500
0
10
20
30
40
50
Position [°2Theta]
Muscovite
Quartz, syn
Dolomite
Calcite, syn
Dolomite
Muscovite
Muscovite
Calcite, syn
Dolomite
Calcite, syn
Dolomite Blende
Dolomite; Hemimorphite
Quartz, syn; Muscovite
Dolomite; Muscovite
Calcite, syn; Quartz, syn
Quartz, syn; Muscovite
Dolomite; Muscovite
Quartz, syn; Muscovite
Calcite, syn

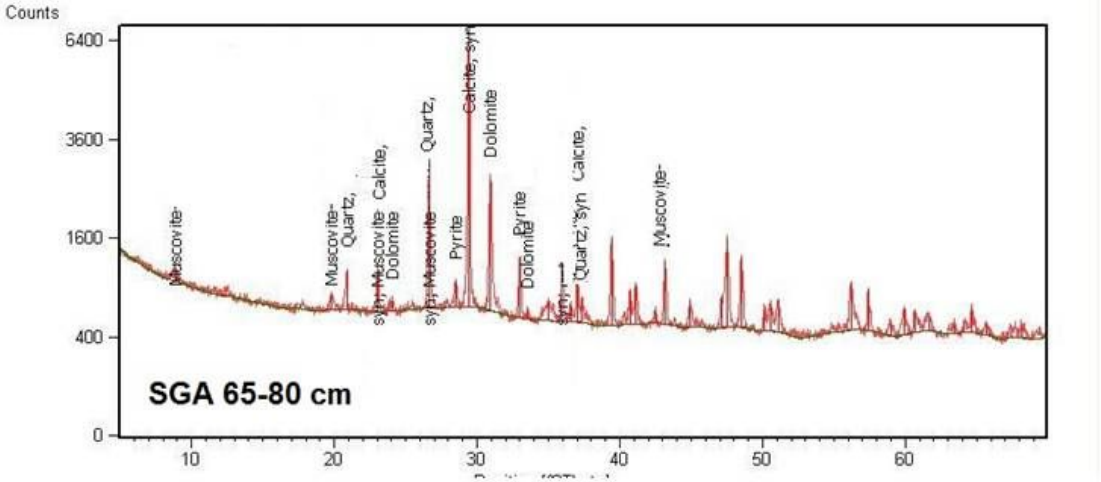
Counts
6400
3600
1600
400
0
SGA 65-80 cm
10
20
30
40
50
60
Muscovite
Muscovite
Quartz,
Calcite,
Muscovite
Dolomite
Quartz,
Muscovite
Calcite, syn
Dolomite
Pyrite
Pyrite
Dolomite
Quartz, syn
Calcite,
Muscovite

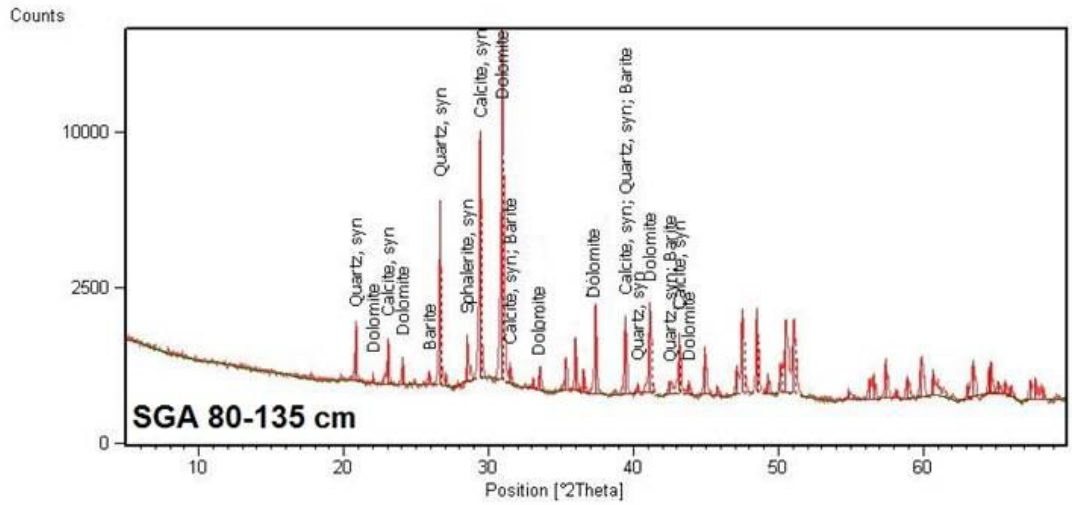
Counts
10000
2500
0
SGA 80-135 cm
10
20
30
40
50
60
Position [°2Theta]
Quartz, syn
Dolomite
Calcite, syn
Dolomite
Barite
Quartz, syn
Sphalerite, syn
Calcite, syn
Dolomite
Calcite, syn; Barite
Dolomite
Dolomite
Calcite, syn; Quartz, syn; Barite
Quartz, syn
Dolomite
Quartz, syn; Barite
Calcite, syn
Dolomite

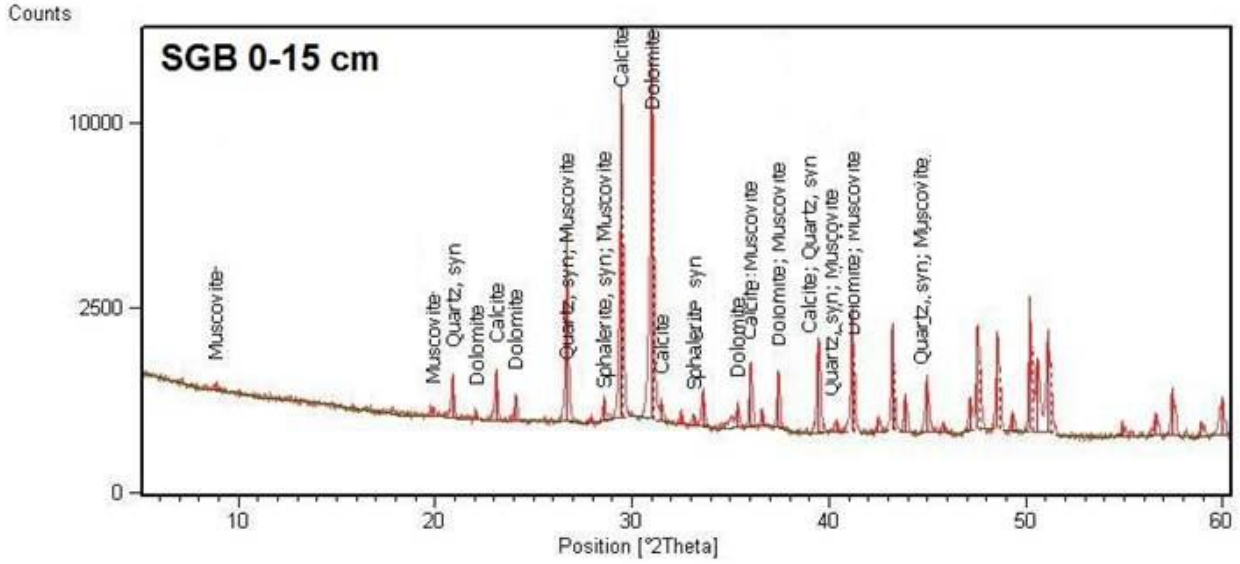
Counts
SGB 0-15 cm
10000
2500
0
Muscovite
Muscovite
Quartz, syn
Dolomite
Calcite
Dolomite
Quartz, syn; Muscovite
Sphalerite, syn; Muscovite
Calcite
Dolomite
Calcite
Sphalerite, syn
Dolomite
Calcite; Muscovite
Dolomite; Muscovite
Calcite; Quartz, syn
Quartz, syn; Muscovite
Dolomite; Muscovite
Quartz, syn; Muscovite
10
20
30
40
50
60
Position [°2Theta]

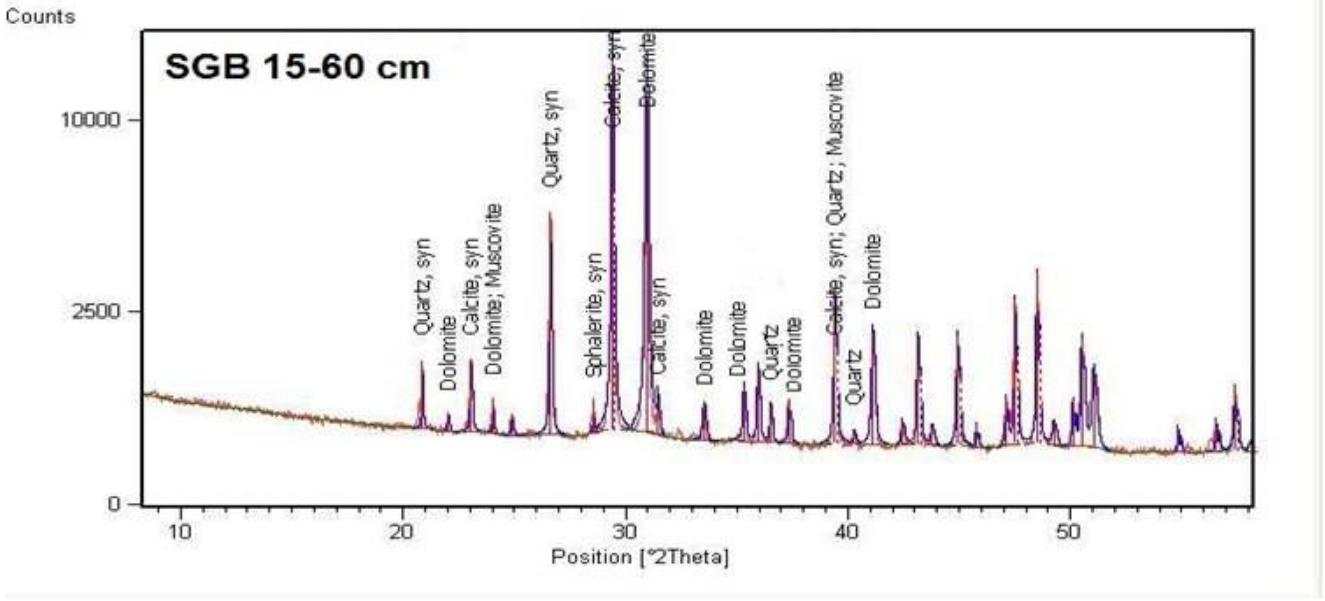
Counts
SGB 15-60 cm
10000
2500
0
Quartz, syn
Dolomite
Calcite, syn
Dolomite; Muscovite
Quartz, syn
Calcite, syn
Dolomite
Sphalerite, syn
Calcite, syn
Dolomite
Dolomite
Quartz
Dolomite
Calcite, syn; Quartz; Muscovite
Quartz
Dolomite
10
20
30
40
50
Position [°2Theta]

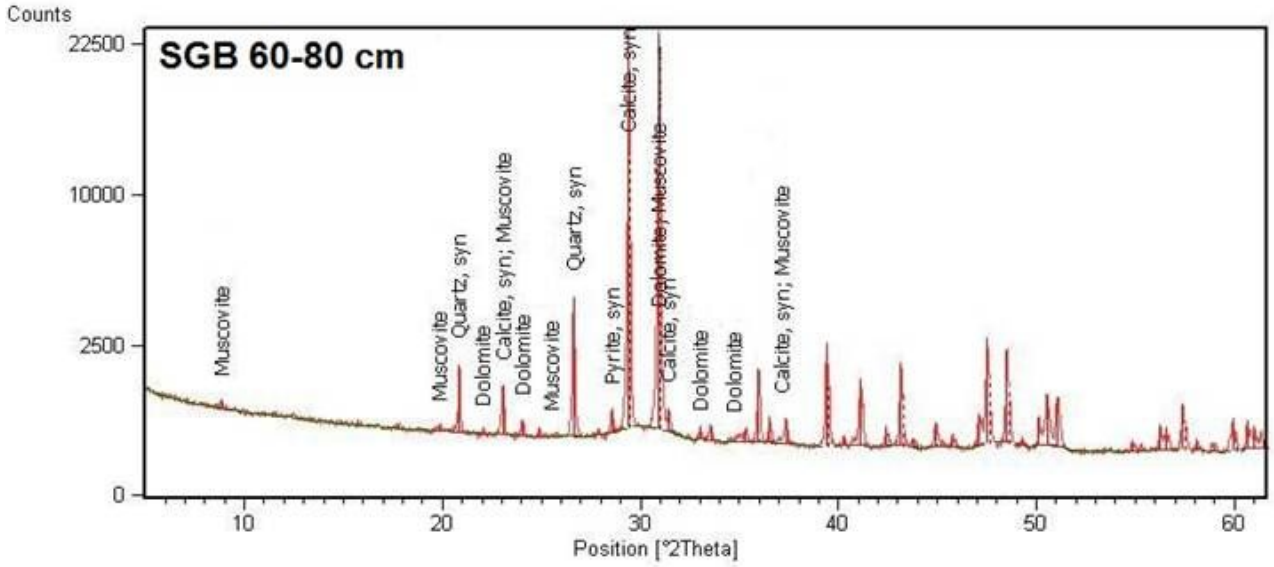
Counts
SGB 60-80 cm
22500
10000
2500
0
Muscovite
Muscovite
Quartz, syn
Dolomite
Calcite, syn; Muscovite
Dolomite
Muscovite
Quartz, syn
Pyrite, syn
Calcite, syn
Dolomite; Muscovite
Calcite, syn
Dolomite
Dolomite
Calcite, syn; Muscovite
10
20
30
40
50
60
Position [°2Theta]

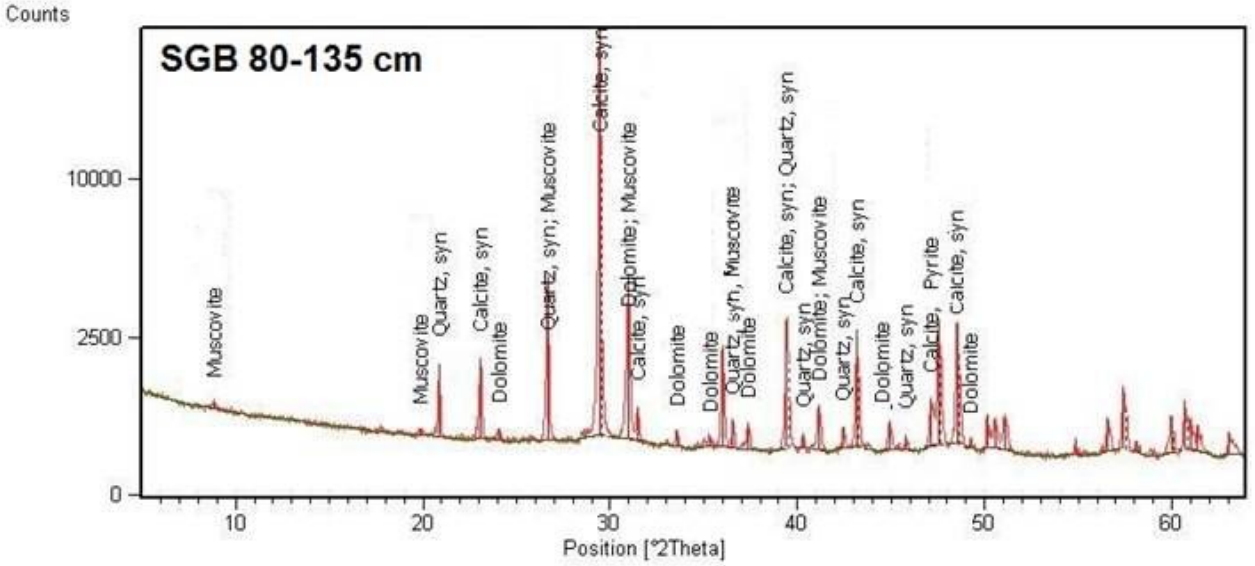
Counts
SGB 80-135 cm
10000
2500
0
Muscovite
Muscovite
Quartz, syn
Calcite, syn
Dolomite
Quartz, syn; Muscovite
Calcite, syn
Dolomite; Muscovite
Calcite, syn
Dolomite
Dolomite
Quartz, syn; Muscovite
Dolomite
Calcite, syn; Quartz, syn
Quartz, syn
Dolomite; Muscovite
Quartz, syn
Calcite, syn
Dolomite
Quartz, syn
Pyrite
Calcite,
Calcite, syn
Dolomite
10
20
30
40
50
60
Position [°2Theta]

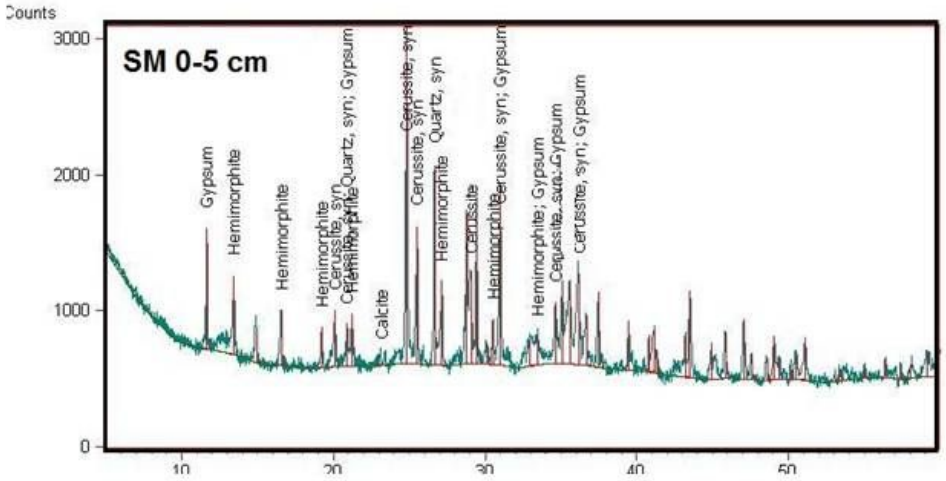
Counts
SM 0-5 cm
Gypsum
Hemimorphite
Hemimorphite
Hemimorphite
Cerussite, syn
Quartz, syn; Gypsum
Calcite
Cerussite, syn
Quartz, syn
Hemimorphite
Cerussite
Hemimorphite
Cerussite, syn; Gypsum
Hemimorphite; Gypsum
Cerussite, syn; Gypsum

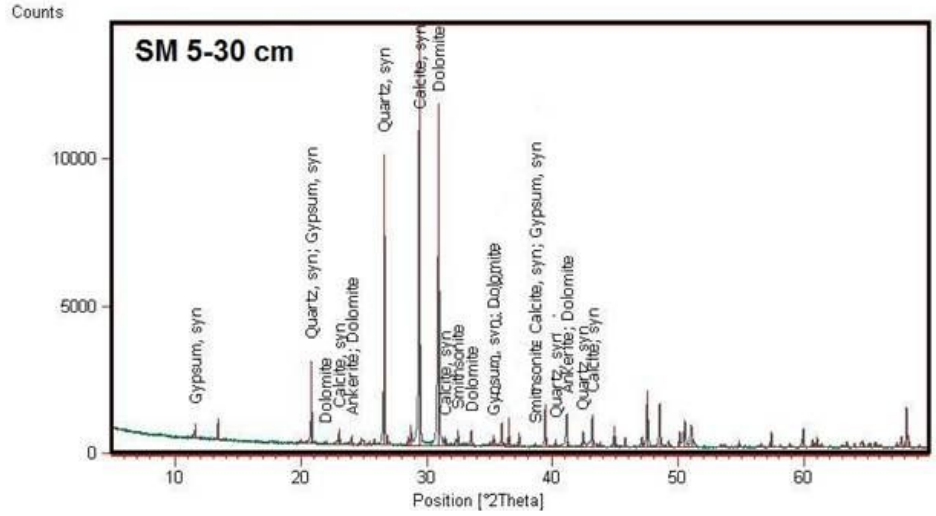
Counts
SM 5-30 cm
Gypsum, syn
Quartz, syn; Gypsum, syn
Dolomite
Calcite, syn
Ankerite; Dolomite
Quartz, syn
Calcite, syn
Dolomite
Smithsonite
Dolomite
Gypsum, syn; Dolomite
Smithsonite
Calcite, syn; Gypsum, syn
Quartz, syn
Ankerite; Dolomite
Quartz, syn
Calcite, syn
Position [°2Theta]

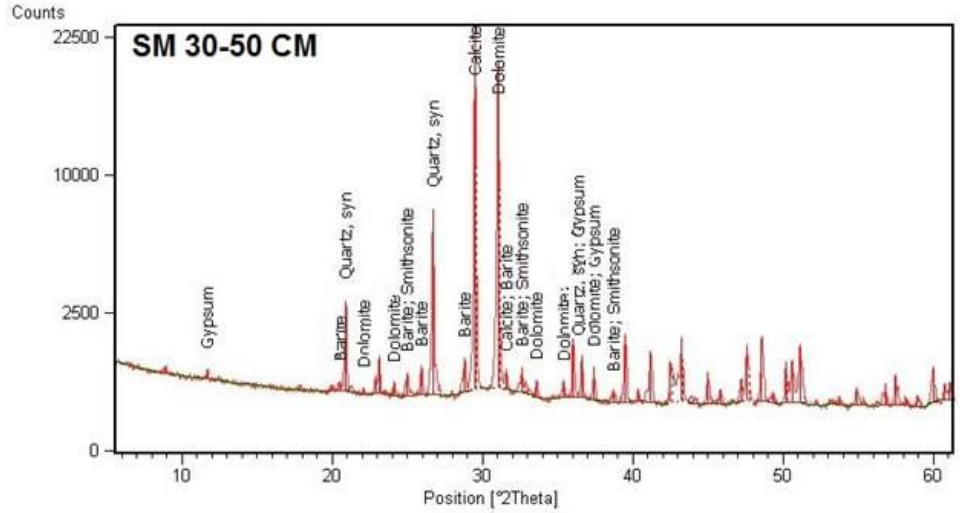
Counts
SM 30-50 CM
Gypsum
Barite
Quartz, syn
Dolomite
Dolomite
Barite; Smithsonite
Barite
Quartz, syn
Barite
Calcite
Dolomite
Calcite; Barite
Barite; Smithsonite
Dolomite
Dolomite; Quartz, syn; Gypsum
Dolomite; Gypsum
Barite; Smithsonite
Position [°2Theta]

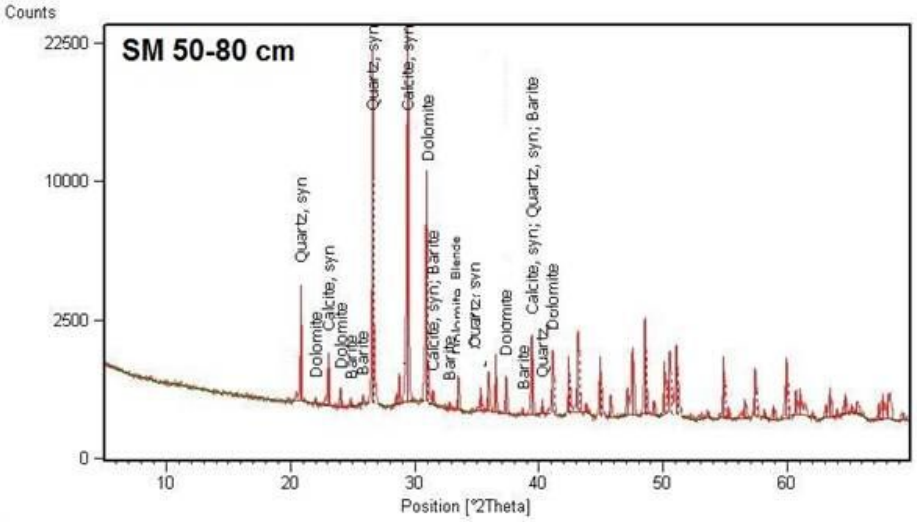
Counts
SM 50-80 cm
Position [°2Theta]

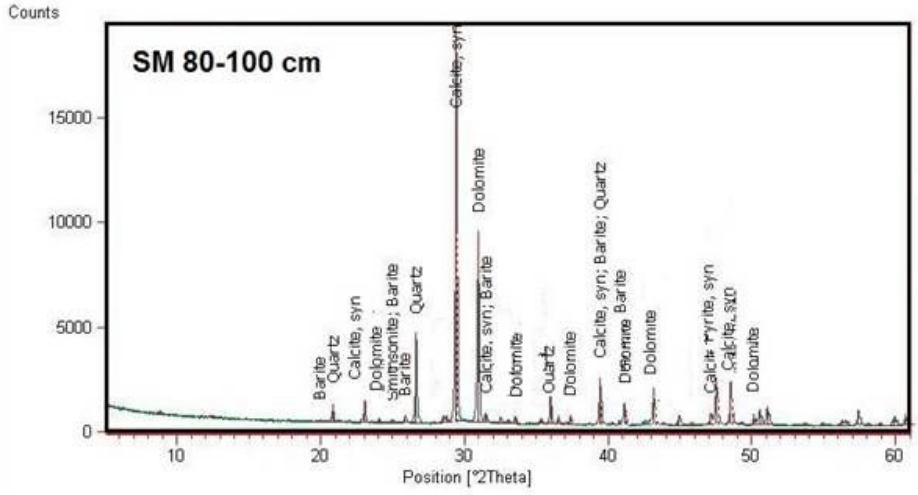
Counts
SM 80-100 cm
Position [°2Theta]

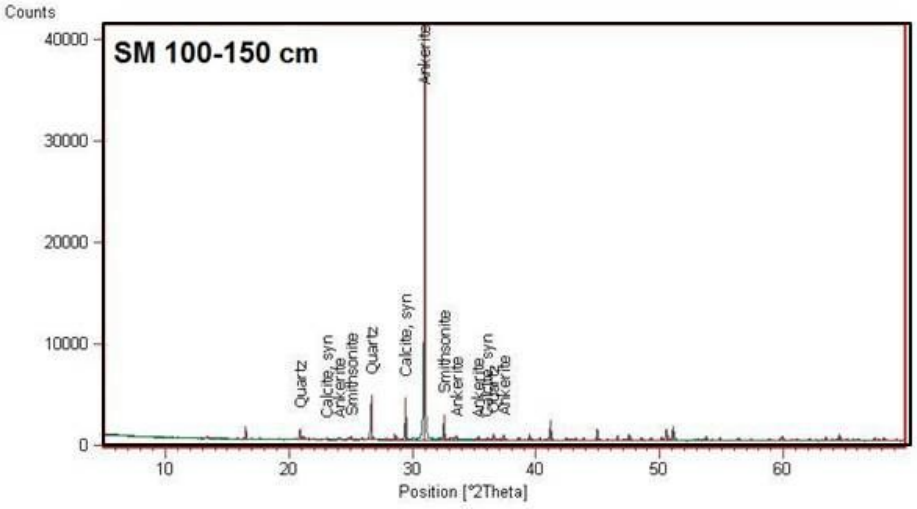
Counts
SM 100-150 cm
Position [°2Theta]

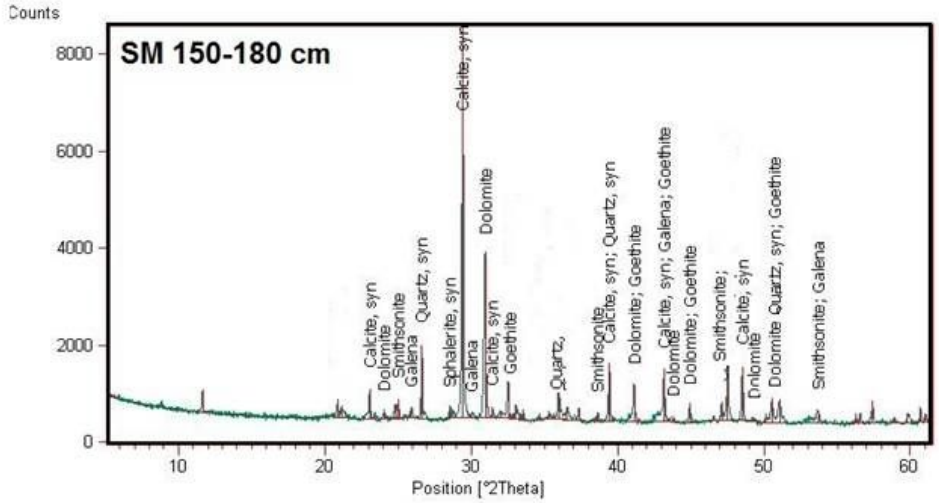
Counts
SM 150-180 cm
Calcite, syn
Dolomite
Smithsonite
Galena
Quartz, syn
Sphalerite, syn
Galena
Calcite, syn
Goethite
Dolomite
Quartz,
Smithsonite
Calcite, syn; Quartz, syn
Dolomite; Goethite
Calcite, syn; Galena; Goethite
Dolomite; Goethite
Smithsonite;
Calcite, syn
Dolomite
Dolomite
Quartz, syn; Goethite
Smithsonite; Galena
Position [°2Theta]

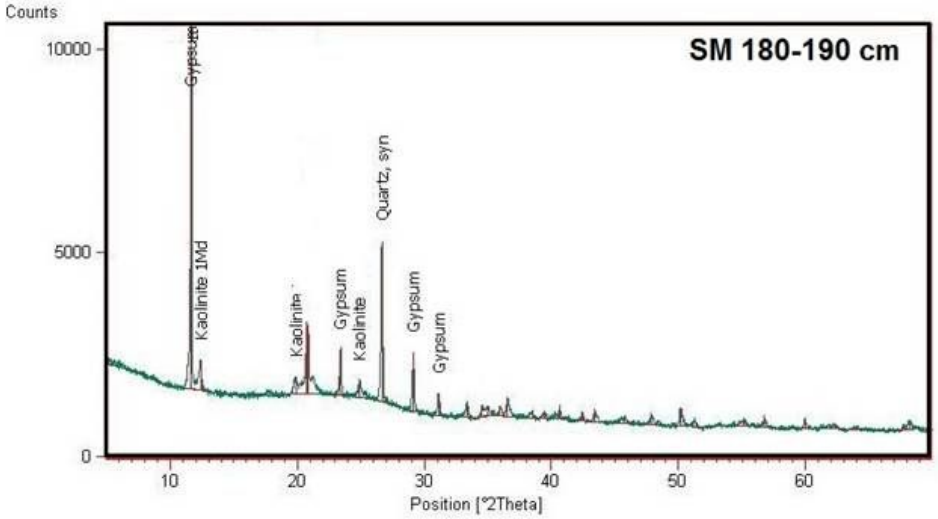
Counts
SM 180-190 cm
Kaolinite 1Md
Kaolinite
Gypsum
Kaolinite
Quartz, syn
Gypsum
Gypsum
Position [°2Theta]

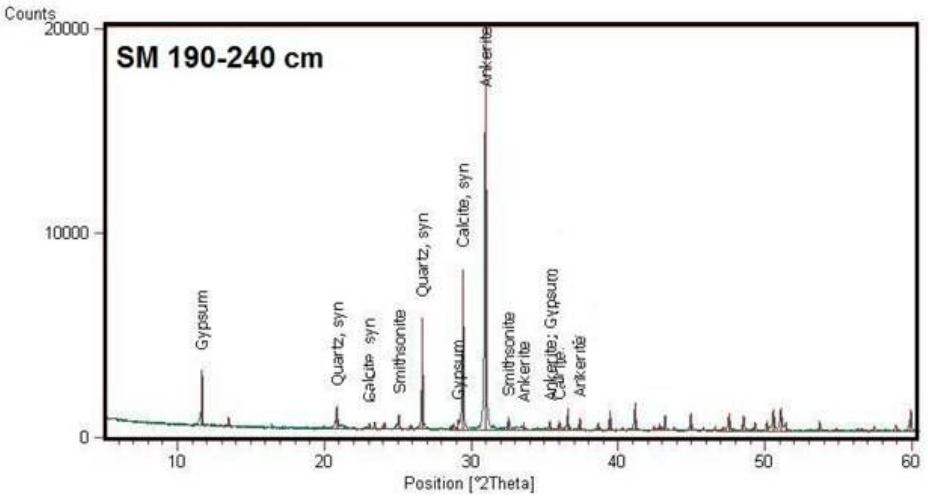
Counts
SM 190-240 cm
Gypsum
Quartz, syn
Smithsonite
Quartz, syn
Gypsum
Calcite, syn
Smithsonite
Ankerite
Ankerite
Position [°2Theta]

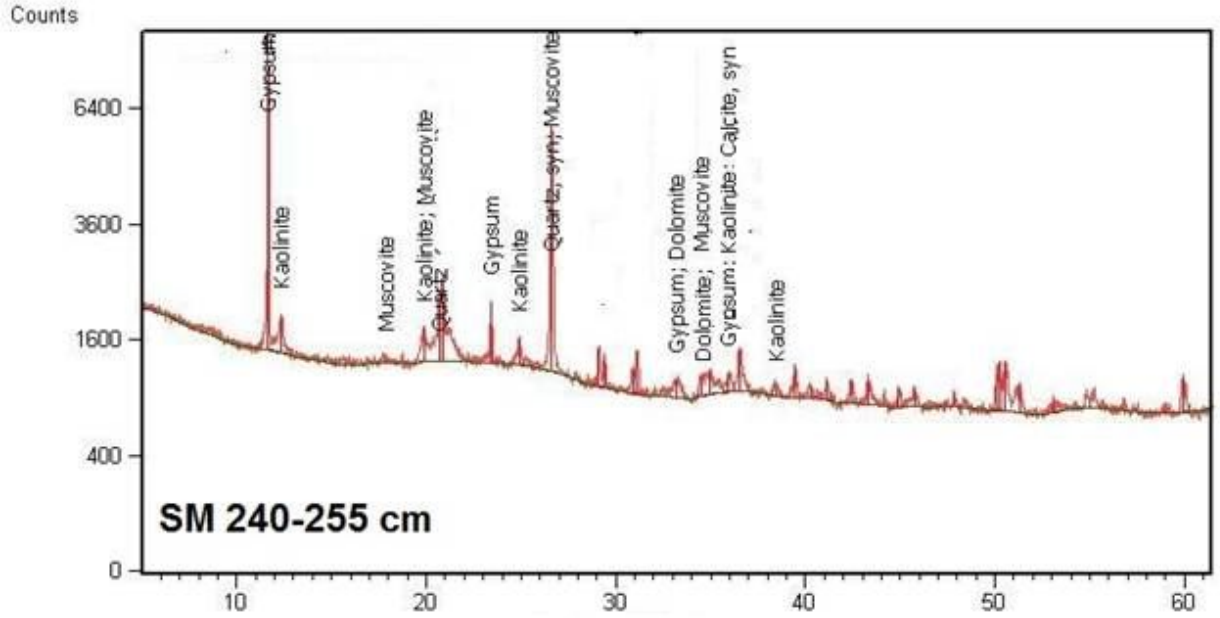
Counts
6400
3600
1600
400
0
Kaolinite
Muscovite
Kaolinite; Muscovite
Gypsum
Kaolinite
Gypsum; Dolomite
Dolomite; Muscovite
Gypsum; Kaolinite; Calcite, syn
Kaolinite
SM 240-255 cm
10
20
30
40
50
60

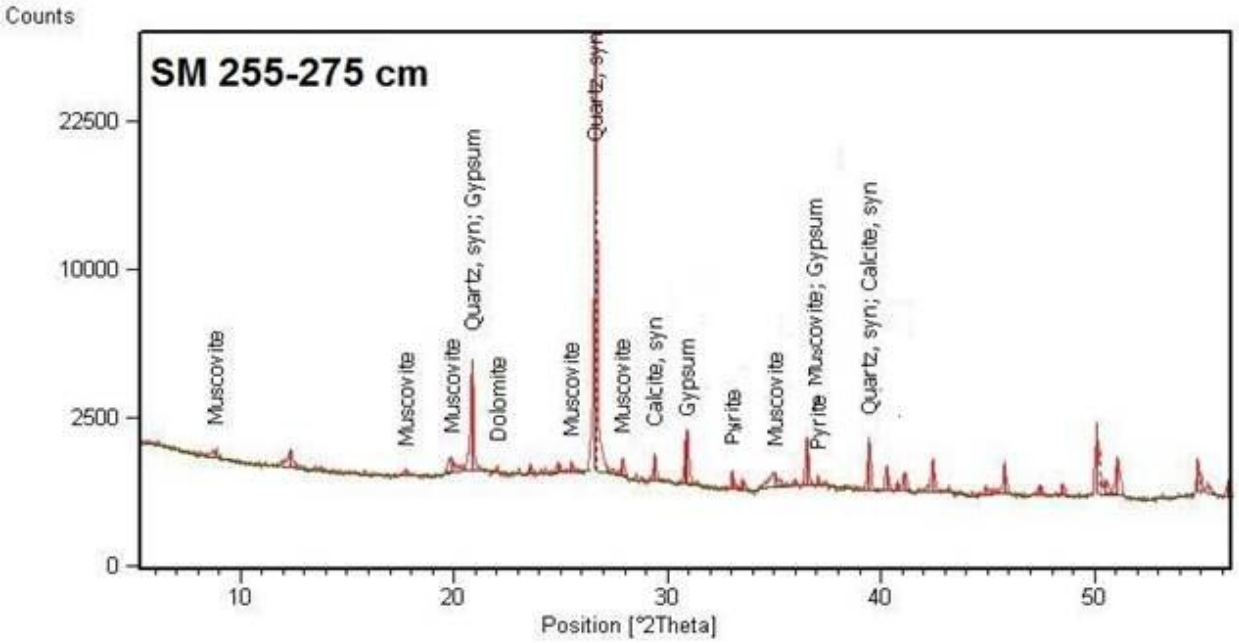
Counts
SM 255-275 cm
22500
10000
2500
0
Muscovite
Muscovite
Muscovite
Quartz, syn; Gypsum
Dolomite
Muscovite
Quartz, syn
Muscovite
Calcite, syn
Gypsum
Pyrite
Muscovite
Pyrite; Muscovite; Gypsum
Quartz, syn; Calcite, syn
10
20
30
40
50
Position [°2Theta]

APPENDIX 4-*SEM images of framboidal pyrite in core samples*

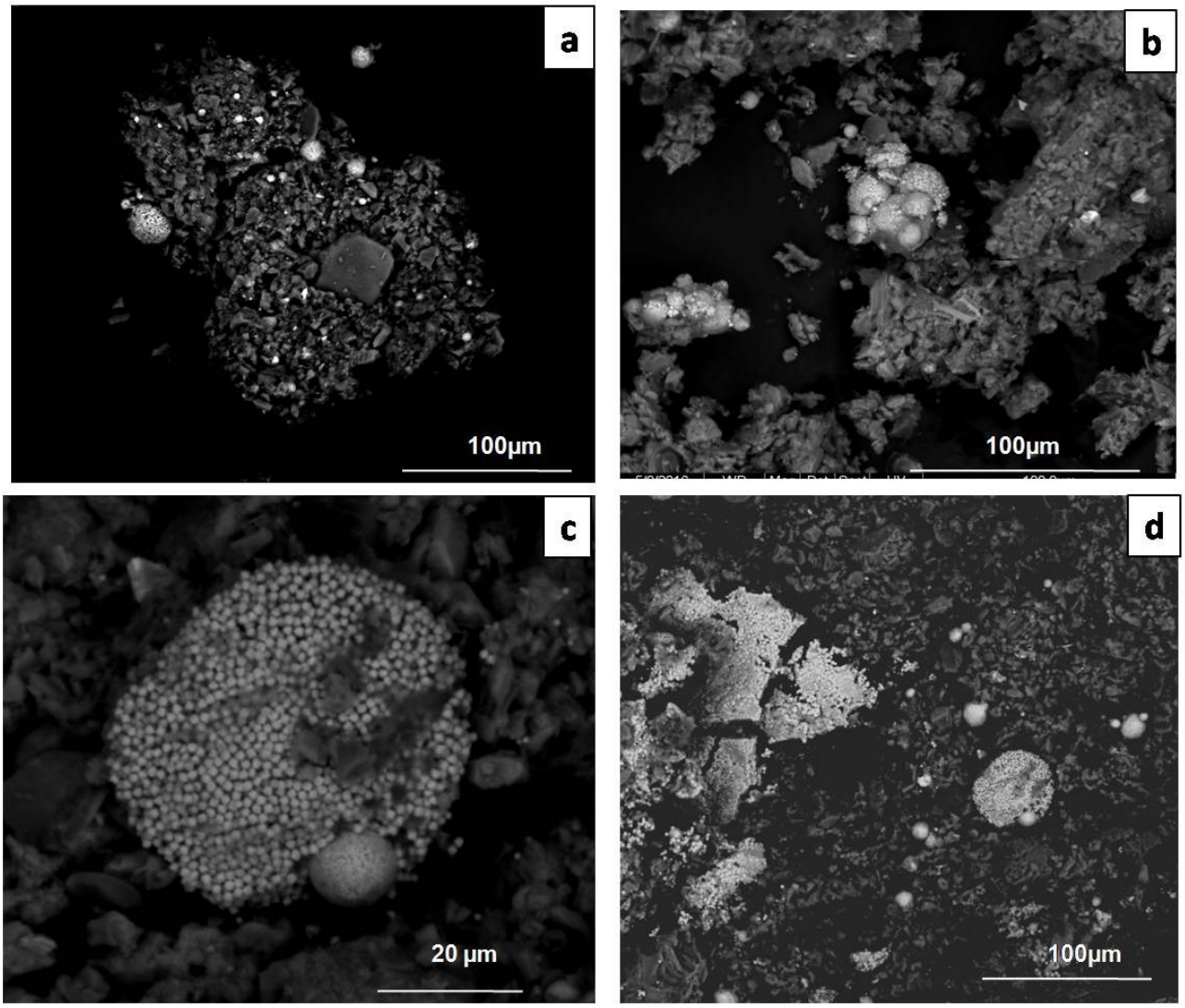

APPENDIX 5- *Heigh t(cm) of plants in Line A(polluted line) an Line B (unpolluted line)*

Line A	**May**	**June**	**July**	**August**	**September**
Juncus a. **and Unpolluted Substrate**	10	21	24	26	27
Juncus a. **and Sa Masa Substrate**	6.5	10.5	11.5	13	16
Juncus a. **and Naracauli Substrate**	8	10.5	11	11	12
Phragmites a. **and Unpolluted Substrate**	13.5	39	60	73.5	90
Phragmites a. **and Sa Masa Substrate**	15.5	23	32	40	51
Line B	**May**	**June**	**July**	**August**	**September**
Juncus a. **and Unpolluted Substrate**	8	19	19	27	27
Juncus a. **and Sa Masa Substrate**	6	12	12	17	18.5
Juncus a. **and Naracauli Substrate**	6.5	9.5	10	10.5	12
Phragmites a. **and Unpolluted Substrate**	15	58	65.5	70	73
Phragmites a. **and Sa Masa Substrate**	15	25	29	29	29

APPENDIX 6- *Concentration of Zn in substrates, in Juncus acutus and Phragmites australis within experimental error in brackets.*

Concentration of Zn in substrate Line A (polluted line) before and after experiment

	Before	***After***
	(ppm)	
***Juncus a.* and Unpolluted Substrate**	137 (±4)	3040 (±91)
***Juncus a.* and Sa Masa Substrate**	20390 (±610)	20620 (±618)
***Juncus a.* and Naracauli Substrate**	9715 (±290)	12490 (±375)
***Phragmites a.* and Unpolluted Substrate**	137 (±4)	3200 (±96)
***Phragmites a.* and Sa Masa Substrate**	20390 (±610)	20450 (±614)

Concentration of Zn in substrate Line B(unpolluted line) before and after experiment

	Before	***After***
	(ppm)	
***Juncus a.* and Unpolluted Substrate**	137 (±4)	169 (±6)
***Juncus a.* and Sa Masa Substrate**	20390 (±610)	19550 (±587)
***Juncus a.* and Naracauli Substrate**	9715 (±290)	10450(±314)
***Phragmites a.* and Unpolluted Substrate**	137 (±4)	145(±4)
***Phragmites a.* and Sa Masa Substrate**	20390 (±610)	19510(±587)

. Concentration of Zn in Juncusacutus	***Stems***	***Roots***
	(ppm)	(ppm)
Juncus a., Unpolluted Substrate, Polluted Water	62 (±2)	123(±4)
Juncus a., Unpolluted Substrate, Unpolluted Water	41(±1)	59(±2)
Juncus a., Sa Masa Substrate, Polluted Water	1140(±34)	9960(±299)
Juncus a., Sa Masa Substrate, Unpolluted Water	872(±26)	5890(±178)
Juncus a., Naracauli Substrate, Polluted Water	480(±14)	4670(±140)
Juncus a., Naracauli Substrate, Unpolluted Water	423(±13)	4400(±132)

Concentration of Zn in Phragmites australis	***Leaves***	***Stems***	***Roots***
	(ppm)	(ppm)	(ppm)
Phragmites a., Unpolluted Substrate, Polluted Water	49(±1)	126(±4)	210(±6)
Phragmites a., Unpolluted Substrate, Unpolluted Water	20(±6)	32(±1)	57(±2)
Phragmites a., Sa Masa Substrate, Polluted Water	1200(±36)	1240(±38)	4110(±123)
Phragmites a., Sa Masa Substrate, Unpolluted Water	1340(±40)	1350(±41)	1560(±47)

APPENDIX 7. *Mineralogical composition of all substrates.*

Substrate	***Mineralogical composition***
Unpolluted Substrates	*quartz, calcite, albite, muscovite, gypsum*
Juncus a., Unpolluted Substrate, Polluted Water	*quartz, calcite, albite, muscovite, gypsum*
Juncus a., Unpolluted Substrate, Unpolluted Water	*quartz, calcite, albite, muscovite, gypsum*
Phragmites a., Unpolluted Substrate, Polluted Water	*quartz, calcite, albite, muscovite, gypsum*
Phragmites a., Unpolluted Substrate, Unpolluted Water	*quartz, calcite, albite, muscovite, gypsum*
Sa Masa Substrates	*quartz, dolomite, calcite, hemimorphite, barite, smithsonite*
Juncus a., Sa Masa Substrate, Polluted Water	*quartz, dolomite, calcite, hemimorphite, barite, smithsonite*
Juncus a., Sa Masa Substrate, Unpolluted Water	*quartz, dolomite, calcite, hemimorphite, barite, smithsonite*
Phragmites a., Sa Masa Substrate, Polluted Water	*quartz, dolomite, calcite, hemimorphite, barite, smithsonite*
Phragmites a., Sa Masa Substrate, Unpolluted Water	*quartz, dolomite, calcite, hemimorphite, barite, smithsonite*
Naracauli Substrates	*quartz, calcite, muscovite, gypsum, hemimorphite, siderite, hydrozincite*
Juncus a., Naracauli Substrate, Polluted Water	*quartz, calcite, muscovite, gypsum, hemimorphite, siderite, hydrozincite*
Juncus a., Naracauli Substrate, Unpolluted Water	*quartz, calcite, muscovite, gypsum, hemimorphite, siderite, hydrozincite*

APPENDIX 8- STXM *Distribution of Zn, Si, AL and Fe in external surface of root of Phragmites australis*

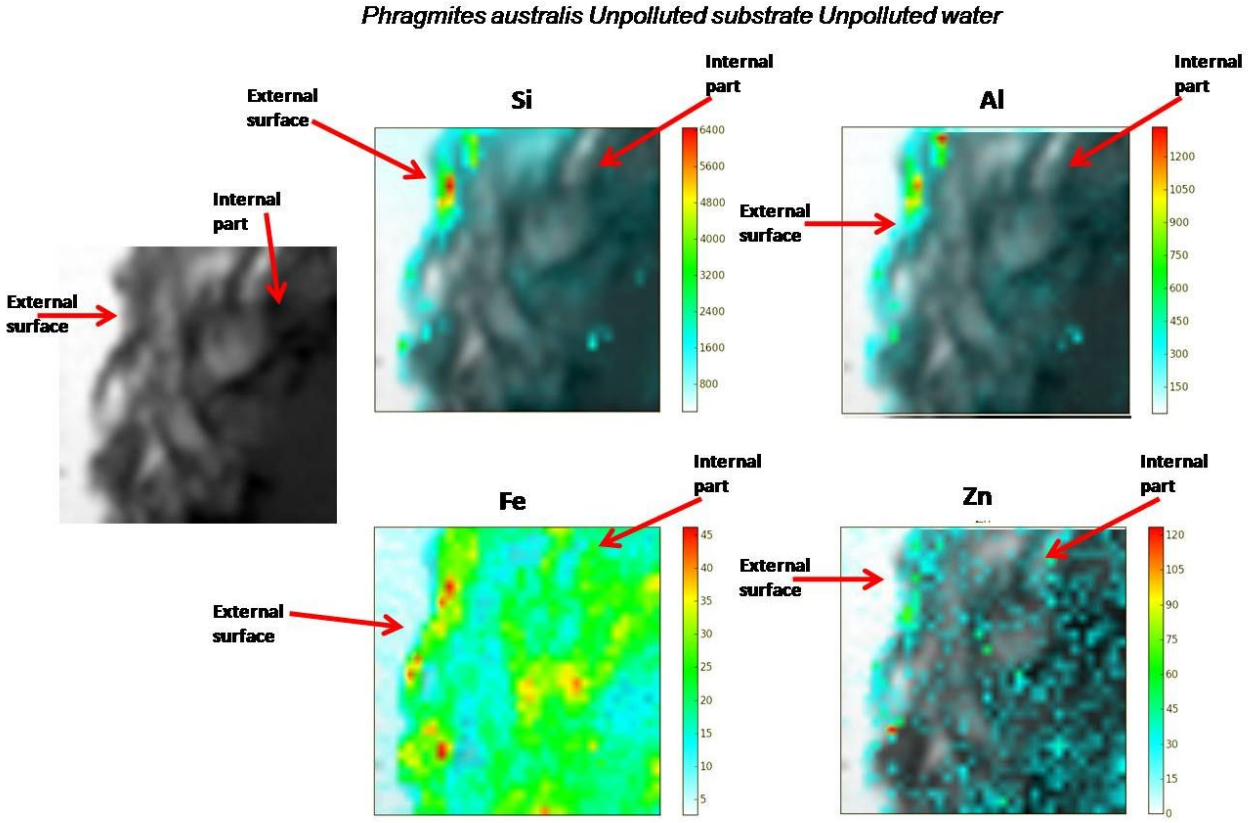

APPENDIX 9 - *XRD analysis of substrate of rhizoboxes*

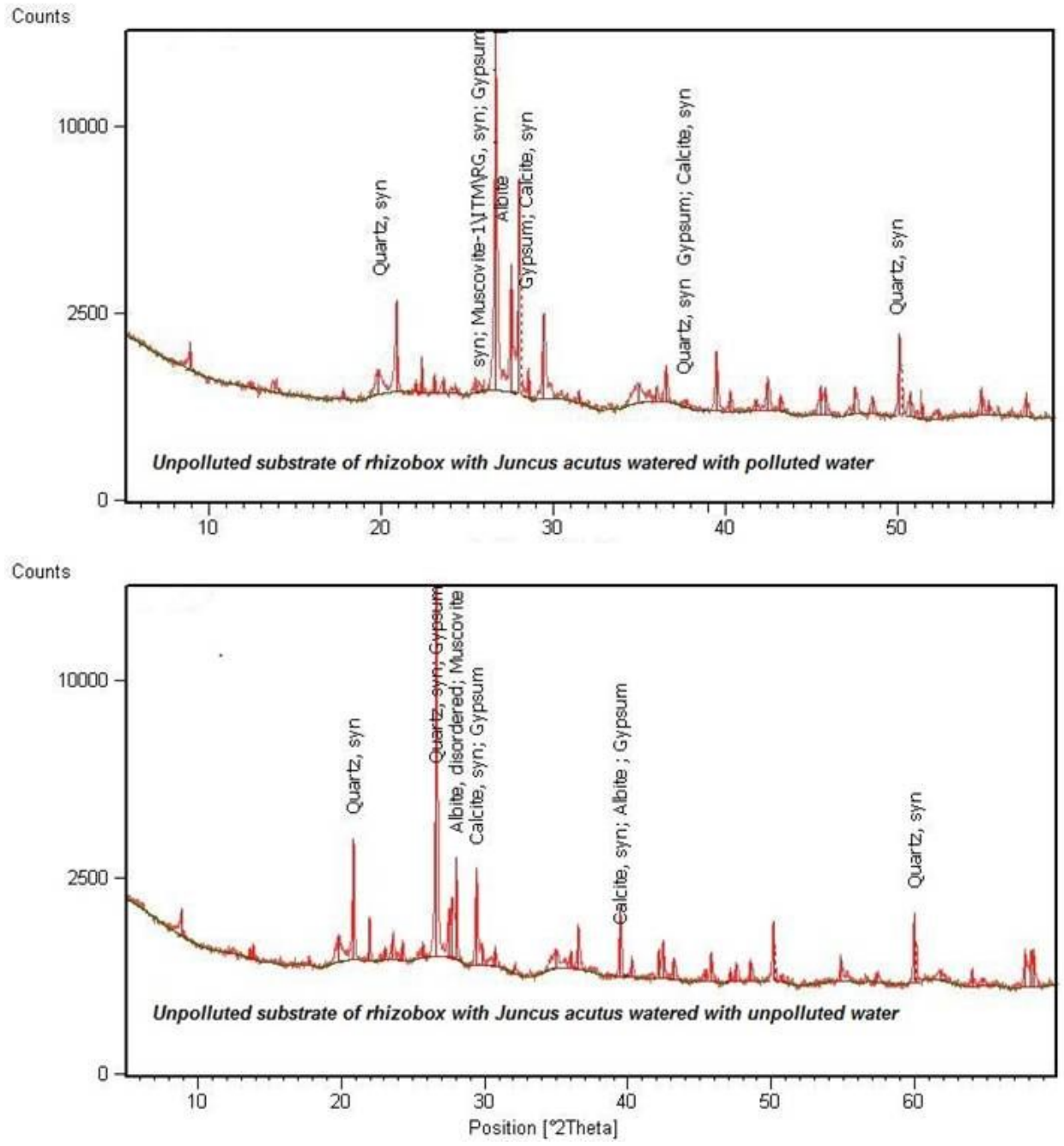

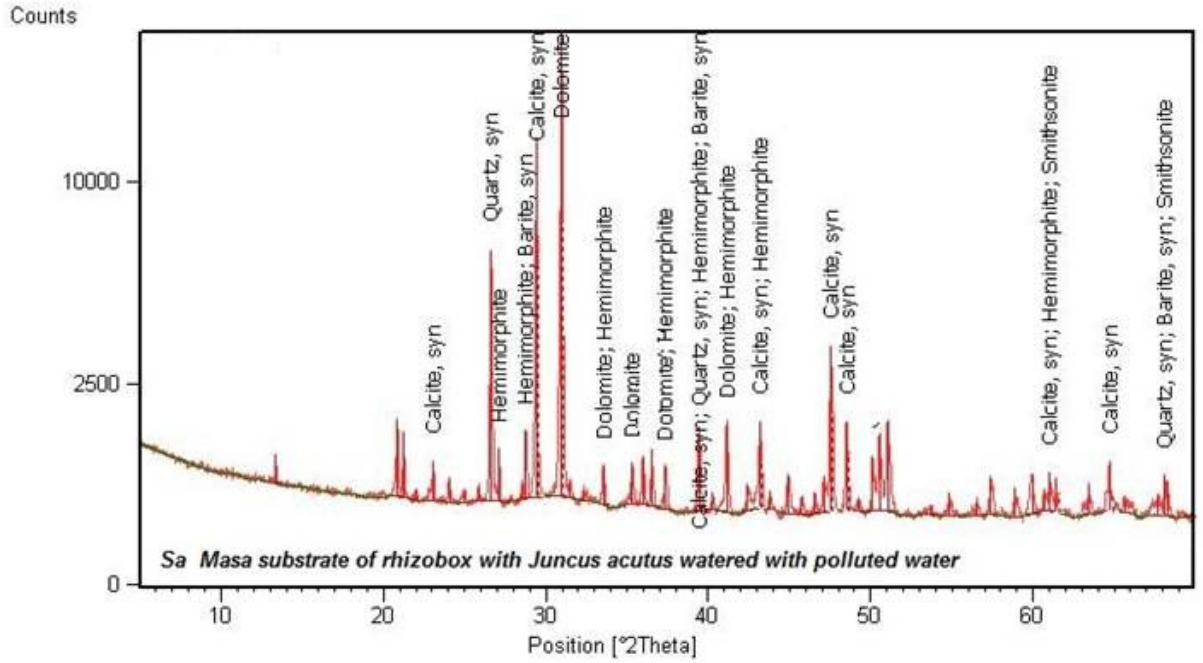
Counts
10000
2500
0
Quartz, syn
Calcite, syn
Dolomite
Hemimorphite
Hemimorphite; Barite, syn
Dolomite; Hemimorphite
Dolomite; Hemimorphite
Calcite, syn; Quartz, syn; Hemimorphite; Barite, syn
Dolomite; Hemimorphite
Calcite, syn; Hemimorphite
Calcite, syn
Calcite, syn
Calcite, syn; Hemimorphite; Smithsonite
Calcite, syn
Quartz, syn; Barite, syn; Smithsonite
Sa Masa substrate of rhizobox with Juncus acutus watered with polluted water
10
20
30
40
50
60
Position [°2Theta]

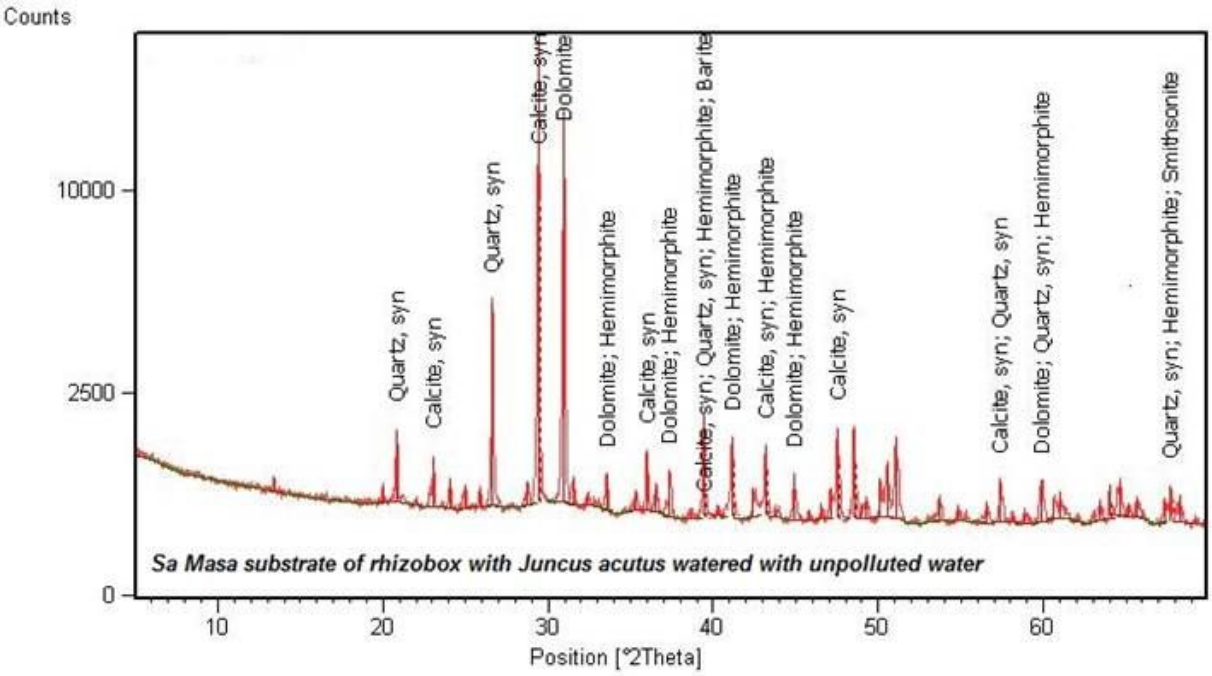
Counts
10000
2500
0
Quartz, syn
Calcite, syn
Quartz, syn
Calcite, syn
Dolomite
Dolomite; Hemimorphite
Calcite, syn
Dolomite; Hemimorphite
Calcite, syn; Quartz, syn; Hemimorphite; Barite
Dolomite; Hemimorphite
Calcite, syn; Hemimorphite
Dolomite; Hemimorphite
Calcite, syn
Calcite, syn; Quartz, syn
Dolomite; Quartz, syn; Hemimorphite
Quartz, syn; Hemimorphite; Smithsonite
Sa Masa substrate of rhizobox with Juncus acutus watered with unpolluted water
10
20
30
40
50
60
Position [°2Theta]

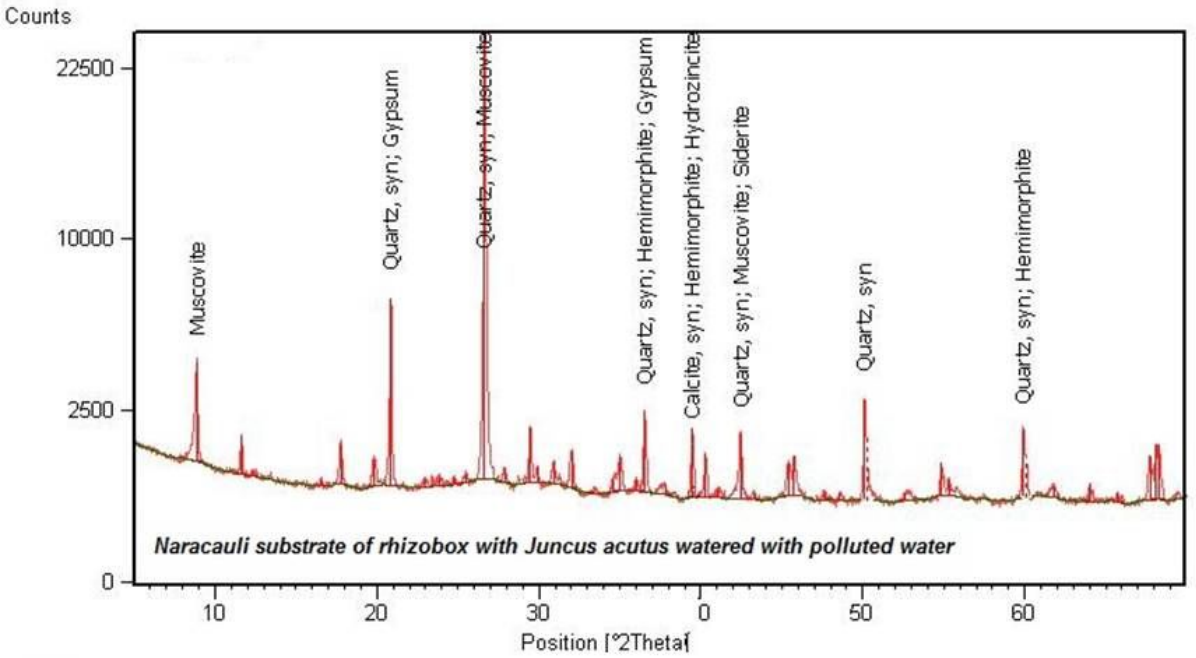
Counts
22500
10000
2500
0
Muscovite
Quartz, syn; Gypsum
Quartz, syn; Muscovite
Quartz, syn; Hemimorphite; Gypsum
Calcite, syn; Hemimorphite; Hydrozincite
Quartz, syn; Muscovite; Siderite
Quartz, syn
Quartz, syn; Hemimorphite
Naracauli substrate of rhizobox with Juncus acutus watered with polluted water
10
20
30
0
50
60
Position [°2Theta]

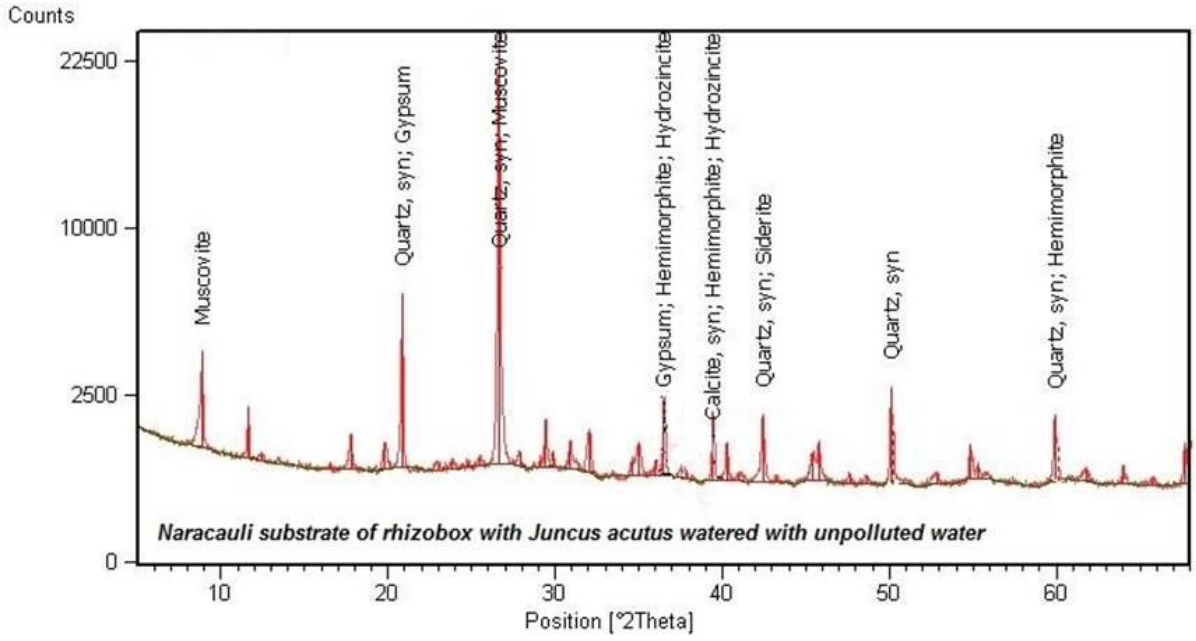
Counts
22500
10000
2500
0
Muscovite
Quartz, syn; Gypsum
Quartz, syn; Muscovite
Gypsum; Hemimorphite; Hydrozincite
Calcite, syn; Hemimorphite; Hydrozincite
Quartz, syn; Siderite
Quartz, syn
Quartz, syn; Hemimorphite
Naracauli substrate of rhizobox with Juncus acutus watered with unpolluted water
10
20
30
40
50
60
Position [°2Theta]

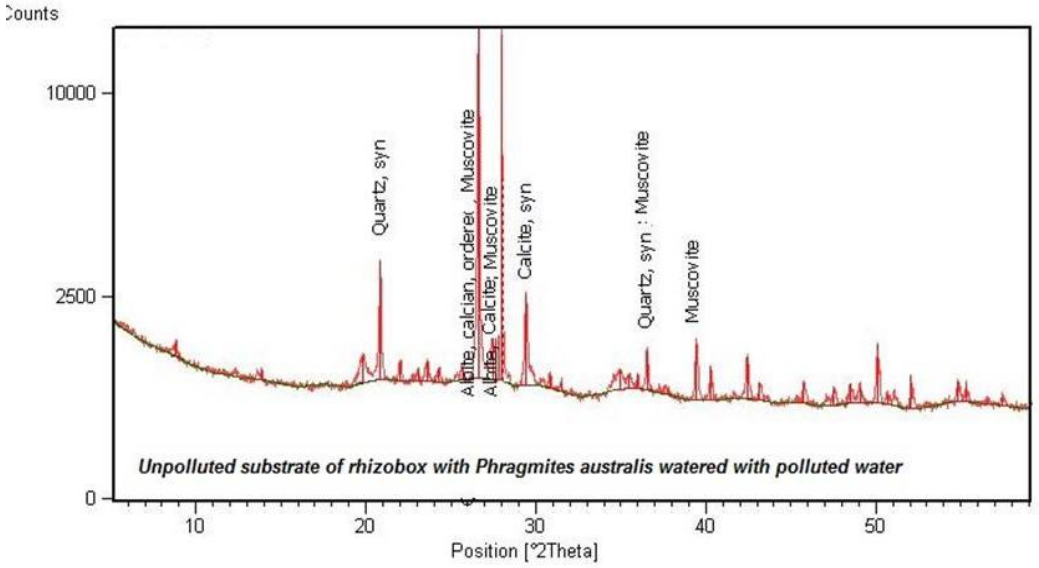
Counts
10000
2500
0
Quartz, syn
Albite, calcian, ordered; Muscovite
Albite; Calcite; Muscovite
Calcite, syn
Quartz, syn; Muscovite
Muscovite
Unpolluted substrate of rhizobox with Phragmites australis watered with polluted water
10
20
30
40
50
Position [°2Theta]

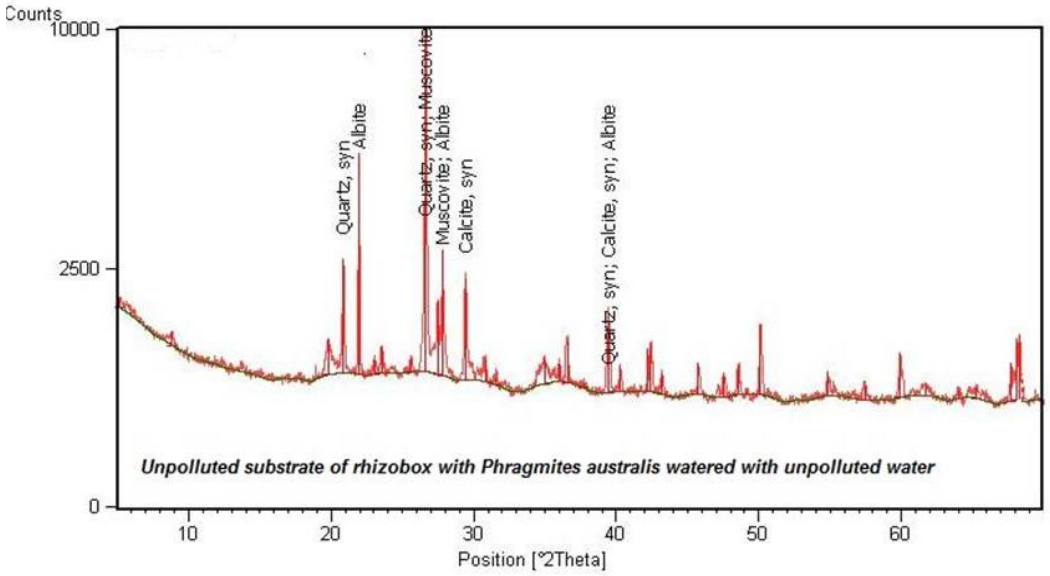
Counts
10000
2500
0
Quartz, syn
Albite
Quartz, syn; Muscovite
Muscovite; Albite
Calcite, syn
Quartz, syn; Calcite, syn; Albite
Unpolluted substrate of rhizobox with Phragmites australis watered with unpolluted water
10
20
30
40
50
60
Position [°2Theta]

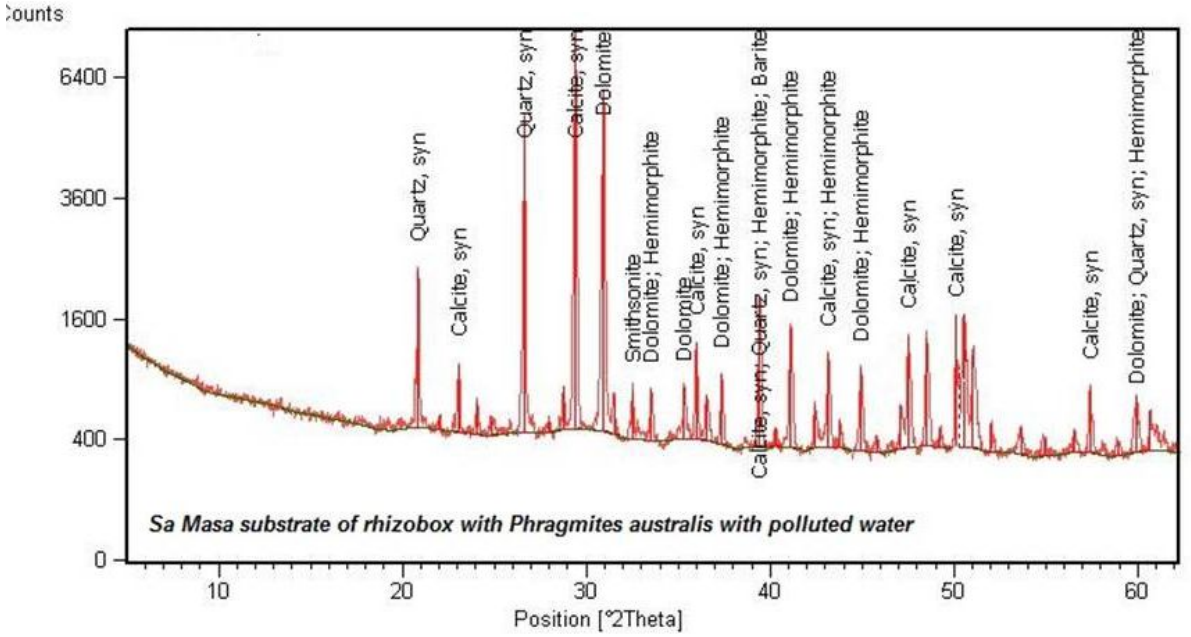
Counts
6400
3600
1600
400
0
Quartz, syn
Calcite, syn
Quartz, syn
Calcite, syn
Dolomite
Smithsonite
Dolomite; Hemimorphite
Dolomite
Calcite, syn
Dolomite; Hemimorphite
Calcite, syn; Quartz, syn; Hemimorphite; Barite
Dolomite; Hemimorphite
Calcite, syn; Hemimorphite
Dolomite; Hemimorphite
Calcite, syn
Calcite, syn
Calcite, syn
Dolomite; Quartz, syn; Hemimorphite
Sa Masa substrate of rhizobox with Phragmites australis with polluted water
10
20
30
40
50
60
Position [°2Theta]

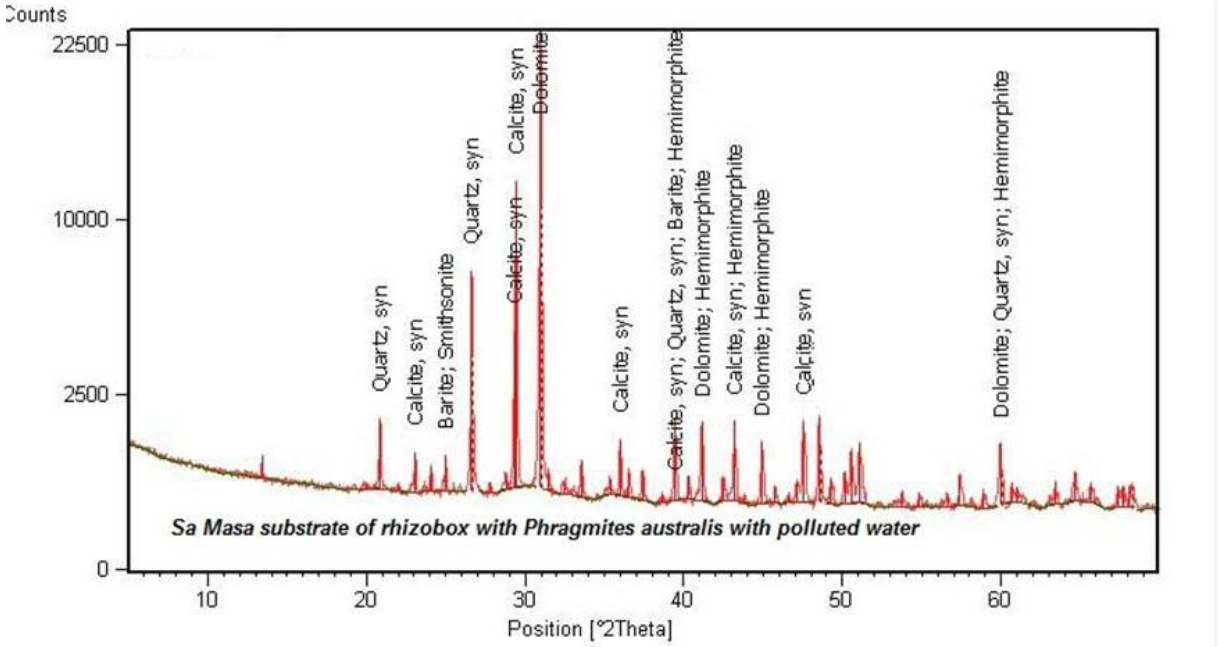
Counts
22500
10000
2500
0
Quartz, syn
Calcite, syn
Barite; Smithsonite
Quartz, syn
Calcite, syn
Calcite, syn
Dolomite
Calcite, syn
Calcite, syn; Quartz, syn; Barite; Hemimorphite
Dolomite; Hemimorphite
Calcite, syn; Hemimorphite
Dolomite; Hemimorphite
Calcite, syn
Dolomite; Quartz, syn; Hemimorphite
Sa Masa substrate of rhizobox with Phragmites australis with polluted water
10
20
30
40
50
60
Position [°2Theta]

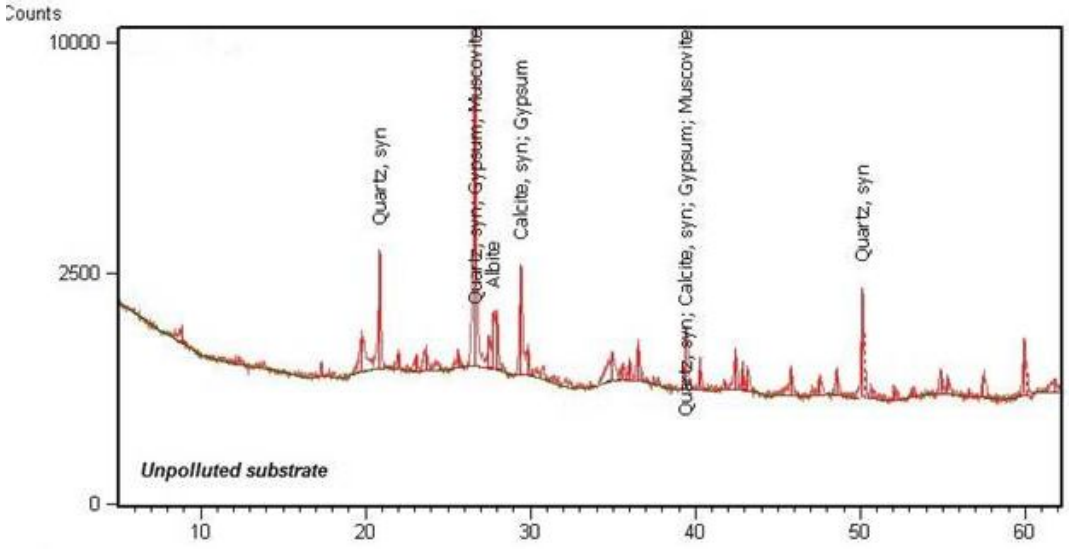
Counts
10000
2500
0
Quartz, syn
Quartz, syn; Gypsum; Muscovite
Albite
Calcite, syn; Gypsum
Quartz, syn; Calcite, syn; Gypsum; Muscovite
Quartz, syn
Unpolluted substrate
10
20
30
40
50
60

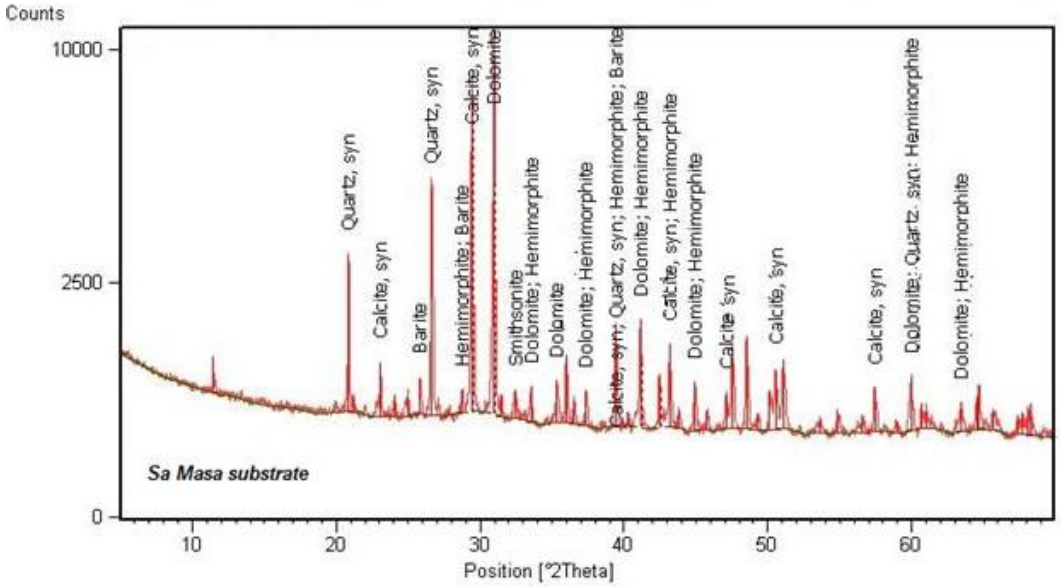
Counts
10000
2500
0
Quartz, syn
Calcite, syn
Barite
Quartz, syn
Hemimorphite; Barite
Calcite, syn
Dolomite
Smithsonite
Dolomite; Hemimorphite
Dolomite
Dolomite; Hemimorphite
Calcite, syn; Quartz, syn; Hemimorphite; Barite
Dolomite; Hemimorphite
Calcite, syn; Hemimorphite
Dolomite; Hemimorphite
Calcite, syn
Calcite, syn
Calcite, syn
Dolomite; Quartz, syn; Hemimorphite
Dolomite; Hemimorphite
Sa Masa substrate
10
20
30
40
50
60
Position [°2Theta]

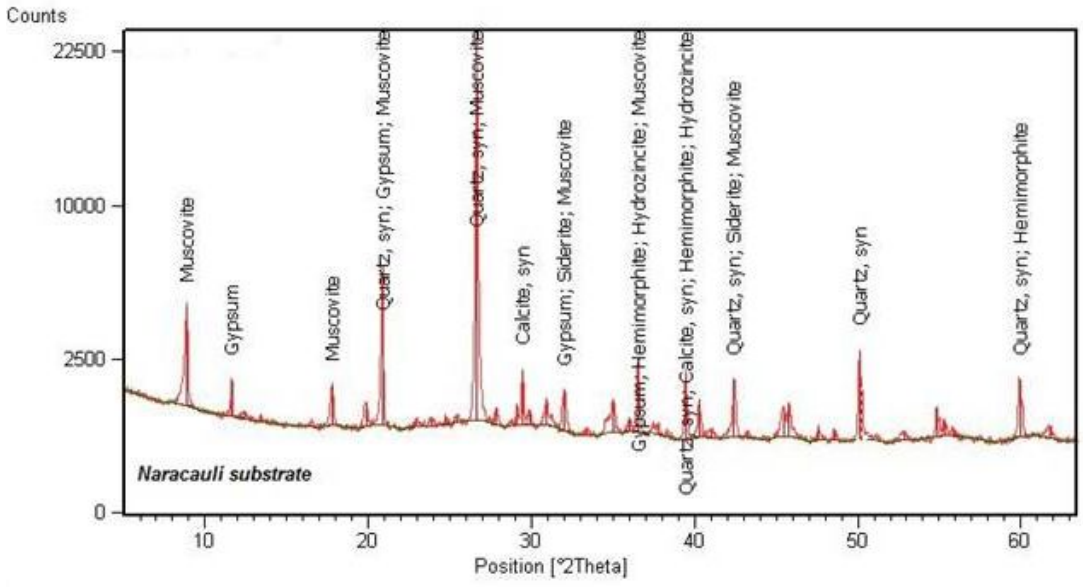
Counts
22500
10000
2500
0
Muscovite
Gypsum
Muscovite
Quartz, syn; Gypsum; Muscovite
Quartz, syn; Muscovite
Calcite, syn
Gypsum; Siderite; Muscovite
Gypsum; Hemimorphite; Hydrozincite; Muscovite
Quartz, syn; Calcite, syn; Hemimorphite; Hydrozincite
Quartz, syn; Siderite; Muscovite
Quartz, syn
Quartz, syn; Hemimorphite
Naracauli substrate
10
20
30
40
50
60
Position [°2Theta]